ΡΑΠΤΟΠΟΥΛΟΣ ΙΩΑΝΝΗΣ

ΣΧΟΛΗ ΜΗΧΑΝΟΛΟΓΩΝ ΜΗΧΑΝΙΚΩΝ

Ευστάθεια, Διακλαδώσεις και Ροή Ενέργειας σε Δυναμικά Συστήματα Ελαστικών Αξόνων σε Αεροέδρανα με Εύκαμπτο Κέλυφος (Gas Foil Bearings)

Τομέας: Μηχανολογικού Σχεδιασμού & Αυτομάτου Ελέγχου

Επιβλέπων: Αθανάσιος Χασαλεύρης, Επίκουρος Καθηγητής ΕΜΠ

Αθήνα, 2021

RAPTOPOULOS IOANNIS

SCHOOL OF MECHANICAL ENGINEERING

Stability, Bifurcations and Energy Flow in Dynamic Systems of Elastic Rotors on Gas Foil Bearings

Department: Mechanical Design & Automatic Control

Supervisor: Athanasios Chasalevris, Assistant Professor NTUA

Athens, 2021

Υπεύθυνη δήλωση για λογοκλοπή και για κλοπή πνευματικής ιδιοκτησίας:

Έχω διαβάσει και κατανοήσει τους κανόνες για τη λογοκλοπή και τον τρόπο σωστής αναφοράς των πηγών που περιέχονται στον οδηγό συγγραφής Διπλωματικών Εργασιών. Δηλώνω ότι, από όσα γνωρίζω, το περιεχόμενο της παρούσας Διπλωματικής Εργασίας είναι προϊόν δικής μου εργασίας και υπάρχουν αναφορές σε όλες τις πηγές που χρησιμοποίησα.

Ονοματεπώνυμο

Ιωάννης Ραπτόπουλος

This page has been intentionally left blank

Contents

This page has been intentionally left blank

ABSTRACT

The Diploma Thesis presents an investigation on the dynamics of elastic rotors on Gas Foil Bearings (GFBs) and aims to provide answers regarding the influence of key design parameters, such as the shaft stiffness, the foil compliance and the foil loss factor, to the quality of response, the stability of the system, and the energy flow among its main components. Right after the short presentation of the historical background of GFB technology in the introduction section, the Reynolds equation for compressible flow (gas flow) is numerically solved in order to approach the gas pressure distribution inside the GFB, and the ordinary differential equation for a simplified bump foil structure is defined. The flexible rotor is implemented in this work with the well-known equations of motion of the Jeffcott rotor.

A coupled vector including all three aforementioned components consisting of gas pressure, foil deformation, and rotor's horizontal and vertical displacements with their time derivatives is introduced and the respective nonlinear system of ordinary differential equations is represented in state space. The unique source of nonlinearity in the system is the strongly nonlinear gas forces resulting in various types of rotor motion and trajectories which are studied thoroughly in terms of stability and periodicity for different properties of the design parameters utilizing short-time Fourier transform, bifurcation diagrams, Poincaré maps and fast Fourier transform. Autonomous and non-autonomous versions of the system are studied corresponding to perfectly balanced and unbalanced rotors. The energy flow constitutes the final field of study where the work portions produced by the gas, foil spring and foil damper forces are evaluated.

Conclusions can be drawn highlighting the role of foil damping (loss factor) and the foil stiffness in the birth of limit cycle motions and their bifurcations occurring as the parameter of rotating speed changes. Saddle node (fold), and Neimark-Sacker bifurcations of limit cycles are found to occur for specific design properties, while limit cycles are generated always by Hopf-Andronov bifurcation of fixed equilibria; the corresponding whirl-whip phenomena are discussed. The energy flow between the components of the system is addressed founding that the work of gas forces along a closed orbit changes sign when saddle node bifurcations of limit cycles occur. Similar changes are noticed during bifurcations of fixed equilibria (Hopf-Andronov type).

ABSTRACT (Greek)

Η Διπλωματική Εργασία διερευνά την δυναμική των ελαστικών αξόνων σε αεροέδρανα με εύκαμπτο κέλυφος (GFBs - Gas Foil Bearings), στοχεύοντας να δώσει απαντήσεις σχετικά με την επίδραση βασικών σχεδιαστικών παραμέτρων, όπως η δυσκαμψία του άξονα, η ενδοτικότητα και η απόσβεση (loss factor) της διάταξης του foil, στην ποιότητα της χρονικής απόκρισης, την ευστάθεια του συστήματος, και τη ροή ενέργειας μεταξύ των κύριων συνιστωσών αυτού. Έπειτα από τη σύντομη ιστορική ανασκόπηση στην τεχνολογική εξέλιξη του GFB στο εισαγωγικό κεφάλαιο, η εξίσωση του Reynolds για συμπιεστή ροή (ροή ατμοσφαιρικού αέρα) επιλύεται αριθμητικά προκειμένου να εκτιμηθεί η κατανομή της πίεσης του αερίου εντός του GFB, και επιπλέον ορίζεται η διαφορική εξίσωση για την παραμόρφωση του υποσυστήματος του κελύφους. Ο ελαστικός άξονας εισάγεται στην προσομοίωση με τις εξισώσεις κίνησης του άξονα Jeffcott.

Το διάνυσμα στο χώρο κατάστασης ορίζεται με τρεις συνιστώσες: την πίεση του αερίου, την παραμόρφωση του κελύφους, και την οριζόντια και κατακόρυφη μετατόπιση του άξονα μαζί με τις χρονικές παραγώγους τους. Στη συνέχεια, ακολουθεί ο ορισμός του μη-γραμμικού συστήματος συνήθων διαφορικών εξισώσεων. Την μοναδική πηγή μη-γραμμικότητας στο σύστημα αποτελούν οι ισχυρά μη-γραμμικές δυνάμεις του αερίου, οι οποίες ευθύνονται για την δημιουργία κινήσεων ποικίλων τύπων και διαφόρων τροχιών και μελετώνται εκτενώς -ως προς την ευστάθεια και την περιοδικότητά τους για διάφορες τιμές των σχεδιαστικών παραμέτρων- χρησιμοποιώντας μετασχηματισμό Fourier, διαγράμματα διακλαδώσεων, και απεικονίσεις Poincaré. Η αυτόνομη και η μη-αυτόνομη έκδοση του συστήματος μελετώνται κατ' αντιστοιχία με άξονα χωρίς αζυγοσταθμία και με αζυγοσταθμία. Η ροή ενέργειας ανάμεσα στις συνιστώσες του συστήματος αποτελεί το τελευταίο μέρος αυτής της μελέτης όπου υπολογίζονται οι ποσότητες των έργων των δυνάμεων του αερίου, καθώς και των δυνάμεων του ελατηρίου και του αποσβεστήρα συγκράτησης του κελύφους.

Τα συμπεράσματα εξάγονται υπογραμμίζοντας τον ρόλο της απόσβεσης και της δυσκαμψίας του υποσυστήματος συγκράτησης του κελύφους στην δημιουργία κινήσεων σε οριακό κύκλο (limit cycle motions), καθώς και στις διακλαδώσεις τους (bifurcations), που συμβαίνουν καθώς μεταβάλλεται η παράμετρος της γωνιακής ταχύτητας περιστροφής του άξονα. Διακλαδώσεις αναδίπλωσης (σάγματος κόμβου – saddle node) και τύπου Neimark-Sacker λαμβάνουν χώρα για συγκεκριμένες σχεδιαστικές παραμέτρους, ενώ βρέθηκε ότι τα σημεία ισορροπίας (fixed points) χάνουν πάντα την ευστάθειά τους με διακλαδώσεις τύπου Hopf-Andronov. Τα αντίστοιχα φαινόμενα whirl-whip σχολιάζονται. Η ενεργειακή ροή μεταξύ των συνιστωσών του συστήματος εξετάζεται και συμπεραίνεται ότι το έργο των δυνάμεων του αερίου σε μία κλειστή τροχιά αλλάζει πρόσημο όταν συμβαίνουν διακλαδώσεις αναδίπλωσης (saddle node) στους οριακούς κύκλους. Παρόμοιες μεταβολές παρουσιάζονται και κατά τη διάρκεια διακλαδώσεων των σημείων ισορροπίας τύπου Hopf-Andronov.

PREFACE

Hitting a milestone is always a pleasant experience. It may sound a bit cliché, but I could not have achieved this outcome without other people's help. Even though none of them could guarantee this graduation since it requires personal effort, their support has been critical in making me capable of pursuing my dreams and achieving my goals.

For this reason, I want to express my gratitude to my parents for their selfless love and devotion throughout my whole life in every possible way and for the sacrifices they have made to provide me with the opportunity to have a high-quality education. This moment is a reward for their tireless efforts to help me progress in my life. I also want to thank my brother and the rest of my family for their unwavering love and support all these years.

I could not have achieved this goal, though, or at least with the same level of joy, if it weren't for my friends who stood by me and supported me. We shared opinions and world views, travelled around the globe, learned to appreciate every moment, and I am grateful for all the experiences we shared.

Finally, I wish to express my sincere appreciation and gratitude for the most important partner I had during this last year of my studies. Special thanks to my supervisor, Prof. Athanasios Chasalevris. Before this journey started, I could not have imagined that I would have the chance to experience such a level of cooperation and work ethic when pursuing my diploma thesis. His contribution to this work has been extraordinary, and his day-by-day guidance led me to a whole new world of knowledge and challenges.

Ioannis G. Raptopoulos

Athens, March 2021

This page has been intentionally left blank

NOMENCLATURE

$(\dot{\square})$, $(\square)'$	first order time derivatives
$(\ddot{\square})$, $(\square)''$	second order time derivatives
$\overline{\alpha}_f$	dimensionless compliance of bump foil $\left(2p_0\left(\frac{l_0}{t_b}\right)^3(1-v^2)\frac{s_0}{c_r E}\right)$
c_r	bearing clearance $[m]$
D	bearing diameter $[m]$
e, ε	unbalance eccentricity $[m]$, $\varepsilon = e/c_r$
E	Young's modulus for bump foil $[N/m^2]$
$F_{Bx}, F_{By}, \overline{F}_{Bx}, \overline{F}_{By}$	gas force components in x and y directions $[N]$, $\overline{F}_{Bx} = F_{Bx}/c_r, \overline{F}_{Bx} = F_{Bx}/c_r$
F_{c_f}	foil damper force $[N]$
F_{k_f}	foil spring force $[N]$
F_m	mean force acting on the top foil $[N]$
$F_{Ux}, F_{Uy}, \overline{F}_{Ux}, \overline{F}_{Uy}$	unbalance force components in x and y directions $[N]$, $\overline{F}_{Ux} = F_{Ux}/c_r, \overline{F}_{Ux} = F_{Ux}/c_r$
$h, \overline{h}$	fluid film thickness $[m]$, $\overline{h} = h/c_r$
$k_f, \overline{k}_f$	foil stiffness coefficient per area $(p_0/(\overline{\alpha}_f c_r))$ $[N/m^3]$, $\overline{k}_f = 1/\overline{\alpha}_f$
$k_s, \overline{k}_s$	shaft stiffness coefficient $(\overline{k}_s m_d p_0^2 {c_r}^4/(36\mu^2 R^4))$ $[N/m^2]$
$p, \overline{p}$	gas pressure $[N/m2]$, $\overline{p} = p/p_0$
$q, \overline{q}$	foil deflection $[m]$, $\overline{q} = q/c_r$
t_b	bump foil thickness $[m]$
W_{c_f}	work produced by the foil damper forces $[J]$
W_f	work produced by the foil $[J]$
W_g	work produced by the bearing's gas forces $[J]$
W_{k_f}	work produced by the foil spring forces $[J]$
$x_j, y_j, \overline{x}_j, \overline{y}_j$	journal displacements in x and y directions $[m]$, $\overline{x}_j = x_j/c_r, \overline{y}_j = y_j/c_r$
$x_d, y_d, \overline{x}_d, \overline{y}_d$	disc displacements in x and y directions $[m]$, $\overline{x}_d = x_d/c_r, \overline{y}_d = y_d/c_r$
$x, \overline{x}$	spatial coordinate in x direction, $\overline{x} = x/R$
$z, \overline{z}$	spatial coordinate in z direction, $\overline{z} = z/R$
η	loss factor for bump foil structure
θ	angular coordinate $[rad]$
μ	viscosity of gas $[Ns/m^2]$
v	Poisson's ratio for bump foil

l_0	bump half-length $[m]$
m_j	journal mass $[kg]$
m_d	disc mass $[kg]$
p_0	ambient pressure $[N/m^2]$
$p_m, \overline{p}_m$	mean gas pressure over bearing length $[N/m^2]$, $\overline{p}_m = p_m/(p_0 L)$
ξ	dimensionless parameter of the rotor model $(36\mu^2 L R^5/(m_j p_0 {c_r}^5))$
σ	dimensionless parameter of the rotor model $(36\mu^2 R^4 g/({p_0}^2 {c_r}^5))$
τ	dimensionless time $(p_0 {c_r}^2/(6\mu R^2) t)$
φ_r	journal's angle of rotation $[rad]$
χ	angle of foil fixation point $[rad]$
$\Omega, \overline{\Omega}$	angular velocity $(6\mu\omega/p_0)(R/c_r)^2$ $[rad/s]$, $\overline{\Omega} = 6\mu R^2/(p_0 {c_r}^2)$

ABBREVIATIONS

DL	Dimensionless
DM	Dimensioned
FDM	Finite Difference Method
GFB	Gas Foil Bearing
NS	Neimark-Sacker
SN	Saddle node

1 INTRODUCTION

1.1 Background on Gas Foil Bearing Development

Gas foil bearings (GFBs) are an upcoming and promising oil-free technology in modern high-speed rotating machinery [1]. Relying on a thin gas film building up an aerodynamic, load-carrying lubrication wedge, such bearings are self-acting and do not require any external pressurization. Most notably, due to the absence of solid-to-solid contact between the airborne rotor journal and the bearing sleeve, excessively low wear and power loss can be achieved [2].

During the last few decades, the potential of GFBs has been widely confirmed by a great number of successful applications in air cycle machines of commercial aircraft [3]. Lately, in particular as a result of insurmountable speed, temperature, and weight limitations of conventional rolling-element bearings, novel concepts of oil-free turbochargers [4] and oil-free rotorcraft propulsion engines [5] are gaining more and more interest.

Foil air bearings are similar to conventional oil-lubricated bearings in size, shape, and in that the fluid film pressure is developed via the hydrodynamic effect, see Figs. 1.1 and 1.2. Unlike conventional bearings, foil air bearings use air as their working fluid and the bearing surface is compliant rather than rigid [6]. This compliant inner or top foil surface is supported by a spring pack or bump foil layer which allows the bearing to accommodate shaft misalignment, thermal and centrifugal distortion, the presence of

[1] T. Leister, C. Baum, W. Seemann (2017) On the Importance of Frictional Energy Dissipation in the Prevention of Undesirable Self-Excited Vibrations in Gas Foil Bearing Rotor Systems. TECHNISCHE MECHANIK, 37, 2-5, (2017), 280 – 290

[2] Heshmat, H.; Walowit, J. A.; Pinkus, O. (1983) Analysis of gas-lubricated foil journal bearings. Journal of Lubrication Technology, 105, 4, 647–655.

[3] Howard, S. A.; Bruckner, R. J.; DellaCorte, C.; Radil, K. C. (2007) Gas foil bearing technology advancements for closed Brayton cycle turbines. Tech. Rep. NASA TM-214470, National Aeronautics and Space Administration, United States of America.

[4] Howard, S. A. (1999) Rotordynamics and design methods of an oil-free turbocharger. Tech. Rep. NASA CR-208689, National Aeronautics and Space Administration, United States of America.

[5] Howard, S. A.; Bruckner, R. J.; Radil, K. C. (2010) Advancements toward oil-free rotorcraft propulsion. Tech. Rep. NASA TM-216094, National Aeronautics and Space Administration, United States of America.

[6] DellaCorte C., Zaldana, A., and Radil, K. (2004) A Systems Approach to the Solid Lubrication of Foil Air Bearings for Oil-Free Turbomachinery. STLE/ASME Joint International Tribology Conference, FL Oct. 2003.

wear debris and also allows the designer to tailor the operational foil shape to enhance film pressure and hence bearing load capacity [7].

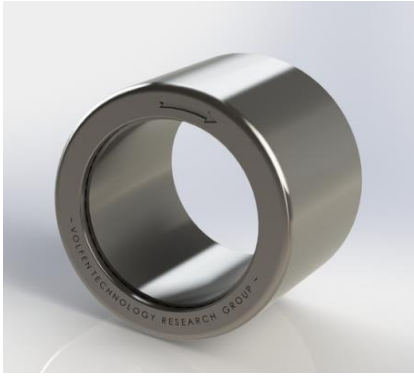

Fig. 1.1: Photo of an integrated gas foil bearing; taken from grabcad.com

Fig. 1.2: Photo of the inner compounds of a gas foil bearing; taken from sulzer.com

Fig. 1.3 schematically shows typical foil bearing designs. Micro-sliding, which occurs between the top foil and its spring support and within the spring foils, contributes significant coulomb damping properties to the bearing [8].

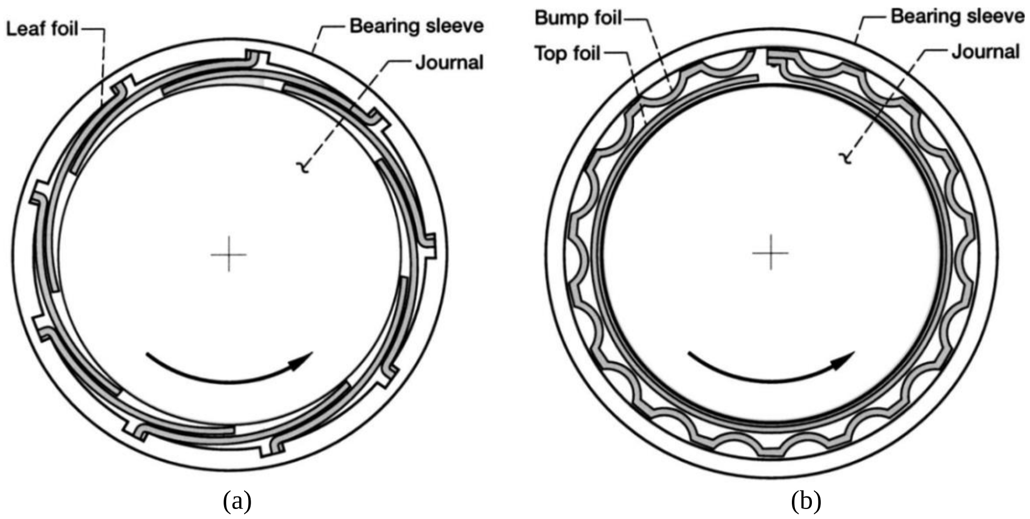

Fig. 1.3: Schematic example of typical first-generation foil bearings with axially and circumferentially uniform elastic support elements: a) leaf-type foil bearing; and b) bump-type foil bearing; taken from [6]

Since foil bearings do not use oil as their working fluid they can and are routinely used over an extremely wide temperature range, from cryogenic to over 650°C, not possible with oil lubrication. Foil air bearings, however, do require solid lubrication to prevent wear and reduce friction at very low speeds encountered during start-up and shut-down prior to the development of the hydrodynamic gas film and also during momentary

[7] Gross, W. A. (1962) Gas Film Lubrication, John Wiley and Sons, Inc.

[8] Heshmat, H., Shapiro, W., and Gray, S. (1982) Development of Foil Journal Bearings for High Load Capacity and High Speed Whirl Stability, ASME J. Lubr. Technol., 104, pp. 149–156.

bearing overloads such as high-speed rubs [9]. Traditionally, this solid lubrication is provided by applying a thin polymer film or coating to the foil surface, see Fig. 1.4.

Blok and Van Rossum published the first paper on foil bearings in 1953 [10]. Although they coined the term ‘‘foil bearing’’, their work actually concerned an oil lubricated shaft running against an acetate film or ‘‘foil’’. The concept of a flexible bearing surface and its implications to and potential for improved capabilities was quickly adapted by other technologists and papers on air lubricated foil bearings began to appear in the open literature in the following decade [11,12]. Foil bearing load capacity is expressed in relation to a bearing’s load capacity coefficient, D. This coefficient, defined fully in [13], is an empirically established performance parameter which relates bearing size and speed to the load that a bearing can support. Mathematically, it is defined as follows [6,13]:

$$W = D \times (L \times d) \times (d \times \mathrm{krpm})$$

where W is the maximum steady load that can be supported, N; D is the bearing load capacity coefficient, N/mm3krpm; L is the bearing axial length, mm; and d is the shaft diameter, mm. krpm is the shaft rotational speed in thousands of revolutions per minute, krpm. This relationship can be remembered easily for advanced technology bearings, which have load capacity coefficients of around 1.0 when non-SI or English units are used. The comparable coefficient for SI units is about 175 kPa/mm. An advanced design, designated Generation III [6] foil bearing, like the type depicted in Fig. 1.6, will support about ‘‘one pound of load per in2 of projected bearing area per inch of bearing diameter per thousand rpm.’’ The earliest foil bearing designs, designated Generation I, had very simple elastic support structures (spring systems) and exhibited load capacity coefficients of around 0.3. The development of more complex bearing designs in which the elastic foundation varied circumferentially or axially is defined as Generation II and exhibit load capacity coefficients around 0.5. The most recent bearing designs have elastic structures which tailor the spring foundation both circumferentially and axially, are designated Generation III bearings, and have load capacity coefficients of about 1.0. Foil bearings used in air cycle machines are Generation I bearings. Generation II bearings have been used successfully in turbocompressors and small

[9] DellaCorte, C., and Wood, J. C. (1994) High Temperature Solid Lubricant Materials for Heavy Duty and Advanced Heat Engines, NASA TM-106570.

[10] Blok, H., and van Rossum, J. J. (1953) The Foil Bearing-A New Departure in Hydrodynamic Lubrication, ASLE J. Lubr. Eng., 9, pp. 316–330.

[11] Ma, J. T. S., 1965, ‘‘An Investigation of Self-Acting Foil Bearings,’’ASME J. Basic Eng., 87, pp. 837–846.

[12] Barnett, M. A., and Silver, A. (1970) ‘‘Application of Air Bearings to High Speed Turbomachinery,’’ SAE Paper 700720.

[13] DellaCorte, C., and Valco, M. J. (2000) Load Capacity Estimation of Foil Air Journal Bearings for Oil-Free Turbomachinery Applications, STLE Tribol. Trans., 43, pp. 795–801.

microturbines. It is expected that Generation III bearings with load capacity coefficients near 1.0 will be used in aircraft engine applications.

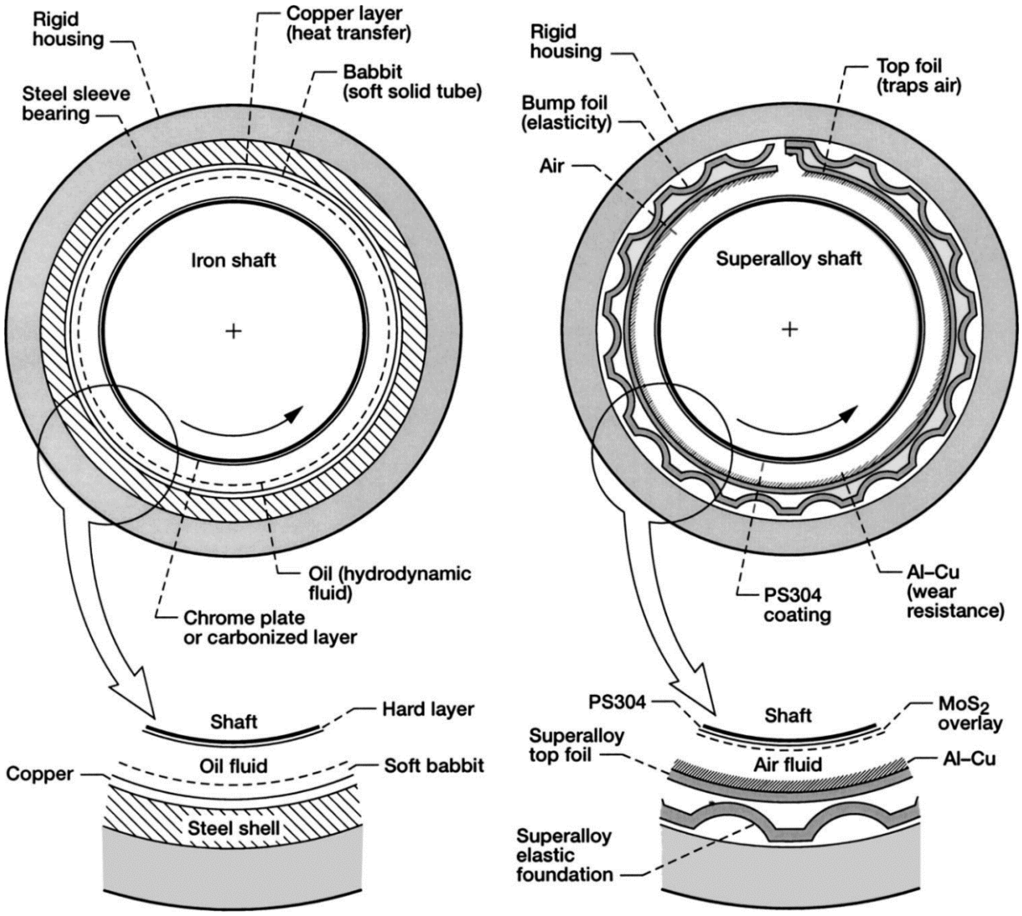

Fig. 1.4: Schematic representation of systems approach to bearing lubrication a) conventional oil lubricated bearing, and b) multilevel solid/gas lubricated foil air bearing [6]

Foil bearings have been successfully used in high-speed turbomachines, and they present a remarkable reliability. For aircraft turbo-compressors, the mean-time-between failure is typically over 60000 h [[14],[15]]. The operational mechanism of foil bearings is similar to that of fluid-film bearings. At the start-up stage, the rotor journal and the bearing bore are contacting each other directly. Once the rotational speed crosses the lift off speed, the rotor will be suspended by the generated pressure fluid film. As the stiffness of the foils is much smaller than that of the fluid film, the foil bearings can adapt to various working conditions through foil deformations. Specially, the range between the second and third critical speeds of the foil bearing-rotor system

[[14]] Y. Hou, Z. H Zhu, C. Z. Chen (2004) Comparative test on two kinds of new compliant foil bearing for small cryogenic turbo-expander. *Cryogenics*, 44: 69-72.

[[15]] Z. Y. Guo, K. Feng, T. Y. Liu (2018) et al. Nonlinear dynamic analysis of rigid rotor supported by gas foil bearings: effects of gas film and foil structure on subsynchronous vibration. Mechanical Systems and Signal Processing, 107: 549-566.

is very large, which means that the foil bearings can suspend the rotor at a very high speed stably. Owing to these advantages, foil bearings are identified as a potential

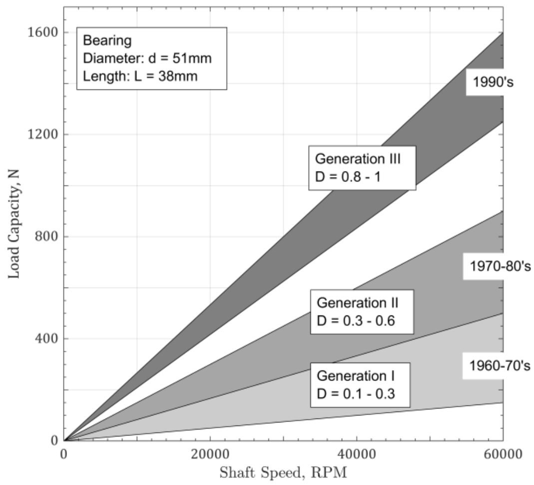

Fig. 1.5: Bearing Load Capacity, Gen. I, II, III [8]

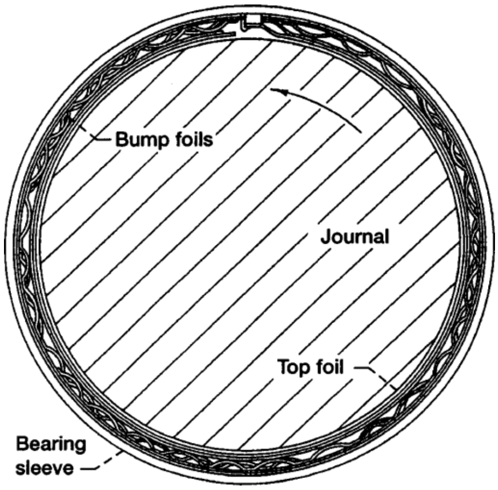

Fig. 1.6: Generation III foil air bearing [8]

alternative for REBs. If properly designed and operated, foil bearings would incur very slight wear and have a long service life [[16]].

In the 1990s, NASA conducted various tests of foil bearings in LH2 and LO2 environments [[17],[18]]. The material compatibility of three candidate polymer coatings for LH2 lubricated foil bearings was tested at the NASA White Sands Test Center [[19]]. There were no ignition hazards during the frictional heating tests, which means that these polymer coatings can be used in the establishment of foil bearing turbopumps. After that, LH2 foil bearing

[[16]] H Heshmat H. (1991) A feasibility study on the use of foil bearings in cryogenic turbopumps. 27th AIAA/SAE/ASME/ASEE Joint Conference, California, USA, June 24-26: AIAA-91-2103.

[[17]] M. Saville, A Gu, R Capaldi (1991) Liquid hydrogen turbopump foil bearing. 27th AIAA/SAE/ASME/ASEE Joint Propulsion Conference and Exhibit, California, USA, June 24-26: AIAA-91-2108.

[[18]] J. S. McFarlane, M P Saville, S C Nunez (1995) Testing a 10000 lbf thrust hybrid motor with a foil bearing LOx turbopump. 31st AI-AA/SAE/ASME/ASEE Joint Propulsion Conference and Exhibit, California, USA, July 10-12: AIAA-95-2941.

[[19]] J. M. Stoltzfus, J. Dees, A. Gu, et al. (1992) Material compatibility evaluation for liquid oxygen turbopump fluid foil bearing. 28th AIAA/SAE/ASME/ASEE Joint Propulsion Conference and Exhibit, Tennessee, USA, July 6-8: AIAA-92-3403.

turbopump and LO2 turbopump demonstrations were conducted subsequently [20]. In 1992, the LH2 foil bearing turbopump was successfully tested in NASA Stennis Space Center. The maximum rotational speed was 91000 r/min. After over 100 times of a frequent start/stop, the foil bearings and rotating assembly were still in excellent condition. In 1993, a LO2 turbopump demonstration was successfully conducted in NASA Marshall Space Flight Center. The maximum rotational speed was 25000 r/min and the total start/stop times were over 100. However, foil bearings have not yet been adopted in any rocket turbopump in service. In fact, the working principle of foil bearings is almost identical to that of fluid film bearings, and thus, the start-up problem still exists. Although bearing coatings were adopted, some debris particles with a size of approximately 0.51 mm were still found in NASA foil bearing turbopump demonstrations and the bearing surface was scratched by them to some extent. This is a potential hazard for a safe service, which cannot be ignored.

1.2 Gas Foil Bearings and Rotor Dynamics

Most of the considered rotating machinery is supposed to reach and to maintain a stable operating point after completing the run-up. However, as a result of the highly nonlinear bearing forces induced by the pressurized fluid, the existing equilibrium points of GFB rotor systems tend to become unstable for higher rotational speeds [1]. Subsequently, undesirable self-excited vibrations with comparatively large amplitudes may occur [21,22,23]. For this reason, many common bearing designs feature a compliant and slightly movable multi-part foil structure inside the lubrication gap. By dissipating a certain amount of energy via dry sliding friction mechanisms [24], this countermeasure is supposed to reduce the vibrational amplitudes or, as the ultimate goal, to prevent the occurrence of self-excited vibrations in the first place.

The gas foil bearing is becoming very popular in oil free turbo-machinery because of its good dynamic characteristics and environment friendly features. There are different

[20] A. Gu (1994) Cryogenic foil bearing turbopumps, 32nd Aerospace Science Meeting & Exhibit, Nevada, USA, January 10-13: AIAA-94-0868.

[21] Bonello, P.; Pham, H. M. (2014) The efficient computation of the nonlinear dynamic response of a foil-air bearing rotor system. Journal of Sound and Vibration, 333, 15, 3459–3478.

[22] Hoffmann, R.; Pronobis, T.; Liebich, R. (2014) Non-linear stability analysis of a modified gas foil bearing structure. In: Proceedings of the 9th IFToMM International Conference on Rotor Dynamics, Milan, Italy.

[23] Baum, C.; Hetzler, H.; Seemann, W. (2015) On the stability of balanced rigid rotors in air foil bearings. In: Proceedings of the SIRM 2015, Magdeburg, Germany(2015a).

[24] Peng, J.-P.; Carpino, M. (1993) Calculation of stiffness and damping coefficients for elastically supported gas foil bearings. Journal of Tribology, 115, 1, 20–27.

types of foil bearings viz. leaftype, bumptype, tapetype, multi-wound and foil bearing with compression springs [25] etc. The bump type foil bearing is simple in construction and more efficient compared to the other types of foil bearing. It is superior to conventional gas bearing and has higher load capacity, lower power loss, good stability, and endurance to high temperature, misalignment and foreign particles in the gas [2]. Due to these advantages, it is considered as best candidate for oil free turbo-machinery and have shown potential for micro/meso- scale gas turbine and its different applications [26,27]. A good amount of research work on bump type foil bearing dynamics has been carried out in the past three decades. Heshmat et al. [2] presented the first model of bump type of foil bearing. In this model they considered only elastic effect to bump foil; whereas damping due to the interaction of bump foil to top foil and bump foil to bearing housing is not considered. Later, Ku and Heshmat [28] proposed a more elaborate model that comprises elastic deformation of bump, interactions between bumps, Coulomb friction damping between top and bump foils as well as interaction between bump foil and bearing housing. Peng and Carpino [24] presented linear stiffness and damping coefficients of bump foil bearing considering elastic effect of bump foil. Peng and Carpino [29] also presented foil bearing dynamic coefficients using finite element method. Iordanoff [30] proposed rapid design method for foil thrust bearing in which static stiffness of bump with friction between bump foil and housing is incorporated.

[25] J. Song, D. Kim (2007) Foil gas bearing with compression springs: analysis and experiments, Journal of Tribology 129:628–639.

[26] S.P. Bhore, A.K. Darpe (2013) Investigations of characteristics of micro/meso-scale gas foil journal bearings for 100-200W class micro-power system using first order slip velocity boundary condition and the effective viscosity model, Journal of Microsystem Technologies 19:509–523, http://dx.doi.org/ 10.1007/s00542-012-1639-1.

[27] S.P. Bhore, A.K. Darpe (2014) Rotordynamics of micro and mesoscopic turbomachinery: a review, Journal of Advances in Vibration Engineering 13 (1), in press.

[28] C. P. Ku, H. Heshmat (1992) Compliant foil bearing structural stiffness analysis: part1-theoretical model including strip and variable bump foil geometry, Journal of Tribology 114 (2): 394–400.

[29] J. P. Peng, M. Carpino (1997) Finite element approach to the prediction of foil bearing rotor dynamic coefficients, Journal of Tribology 119 (1): 85–90.

[30] I. Iordanoff (1997) Analysis of an aerodynamic compliant foil thrust bearing: method for a rapid design. Journal of Tribology 121 (4) 1996 816-822

Kim and San Andres [31] obtained bearing characteristics for heavily loaded foil bearing and validated with test results. They also presented frequency dependent dynamic coefficients. San Andres and Kim [32] presented nonlinear response of rotor supported by gas foil bearing. The nonlinear nature of stiffness characteristics of foil bearing is modelled using experimental data. They have shown that the linear force coefficients are not reliable to represent the dynamic behavior of rotor supported on gas foil bearing. Kim [33] conducted a parametric study on the static and dynamic characteristics of bump type foil bearings with different top foil geometries (circular and three pad configurations) and bump stiffness distributions. He presented a mathematical model of the bump foil bearing with equivalent viscous damping. The comparison of the static and dynamic performance of the bearing with linear perturbation based dynamic coefficients and a time domain orbit simulation is carried out. He found that there is a significant difference in the estimated onset speeds of instability from the set of approaches. A more advanced analytical modelling of foil bearing is reported by Lez et al [34]. The bumps and their interaction are modeled by multi-degree freedom system. The interactions between the top foil and bump foil and between bump foil and housing are modelled with friction forces. Feng and Kaneko [35] also presented an analytical model of the bump type foil bearing using link spring structure and finite element-based shell model. Lez et al. [36] have studied the nonlinear behavior of the foil bearing with stability and unbalance responses. Nonlinear jump phenomena have been observed. The shaft trajectory analysis and influence of friction on stability are investigated. They have not explored the bifurcation analysis with different system parameters [37]. As the gas foil bearing shows nonlinear behavior [32,33], the analysis of dynamic behavior of rotor

[31] T. H. Kim, L. San Andres (2008) Heavily loaded gas foil bearings: a model anchored to test data, Journal Engineering for Gas Turbines and Power 130 (1) 012504–012508.

[32] L. San Andres, T. H. Kim (2008) Forced nonlinear response of gas foil bearing supported rotors, Tribology International 41 704–715.

[33] D. Kim (2007) Parametric studies on static and dynamic performance of air foil bearings with different top foil geometries and bump stiffness distributions, Journal of Tribology 129 (2) 354–364.

[34] S. Le Lez, M. Arghir, J. Frene (2007) A new bump-type foil bearing structure analytical model, Journal of Engineering for Gas Turbines and Power 129 (4) 1047–1057.

[35] K. Feng, S. Kaneko (2010) An alytical model of bump-type foil bearings using a link spring structure and a finite element shell model, Journal of Tribology 132 (2) 1–11.

[36] S. Le Lez, M. Arghir, J. Frene (2009) Nonlinear numerical prediction of gas foil bearing stability and unbalanced response, Journal of Engineering for Gas Turbines and Power 131:012503–012512.

[37] S. P. Bhore , A. K. Darpe (2013) Nonlinear dynamics of flexible rotor supported on the gas foil journal bearings. Journal of Sound and Vibration 332:5135–5150

supported on gas foil bearing is essential. A detailed nonlinear dynamic analysis using bifurcation diagrams, Poincaré maps, trajectories and Fast Fourier transforms is hence needed.

In order to deal with computationally expensive rotor-bearing nonlinear dynamic analysis in the time domain, linear damping and stiffness coefficients were calculated to predict rotor-bearing stability [38]. The rapid development of computer science and increasing computer power later enabled the solution of the mathematical models in the time domain and allowed for the inclusion of gas compressibility and foil compliance in the models. Although almost a century has passed since the first publications about gas bearings, the accurate time simulation of gas bearings with compliant surfaces is still a challenging and very time-consuming task. Prior to the presented work, different approaches for solving the compressible Reynolds equation have been investigated. Among others, Wang and Chen [39] who used finite difference for the spatial and temporal dimensions when solving the Reynolds equation. They simulated the steady-state response of a perfectly balanced rigid rotor supported by two identical bearings. The spatial discretization was performed with a central-difference scheme, while the temporal discretization was performed with an implicit-backward-difference scheme. Arghir et al. [40] presented a finite volume solution where the pressure was implicitly integrated for a prescribed gap perturbation to calculate linear stiffness and damping coefficients dependent on the perturbation amplitude. In the procedure, the rotor was stationary in one direction, while the other was perturbed by a sinusoidal displacement, $\mathrm{A}\sin(\omega t)$. At each time step, the reaction forces from the air film were calculated and based on the displacement/velocity and reaction force pairs, the least square method was used to calculate the linear stiffness and damping for a given amplitude A. This allowed a linear analysis of a rotor system to take into account the nonlinearities related to the vibration amplitude of the rotor in the air bearings. A common method to solve the compressible Reynolds equation in time is to substitute the time derivatives dp/dt and dh/dt by backward-difference approximations [41,42]. In this case, these time

[38] J. W. Lund (1968) Calculation of stiffness and damping properties of gas bearings, Journal of Lubrication Technology 793–804.

[39] C.-C. Wang, C.-K. Chen (2001) Bifurcation analysis of self-acting gas journal bearings, Journal of Tribology 123:755.

[40] M. Arghir, S. LeLez, J. Frene (2006) Finite-volume solution of the compressible Reynolds equation: linear and non-linear analysis of gas bearings, Proceedings of the Institution of Mechanical Engineers, PartJ: Journal of Engineering Tribology 220:617–627.

[41] J.-H. Song, D.Kim (2007) Foil gas bearing with compression springs: analyses and experiments, ASME Journal of Tribology 129:628–639.

[42] D. Lee, Y.-C. Kim, K.-W. Kim (2009) The dynamic performance analysis of foil journal bearings considering coulomb friction: rotating unbalance response, Tribology Transactions 52:146–156.

derivatives will be lagging behind in time, and the time steps need to be very small in order to preserve the accuracy of the solution. This method was employed by e.g. LeLez et al. [43] and Kim [44]. The method was also used by Zhang et al. [45] to solve the transient Reynolds equation, but with four-node planar finite elements for the spatial discretization of the Reynolds equation and for a rigid gas journal bearing. More recently, Bonello and Pham [46,47] solved the nonlinear Reynolds equation by using an alternative state variable $\psi = ph$. Using this alternative state variable, it was possible to setup a set of ordinary differential equations (ODE) to solve the Reynolds equation and other state variables simultaneously at each time step. For spatial discretization, a finite difference and Galerkin reduction method were used. The solution for the transient compressible Reynolds equation was then coupled to the simple elastic foundation model (SEFM), and the transient response of a rotor system was presented. In order to accelerate the time simulations, several authors have consistently and diligently been working on improving the numerical methods and developing new numerical strategies. A simplified method for evaluating the nonlinear fluid forces in air bearings was recently proposed by Hassini and Arghir [48,49,50]. The fundamental idea was based on approximating the frequency-dependent linearized dynamic coefficients at several eccentricities by second-order rational functions in the Laplace domain. By applying the inverse of the Laplace transform to the rational functions, a new set of ordinary differential equations was obtained, leading to an original way of linking the fluid forces components to the rotor displacements. The numerical results showed good agreement

---

[43] S. LeLez, M. Arghir, J. Frêne (2009) Nonlinear numerical prediction of gas foil bearing stability and unbalanced response, Journal of Engineering for Gas Turbines and Power 131:012503.

[44] D. Kim (2007) Parametric studies on static and dynamic performance of air foil bearings with different top foil geometries and bump stiffness distributions, Journal of Tribology 129: 354–364.

[45] J. Zhang, W. Kang, Y. Liu (2009) Numerical method and bifurcation analysis of Jeffcott rotor system supported in gas journal bearings, Journal of Computational and Nonlinear Dynamics 4 011007.

[46] P. Bonello, H. M. Pham (2014) The efficient computation of the nonlinear dynamic response of a foil–air bearing rotor system, Journal of Sound and Vibration 333:3459–3478.

[47] H. M. Pham, P. Bonello (2013) Efficient techniques for the computation of the nonlinear dynamics of a foil–air bearing rotor system, ASME TurboExpo2013: Turbine Technical Conference and Exposition, p.7.

[48] M. A. Hassini, M. Arghir (2014) A Simplified and Consistent Nonlinear Transient Analysis Method for Gas Bearing: Extension to Flexible Rotors, Düsseldorf, Germany, June 16–20. GT2014-25955.

[49] M. A. Hassini, M. Arghir (2013) A new approach for the stability analysis of rotors supported by gas bearings, Proceedings of ASME Turbo Expo 2013, pp.1–13.

[50] M. A. Hassini, M. Arghir (2012) A simplified nonlinear transient analysis method for gas bearings, Journal of Tribology 134:011704.

with the results obtained solving the full nonlinear transient Reynolds equation coupled to the equation of motion of a point mass rotor. By ensuring the continuity of the values of the fluid forces and their first derivatives and imposing the same set of stable poles to the rational functions, simplified expressions of the fluid forces were found, avoiding the introduction of false poles into the rotor-bearing system. In [48], the authors showed that the new formulation may be applied to compute the nonlinear response of systems with multiple degrees of freedom such as a flexible rotor supported by two air bearings. On the other hand, working directly with the solution of the Reynolds equation for compressible fluids and compliant surfaces, Bonello and Pham [46,50] presented a generic technique for the transient nonlinear dynamic analysis and the static equilibrium stability analysis of rotating machines, using the finite-difference state equations of the air films with the state equations of the foil structures and the state equations of the rotating machine model. To accelerate the time simulations, the state Jacobian matrix was obtained using symbolic computing, and the equations were solved using a readily available implicit integrator and a predictor-corrector approach.

In [51], an industrial rigid rotor supported by two identical segmented foil bearings is modelled and the effect of rotor unbalance is theoretically and experimentally investigated. The main original contribution of the work was related to the accurate, i.e. quantitatively and qualitatively, prediction of the nonlinear steady-state rotor response. The modelling of the segmented three pad foil bearings was carried out with high attention to the actual geometry by including the inlet slope, which has previously been found to influence both the static and dynamic results [52]. The foil structural model was based on the SEFM but with a stiffness k and loss factor η deduced from a previously described mathematical model [53]. This model considered the friction forces between the sliding surfaces and was validated against experiments. Consequently, the bump foil stiffness k used in [51] differs significantly from results in the literature, in which the foil stiffness was based on analytical expressions not accounting for the stiffening effect generated by the friction forces, e.g. Walowit and Anno [54]. The discretization of the

[51] J. S. Larsen, I. F. Santos (2015) On the nonlinear steady-state response of rigid rotors supported by air foil bearings-Theory and experiments, Journal of Sound and Vibration 346:284–297

[52] J. S. Larsen, A. J.-T. Hansen, I. F. Santos (2014) Experimental and theoretical analysis of a rigid rotor supported by air foil bearings, Mechanics &Industry.

[53] J. S. Larsen, A. C. Varela, I. F. Santos (2014) Numerical and experimental investigation of bump foil mechanical behaviour, Tribology International 74:46–56.

[54] J. A. Walowit, J. N. Anno (1975) Modern Developments in Lubrication Mechanics, Applied Science Publishers, London.

Reynolds equation is performed using the finite element method [55] and the solution of the mathematical model was based on the strategy suggested in [46,47].

Gas bearings have been intensively investigated, theoretically as well as experimentally, for nearly six decades [56,57,58] although some initial publications are dated already from the beginning of the last century [59], and it is rather difficult to cover a representative part of contributions. However, review papers help to perceive the evolution of gas foil bearing technology [60].

In this Master Thesis a rather simplistic model for bump foil properties of linearized stiffness and damping coefficients is utilized, taken directly from literature [2,37,44], and the first two design parameters are introduced as foil compliance a_f and foil loss factor η. The rotor model follows the Jeffcott rotor model and the third design parameter of shaft stiffness k_s is introduced in the modelling. The nonlinear dynamic characteristics of the system are investigated evaluating its time domain response for several sets of a_f, η, and k_s and a study is performed on the quality of stability and of feasible motions experiencing bifurcations. The study of the work portions dissipated in the damping sources of gas and bump foil presents a correlation of the energy flow to the respective bifurcation developed. A real system consisting of a high-speed centrifugal compressor rotor on gas foil bearings is also included in the simulations. The problem description and the work outline are described in continue.

1.3 Problem Description

This work aims to give answers on the influence of key design characteristics of the system (rotor stiffness, bump foil stiffness, bump foil damping) in the quality of response (stable, unstable, periodic, quasi-periodic, chaotic) and the respective energy flow

[55] J. S. Larsen, I. F. Santos (2014) Efficient solution of the non-linear Reynolds equation for compressible fluid using the finite element method, Journal of the Brazilian Society of Mechanical Sciences and Engineering 1–13.

[56] B. Sternlicht, R. C. Elwell (1957) Theoretical and experimental analysis of hydrodynamic gas-lubricated journal bearings, American Society of Mechanical Engineers-Papers.

[57] J. S. Ausman (1961) An improved analytical solution for self-acting, gas-lubricated journal bearings of finite length, Journal of Basic Engineering 83:188–192.

[58] V. Stingelin (1963) Theoretische und experimentelle Untersuchungen an Gaslagern, PhDThesis, Eidgenössischen Technischen Hochschulein Zürich.

[59] W. J. Harrison (1913) The hydrodynamical theory of lubrication with special reference to air as a lubricant, Transactions Cambridge Philosophical Society 22:34–54.

[60] P. Samanta, N.C. Murmu, M.M. Khonsari (2019) The evolution of foil bearing technology. Tribology International 135:305–323

among the major components of the system (rotor, gas, bump foil) at stable operation and at bifurcation points. The questions to be answered are considered as follows:

- What is the relation between rotor stiffness, foil stiffness, and foil damping in order to achieve asymptotically stable motions of the rotor at a specific rotating speed range?
- What is the mechanism which triggers self-excited vibrations, and how this can be prevented?
- What are the portions of energy provided into the system, and dissipated in the system before and after bifurcations take place?

The answers are not always possible in the sense of existence of analytical formulas that describe the functions between input design parameters and output response (in terms of frequency content and quality). However, all answers have been addressed with respect to the notifications made in the various case studies and concluding remarks may be considered as design rules for a stable motion with or without sub-harmonic components.

1.4 Work Outline

The outline of work is described in Fig. 1.7 referring to the major part of the work. This is included in Chapters 2 and 3.

In Chapter 2 (Simulation Method), the first objective is the modelling of a gas foil bearing (Section 2.1) where the Reynolds equation for compressible flow is solved and the gas pressure distribution is defined (Section 2.1.1) in a coupled fluid-structure dynamic model. The structural model of the bump foil is rather simplified in this work as described in Section 2.1.2. The model of flexible rotor is following (Section 2.2) using the simple Jeffcott rotor.

In Section 2.3 the composition of the dynamic system renders the full set of ordinary differential equations coupling three vectors in the system response: the rotor vibration, the gas pressure, and the bump foil deformation. The set of equations is nonlinear due to the nonlinearity introduced by the gas impedance forces. This is the only source of nonlinearity in the system, and its strong character will render quite different quality of motion trajectories. The system of differential equations follows two versions: the autonomous, where no excitation is considered, and the non-autonomous, where unbalance excitation is introduced. The autonomous system is used for the stability assessment of the system; this is included in Section 2.4. The non-autonomous system is used to produce all the rest results presented in Chapter 3.

In Chapter 3, the results are obtained in two operating conditions of the Jeffcott rotor system, and for various combinations of bump foil stiffness and damping: at the first, the system performs a run-up with linearly varying rotating speed (constant rotational acceleration) and the response is transient in the entire time domain, while at the second case the same system is rotating with different values of rotating speed for specific time domain (approximately 500 driving periods at each value of rotating speed). At the second case, steady state response is

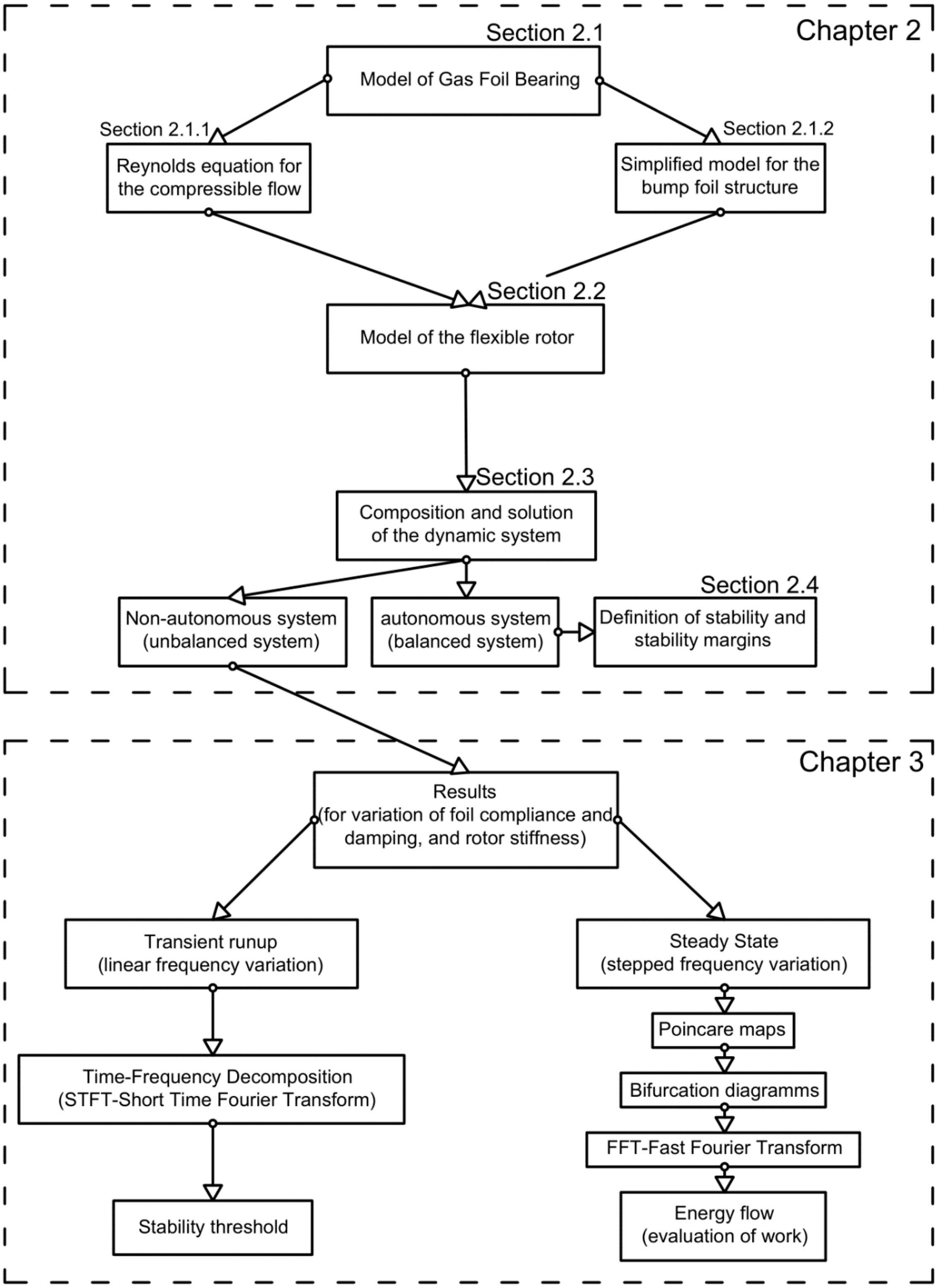

Fig. 1.7: Work flow

obtained at the last 100 driving periods, at most cases (not always). The change of rotating speed from one constant value to another is performed with a locally smoothing function. Respective results are generated from each case of operation.

The transient response is examined with respect to the frequency content applying time-frequency decomposition (Short Time Fourier Transform). The stability threshold for the Hopf and for other types of bifurcations is also identified through the transient response.

The steady state response is post-processed to produce Poincaré maps, the respective bifurcation diagrams, and the frequency content after a Fast Fourier Transform is applied. Last, but not least there is an extensive treatment of the steady state response (of all system components) to evaluate the work portions produced by the gas forces, and the foil spring and damper forces. These work portions are examined to their relevance for various case studies with emphasis in rotating speeds shortly before and after a bifurcation occurs.

Chapter 4 concludes on the influence of key design properties of the system in the quality of each response, and the energy flow between the components of the system at selected cases.

This page has been intentionally left blank

2 SIMULATION METHOD

2.1 Model of the gas foil bearing

Fig. 2.1 shows a Gas Foil Bearing consisting of three parts: the rigid part, or housing (represented in the figure at the bottom of the bearing), the bump foil -explained thoroughly in section 2.1.2- and the top foil. Due to bump foil's structure, the top foil can be deformed as shown. The journal's and bearing's rotational axes are considered parallel, an assumption necessary to neglect any misalignment. The geometrical centers of the journal and the bearing are denoted by O_j and O_b respectively, while their nominal radiuses are defined as R, $R + c_r$, where c_r is the nominal radial clearance. When no radial load is applied in the journal, then journal and bearing are concentric.

Eccentricity $e = \left(x_j^2 + y_j^2\right)^{1/2}$ describes the distance between the two centers, with x_j, y_j being the displacements of the journal in x, y axes respectively, and it has a vital role in the performance of the bearing. The top foil deformation in radial direction is denoted by q, considered positive when it is developed to the outer side of the bearing, and is a function of θ angle and time t ($q = q(\theta, t)$) in the dynamic problem. Coordinate θ is measured from the horizontal positive semi-axis of the bearing (global stationary coordinate system). The deflection of the foil is provoked by the pressure distribution p of the compressible gas flowing in the gap between journal and top foil and the bearing forces F_B induced by the latter. The pressure p is dependent on time t in dynamic problem (whirling motion of the journal) and the spatial coordinates; the circumferential $x = R\theta$ and the axial one z, all of them consisting the independent variables of this problem; thus, $p = p(x, z, t)$. The location of foil starting and ending angle (which are very similar to each other) is denoted by the angular coordinate χ. In this work $\chi = \pi/2$ and at this point the foil is considered without any deformation q.

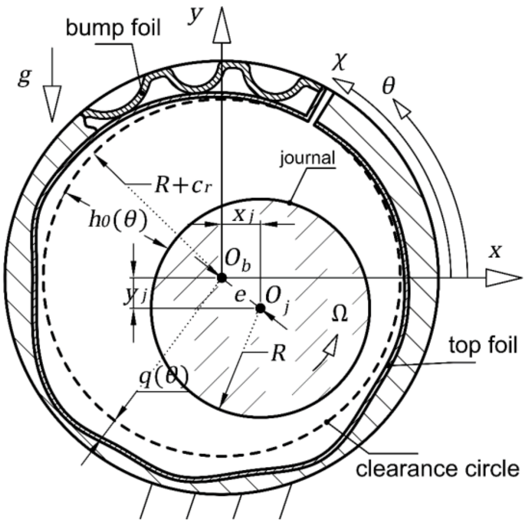

Fig. 2.1: Gas foil bearing representation: main components, geometry, operating parameters, and coordinate system

2.1.1 Reynolds Equation for the compressible flow

The assumptions introduced in the lubrication problem are quite common: a) Newtonian lubricating fluid, b) isothermal film, c) laminar flow, d) no-slip boundary conditions, e) continuum flow, f) negligible fluid inertia, g) ideal isothermal gas law ($p/\rho = const.$), h) negligible entrance and exit effects, i) negligible curvature ($R \gg c_r$). The Reynolds equation for compressible fluid and for an unsteady (whirling) motion of the journal is given in (1) [61], with respect to the journal and foil kinematics, and it is an implicit function of time:

$$\begin{gathered}\frac{\partial}{\partial x}\left[\frac{p(h_0+q)^3}{\mu}\frac{\partial p}{\partial x}\right]+\frac{\partial}{\partial z}\left[\frac{p(h_0+q)^3}{\mu}\frac{\partial p}{\partial z}\right] \\ -6\Omega R\frac{\partial}{\partial x}[p(h_0+q)]-12\frac{\partial}{\partial t}[p(h_0+q)]=0\end{gathered} \tag{1}$$

where p is the unknown gas pressure distribution, μ the dynamic viscosity of the fluid. The foil deflection q is added to h_0, see Fig. 2.1, which represents the fluid film height considered for a rigid wall and -again- can be evaluated as a function of angle θ and time t ($h_0 = h_0(\theta, t)$). The sum of these two variables represents the total height of the fluid film, $h = h_0 + q$. Eventually, the film thickness relation can be finally written as:

$$h(\theta,t)=h=\underbrace{c_r-x_j\cos\theta-y_j\sin\theta}_{h_0}+q \tag{2}$$

where c_r is the nominal clearance, θ is the angular absolute coordinate stating the -position within the lubricating zone between journal and top foil in circumferential direction, and $x_{j,}y_j$ the displacements of the journal. Applying (2) to (1), Reynolds equation renders:

$$\frac{\partial}{\partial x}\left(\frac{ph^3}{\mu}\frac{\partial p}{\partial x}\right)+\frac{\partial}{\partial z}\left(\frac{ph^3}{\mu}\frac{\partial p}{\partial z}\right)-6\Omega R\frac{\partial}{\partial x}(ph)-12\frac{\partial}{\partial t}(ph)=0 \tag{3}$$

The Reynolds equation is defined on the domain $\Pi = \{(x,z) \mid \chi R < x < 2\pi R + \chi R, 0 < z < L\}$, χ being the position of the foil fixation, and L the length of the bearing. The spatial coordinates $x = R\theta$ and z -mentioned in the beginning of this chapter are considered independent. Due to the very small dimensions of the film height in the radial direction, in comparison to the circumferential and axial, the fluid pressure p dependency to any variation on y-axis ($p \neq p(y)$) is neglected. No analytical solution for (3) can be extracted; therefore, an indicated approach to obtain the pressure distribution is a numerical one. For the numerical solution of (3), the Finite Difference Method (FDM) is applied. The domain Π is converted into a grid of $i = 1, \dots, N_x$ and $j = 1, \dots, N_z/2$ points, see Fig. 2.2, where i represents each point in the circumferential

[61] Baum C., Hetzler H., Schröders S., Leister T., Seemann W. (2020) A computationally efficient nonlinear foil air bearing model for fully coupled, transient rotor dynamic investigations. Tribol. Int. doi: https://doi.org/10.1016/j.triboint.2020.106434

direction, while j those in the axial. The chosen grid for the bearing model is $(N_x, N_z) = (29{,}10)$.

First order derivatives with respect to the spatial coordinates x, z are approximated by backward differences:

$$\begin{gathered} \boldsymbol{p_x = \frac{\partial p}{\partial x} \cong \frac{p_{i,j} - p_{i-1,j}}{\Delta x}, \qquad p_z = \frac{\partial p}{\partial z} \cong \frac{p_{i,j} - p_{i,j-1}}{\Delta z}} \\ \boldsymbol{h_x = \frac{\partial h}{\partial x} \cong \frac{h_i - h_{i-1}}{\Delta x}, \qquad h_z = \frac{\partial h}{\partial z} \cong 0} \end{gathered} \tag{4}$$

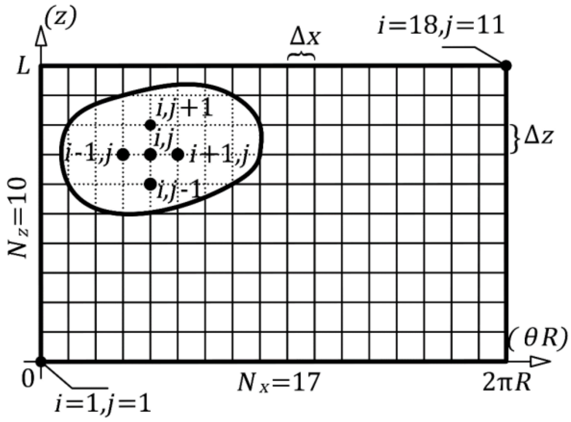

Fig. 2.2: Exemplary discretization grid for the application of Finite Difference Method in the solution of Reynolds equation for compressible flow

As (4) shows, the dependency of the fluid film height h on the axial direction is neglected. This can be figured out easily, since - according to (2) - when it comes to the spatial coordinates, the film height depends only on the foil deflection q. Since the latter is irrelevant to z-axis variations ($q = q(\theta) = q(i)$), the same applies to the former. Therefore, the film height is dependent only on the angle θ ($h = h(\theta) = h(\theta_i)$) which explains the chosen discretization concerning h_x and h_z. The second order derivatives are approximated by central differences, as shown in Eq. (5):

$$\boldsymbol{p_{xx} = \frac{\partial^2 p}{\partial x^2} \cong \frac{p_{i+1,j} - 2p_{i,j} + p_{i-1,j}}{\Delta x^2}, \qquad p_{zz} = \frac{\partial^2 p}{\partial z^2} \cong \frac{p_{i,j+1} - 2p_{i,j} + p_{i,j-1}}{\Delta z^2}} \tag{5}$$

where

$$\boldsymbol{\Delta x = \frac{2\pi R}{N_x}, \qquad \Delta z = \frac{L}{N_Z}} \tag{6}$$

Backward differences are used for the first order derivatives and central differences are used for the second order due the greater numerical stability that characterizes the former, even though it is a less accurate choice. Eventually, the Reynolds equation, after applying the FDM which led to (4) and (5) discretizations, is transformed into Eq. (7):

$$\boldsymbol{\frac{h^2}{\mu}\left[h(p_x^2 + p_z^2) + 3ph_x p_x + ph(p_{xx} + p_{zz})\right]} \tag{7}$$

$$-6\Omega R(hp_x + ph_x) - 12(h\dot{p} + p\dot{h}) = 0$$

where $\dot{p} = \frac{\partial p}{\partial t}$ and $\dot{h} = \frac{\partial h}{\partial t}$.

Eq. (7) can be solved explicitly for the time derivative $\dot{p}$ of the pressure at each grid point, while the time derivatives $\dot{h}$ of the film height can be defined analytically by differentiating (2):

$$\dot{h} = -\dot{x}_j \cos\theta - \dot{y}_j \sin\theta + \dot{q} \tag{8}$$

where $\dot{x}_j$,$\dot{y}_j$ the time derivatives of the journal's displacements, and $\dot{q}$ the time derivative of the foil deflection. Thus, after some math, (7) is written in Eq. (9):

$$\dot{p} = \frac{h}{12\mu}[h(p_x^2 + p_z^2) + 3ph_x p_x + ph(p_{xx} + p_{zz})] - \frac{\Omega R}{2}\left(p_x + \frac{p}{h}h_x\right) - \frac{p}{h}\dot{h} \tag{9}$$

Boundary and initial conditions of the problem should be defined. Ambient pressure is assumed at the starting angle of the foil, Eq. (10).

$$p(t, x = \chi R, z) = p(t, x = 2\pi R + \chi R, z) = p_0 \tag{10}$$

Taking into account the symmetry of the problem, there is another way to express the rest of the BC than the typical one. According to the latter, the fluid pressure is assumed to be equal to the ambient p_0 at the axial ends, $p(z = 0) = p(z = L) = p_0$. However, considering the aforementioned symmetry, the initial domain Π can be reduced to domain $\Pi' = \{(x, z) \mid \chi R < x < 2\pi R + \chi R, 0 < z < \frac{L}{2}\}$. In the present problem, the gap -theoretically mentioned in the beginning of this section and depicted at Fig. 2.1- of the top foil is positioned at $\chi = 0$ angle, which eventually transforms (10) into:

$$p(t, x = 0, z) = p(t, x = 2\pi R, z) = p_0 \tag{11}$$

and determines the final domain $\Pi' = \{(x, z) \mid 0 < x < 2\pi R, 0 < z < \frac{L}{2}\}$. Having each necessary modification implemented, the last two BCs will be:

$$p(t, x, z = 0) = p_0, \qquad \frac{\partial p(t, x, z)}{\partial z}\Big|_{z=\frac{L}{2}} = 0 \tag{12}$$

Regarding the initial conditions for the pressure and the foil deflection, these are expressed in Eq. (13):

$$p(t = 0, x, z) = p_0, \qquad q(t = 0, x) = 0 \tag{13}$$

Assuming that the gas pressure p is determined at all grid points (this is explained in Section 2.3), the bearing forces F_{Bx}, F_{By} evaluation may follow. The bearing forces, as shown subsequently in Chapter 3, signify an important factor in drawing conclusions for rotor-dynamic investigations. The GFB's forces equations are given by:

$$\boldsymbol{F_{Bx}} = -\int_{0}^{2\pi R}\int_{0}^{L}(\boldsymbol{p}-\boldsymbol{p_0})\cos\boldsymbol{\theta}\,\mathbf{dz}\,\mathbf{d}\boldsymbol{x} = -\int_{0}^{2\pi R}2\int_{0}^{\frac{L}{2}}(\boldsymbol{p}-\boldsymbol{p_0})\cos\boldsymbol{\theta}\,\mathbf{dz}\,\mathbf{d}\boldsymbol{x} \qquad \textbf{(14)}$$

$$\boldsymbol{F_{By}} = -\int_{0}^{2\pi R}\int_{0}^{L}(\boldsymbol{p}-\boldsymbol{p_0})\sin\boldsymbol{\theta}\,\mathbf{dz}\,\mathbf{d}\boldsymbol{x} = -\int_{0}^{2\pi R}2\int_{0}^{\frac{L}{2}}(\boldsymbol{p}-\boldsymbol{p_0})\sin\boldsymbol{\theta}\,\mathbf{dz}\,\mathbf{d}\boldsymbol{x} \qquad \textbf{(15)}$$

At this point, it is important to mention that it's quite common in GFBs for sub-ambient pressures to arise. These sub-ambient pressures can cause the top foil to separate from the bumps into a position in which the pressure on both sides of the pad is equalized. Heshmat et al. [62-63] introduced a set of boundary conditions accounting for this separation effect. More specifically, a simple Gümbel [64] boundary condition is imposed, meaning that sub-ambient pressures are discarded when integrating the pressure in Eqs. (14)-(15) to obtain the bearing force components F_{Bx}, F_{By}, essentially leaving the sub-ambient regions ineffective. In terms of numerical calculations, the assumption made by Heshmat [2-3] can be simply explained as following: in case fluid pressure p is lower than the ambient p_0, then the former should be considered equal to p_0. Then, as the train of thought unfolds, a fluid pressure equal to the ambient one would result to the fact that the overall bearing force $\overrightarrow{F_B} = \overrightarrow{F_{Bx}} + \overrightarrow{F_{By}}$ should be equal to zero ($F_{Bx} = F_{By} = 0$), which ultimately means that no foil deformation is going to be observed ($q = 0$). The same assumption about sub-ambient pressures applies to the evaluation of the mean pressure $p_{\boldsymbol{m}}$ over the length L of the bearing, a term introduced in the next Section of this Chapter.

In general, solving the dimensional (DM) form of a problem can be computationally expensive. Thus, a dimensionless (DL) expression of the equations of the model can be a decisive factor in order to enhance time and memory efficiency, and additionally (and most significant) a generic approach for the model and the results. The following transformations take place in order to define the dimensionless equations describing the problem. Firstly, the independent variables x, z are transformed into:

$$\overline{\boldsymbol{x}} = \boldsymbol{\theta} = \frac{\boldsymbol{x}}{\boldsymbol{R}}, \qquad \overline{\boldsymbol{z}} = \frac{\boldsymbol{z}}{\boldsymbol{L}} \qquad \textbf{(16)}$$

while the dependent variables of time and pressure into:

[62] H. Heshmat, J.A. Walowit, O. Pinkus (1983) Analysis of gas lubricated compliant thrust bearings, Journal of Lubrication Technology 105: 638–646.

[63] H. Heshmat, J.A. Walowit, O. Pinkus (1983) Analysis of gas-lubricated foil journal bearings, Journal of Lubrication Technology 10: 647–655.

[64] B.J. Hamrock (1994) Fundamentals of Fluid Film Lubrication, McGraw-Hill Series in Mechanical Engineering, McGraw-Hill Inc., NewYork.

$$\boldsymbol{\tau = \frac{p_0 {c_r}^2}{6\mu R^2} t = \Lambda t, \qquad \overline{p} = \frac{p}{p_0}} \tag{17}$$

where p_0 defines the ambient pressure. Secondly, the DL angular velocity of the journal is introduced:

$$\boldsymbol{\overline{\Omega} = \Lambda^{-1}\Omega} \tag{18}$$

where Ω is the rotational speed of the journal. The fluid height and foil deflection, as well as the journal (and its eccentricity) and disc displacements, are scaled by the clearance c_r which results to their dimensionless form:

$$\boldsymbol{\overline{h} = \frac{h}{c_r}, \qquad \overline{q} = \frac{q}{c_r}} \tag{19}$$

$$\boldsymbol{\overline{x}_j = \frac{x_j}{c_r}, \qquad \overline{y}_j = \frac{y_j}{c_r}, \qquad \varepsilon = \frac{e}{c_r} = \sqrt{\overline{x}_j^2 + \overline{y}_j^2}, \qquad \overline{x}_d = \frac{x_d}{c_r}, \qquad \overline{y}_d = \frac{y_d}{c_r}} \tag{20}$$

After applying the appropriate transformations to (3), the DL Reynolds equation is given by:

$$\boldsymbol{\frac{\partial}{\partial \overline{x}}\left(\overline{p}\overline{h}^3 \frac{\partial \overline{p}}{\partial \overline{x}}\right) + \kappa^2 \frac{\partial}{\partial \overline{z}}\left(\overline{p}\overline{h}^3 \frac{\partial \overline{p}}{\partial \overline{z}}\right) - \Omega \frac{\partial}{\partial \overline{x}}(\overline{p}\overline{h}) - 2\frac{\partial}{\partial \tau}(\overline{p}\overline{h}) = 0} \tag{21}$$

where

$$\boldsymbol{\kappa = R/L} \tag{22}$$

$$\boldsymbol{\overline{h} = 1 - \overline{x}_j \cos\theta - \overline{y}_j \sin\theta + \overline{q}} \tag{23}$$

on the DL domain $\overline{\Pi}' = \{(\overline{x}, \overline{z}) \mid \chi < \overline{x} < 2\pi + \chi, 0 < z < \frac{1}{2}\}$.

The respective line of reasoning, followed in the DM form, will take place regarding the DL dynamic problem. After applying the transformations (18)-((20) to the first order derivatives (4), the DL approximation on them is given:

$$\boldsymbol{\begin{gathered} \overline{p}_x = \frac{\partial \overline{p}}{\partial \overline{x}} \cong \frac{\overline{p}_{i,j} - \overline{p}_{i-1,j}}{\Delta \overline{x}}, \qquad \overline{p}_z = \frac{\partial \overline{p}}{\partial \overline{z}} \cong \frac{\overline{p}_{i,j} - \overline{p}_{i,j-1}}{\Delta \overline{z}} \\ \overline{h}_x = \frac{\partial \overline{h}}{\partial \overline{x}} \cong \frac{\overline{h}_i - \overline{h}_{i-1}}{\Delta \overline{x}}, \qquad \overline{h}_z \cong 0 \end{gathered}} \tag{24}$$

while for the second order derivatives (5), approximated by central differences,

$$\boldsymbol{\overline{p}_{xx} = \frac{\partial^2 \overline{p}}{\partial \overline{x}^2} \cong \frac{\overline{p}_{i+1,j} - 2\overline{p}_{i,j} + \overline{p}_{i-1,j}}{\Delta \overline{x}^2}} \tag{25}$$

$$\overline{\boldsymbol{p}}_{zz} = \frac{\partial^2 \overline{\boldsymbol{p}}}{\partial z^2} \cong \frac{\overline{\boldsymbol{p}}_{i,j+1} - 2\overline{\boldsymbol{p}}_{i,j} + \overline{\boldsymbol{p}}_{i,j-1}}{\Delta \overline{z}^2}$$

where,

$$\Delta \overline{x} = \frac{2\pi}{N_x}, \qquad \Delta \overline{z} = \frac{1}{N_z} \tag{26}$$

Therefore, the DL Reynolds equation (21), solved for the time derivative of the fluid pressure $\overline{p}' = \frac{\partial \overline{p}}{\partial \tau}$, will be:

$$\begin{aligned} \overline{\boldsymbol{p}}' = \frac{1}{2}\overline{\boldsymbol{h}}[\overline{\boldsymbol{h}}\left(\overline{\boldsymbol{p}}_x^2 + k^2\overline{\boldsymbol{p}}_z^2\right) + 3\overline{\boldsymbol{p}}\overline{\boldsymbol{h}}_x\overline{\boldsymbol{p}}_x + \overline{\boldsymbol{p}}\overline{\boldsymbol{h}}(\overline{\boldsymbol{p}}_{xx} + \overline{\boldsymbol{p}}_{zz})] \\ -\frac{\Omega R}{2}(\overline{\boldsymbol{p}}_x + (\overline{\boldsymbol{p}}/\overline{\boldsymbol{h}})\overline{\boldsymbol{h}}_x) - \overline{(\boldsymbol{p}/\boldsymbol{h})}\,\overline{\boldsymbol{h}}' \end{aligned} \tag{27}$$

where $\overline{h}'$ the DL time derivative of the fluid height defined analytically as:

$$\overline{\boldsymbol{h}}' = -\overline{\boldsymbol{x}}_j{}' \cos\boldsymbol{\theta} - \overline{\boldsymbol{y}}_j{}' \sin\boldsymbol{\theta} + \overline{\boldsymbol{q}}' \tag{28}$$

Boundary and initial conditions for the DL form of the problem will be expressed as:

$$\overline{\boldsymbol{p}}(\boldsymbol{\tau}, \overline{\boldsymbol{x}} = \boldsymbol{0}, \overline{\boldsymbol{z}}) = \overline{\boldsymbol{p}}(\boldsymbol{\tau}, \overline{\boldsymbol{x}} = \boldsymbol{2\pi}, \overline{\boldsymbol{z}}) = \boldsymbol{1} \tag{29}$$

$$\overline{\boldsymbol{p}}\left(\boldsymbol{\tau}, \overline{\boldsymbol{x}}, \overline{\boldsymbol{z}} = \frac{\boldsymbol{1}}{\boldsymbol{2}}\right) = \boldsymbol{1}, \qquad \frac{\partial}{\partial z}\overline{\boldsymbol{p}}(\boldsymbol{\tau}, \overline{\boldsymbol{x}}, \overline{\boldsymbol{z}} = \boldsymbol{0}) = \boldsymbol{0} \tag{30}$$

$$\overline{\boldsymbol{p}}(\boldsymbol{\tau} = \boldsymbol{0}, \overline{\boldsymbol{x}}, \overline{\boldsymbol{z}}) = \overline{\boldsymbol{p}_0}', \qquad \overline{\boldsymbol{q}}(\boldsymbol{\tau} = \boldsymbol{0}, \overline{\boldsymbol{z}}) = \overline{\boldsymbol{q}_0}' \tag{31}$$

The DL bearing force's components ($\overrightarrow{F_B} = \overrightarrow{F_{Bx}} + \overrightarrow{F_{By}}$), after evaluating the DL fluid pressure $\overline{p}$, can be determined by:

$$\overline{\boldsymbol{F}}_{Bx} = -\int_0^{2\pi}\int_0^{\frac{1}{2}} 2(\overline{\boldsymbol{p}} - 1)\cos\overline{\boldsymbol{x}}\,\mathbf{d}\overline{\boldsymbol{z}}\,\mathbf{d}\overline{\boldsymbol{x}} \tag{32}$$

$$\overline{\boldsymbol{F}}_{By} = -\int_0^{2\pi}\int_0^{\frac{1}{2}} 2(\overline{\boldsymbol{p}} - 1)\sin\overline{\boldsymbol{x}}\,\mathbf{d}\overline{\boldsymbol{z}}\,\mathbf{d}\overline{\boldsymbol{x}} \tag{33}$$

where a multiplication of the components $\overline{F}_{Bx}, \overline{F}_{By}$ with $p_0 LR$ provides the respective DM components F_{Bx}, F_{By}.

2.1.2 Simplified model for the bump foil structure

The simplified model for the bump foil structure is depicted at Fig. 2.3 and Fig. 2.4. The structure consists of rigid, massless, beam-like elements with one finite dimension in axial direction and no coupling of the elements in the circumferential one. The top foil of the bearing is not covering a complete cylinder; a single gap can be found at $x = \chi R$ angle where foils are clamped to the bearing housing, see Fig. 2.1. Regarding the modelling of the structure, each element is supported by a nonlinear spring and a linear damper in parallel, which are connected with the rigid part of the bearing, the housing. These elements are assumed to be only a function of the spatial coordinate x and time t ($q = q(x,t)$). The geometry properties of the foil play a crucial role in determining the foil deflection. More specifically, the pitch s_0, the half-length l_0, the thickness t_b (see Fig. 2.3) and Poisson's ratio v are vital in order to evaluate the dimensionless compliance $\overline{\alpha}_f$ of the foil.

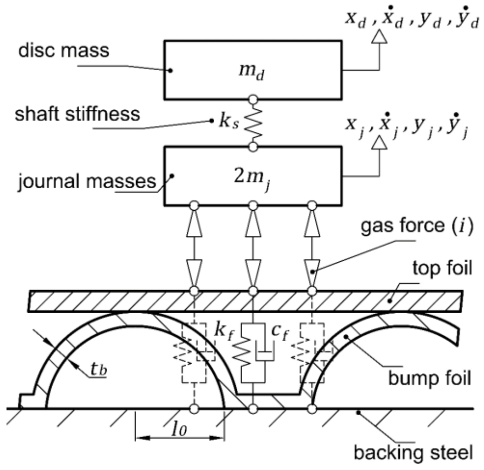

Fig. 2.3: Disc-shaft-journal-gas-top foil-bump foil model representation

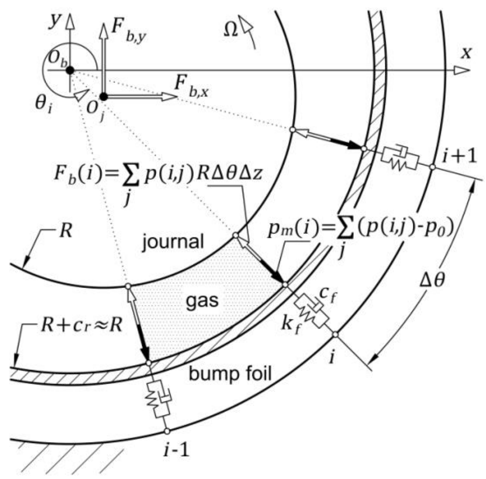

Fig. 2.4: Depiction of mean pressure p_m applied over the bearing length L and bearing force F_B

The algebraic relation between compliance per area $\overline{\alpha}_f$ and the properties of the foil is given by [65]:

$$\overline{\alpha}_f = 2p_0\left(\frac{l_0}{t_b}\right)^3 (1 - v^2)\frac{s_0}{c_r E} \tag{34}$$

Therefore, the dimensionless foil stiffness per area can be found:

$$\overline{k}_f = \frac{1}{\overline{\alpha}_f} \tag{35}$$

while the dimensional foil stiffness per area can be extracted by multiplying (35) with the ratio p_0/c_r, or -expressed in words- the ratio of the ambient pressure over the nominal clearance in (36).

$$k_f = \frac{p_0}{\overline{\alpha}_f c_r} \tag{36}$$

In addition, the damping coefficient (per area) c_f of the bump foil is related to the stiffness k_f (per area) and the loss factor η of the foil structure as:

[65] Bhore S.P., Darpe A.K. (2013) Nonlinear dynamics of flexible rotor supported on the gas foil journal bearings. J. of Sound and Vib. 332:5135-5150

$$\boldsymbol{c_f = \eta k_f} \tag{37}$$

The ODE connecting the fluid pressure p with the foil deflection q is [66]:

$$\boldsymbol{c_f \dot{q}_k + k_f q_k = p_m} \tag{38}$$

which can be solved explicitly for the time derivatives of the deflection $\dot{q}_k$ as shown below:

$$\boldsymbol{\dot{q}_k = \frac{p_m - k_f q_k}{c_f}} \tag{39}$$

where

$$\boldsymbol{p_m = \int_{-\frac{L}{2}}^{\frac{L}{2}} (p - p_0)\,\mathrm{d}z} \tag{40}$$

is the arithmetic mean pressure over the length L of the bearing, or - in other words - the pressure applied in the axial direction on each element k of the foil. If $p_m < 0$, which indicates that a state of sub-pressure prevails (pressure applied on foil elements lower than the ambient p_0), p_m will be considered equal to zero ($p_m = 0$), as explained in the previous paragraphs. Under these circumstances, (38) will be transformed into:

$$\boldsymbol{c_f \dot{q}_k + k_f q_k = 0 \Rightarrow \dot{q}_k = -\frac{k_f}{c_f} q_k} \tag{41}$$

Due to the symmetry and the domain Π' transformation, the mean pressure over axial direction can be written as:

$$\boldsymbol{p_m = \int_{-\frac{L}{2}}^{\frac{L}{2}} (p - p_0)\,\mathrm{d}z = 2\int_{0}^{\frac{L}{2}} (p - p_0)\,\mathrm{d}z} \tag{42}$$

With regard to the DL form, having already introduced the dimensionless Reynolds equation, the transformed ODE for the bump foil structure model (38) - now on the DL domain $\overline{\Pi}' = \{(\overline{x}, \overline{z}) |\, 0 < \overline{x} < 2\pi, 0 < \overline{z} < \frac{1}{2}\}$ - will be:

$$\boldsymbol{\overline{c}_f \overline{q}_k' + \overline{k}_f \overline{q}_k = \overline{p}_m} \tag{43}$$

[66] Larsen J.S., Santos I.F. (2015) On the nonlinear steady-state response of rigid rotors supported by air foil bearings-Theory and experiments. J. of Sound and Vib. 346:284-297

where $\overline{q}_k$ the DL foil deflection, see (39), $\overline{k_f}$ the DL foil stiffness coefficient, see (35), $\overline{c}_f$ the DL foil damping coefficient given by:

$$\overline{\boldsymbol{c}}_{\boldsymbol{f}} = \boldsymbol{\eta}\overline{\boldsymbol{k}}_{\boldsymbol{f}} \tag{44}$$

and $\overline{p}_m$ the averaged DL pressure, defined after the transformations (16) and (17) applied to (42):

$$\overline{\boldsymbol{p}}_{\boldsymbol{m}} = 2\int_0^{\frac{1}{2}} (\overline{\boldsymbol{p}} - 1)\,\mathrm{d}\overline{\boldsymbol{z}} = \frac{\boldsymbol{p}_{\boldsymbol{m}}}{\boldsymbol{p}_0 \boldsymbol{L}} \tag{45}$$

Eq. (43) can be solved explicitly for the time derivatives of the deflection $\overline{q}_k'$ as shown below where $\overline{k}_f, \overline{c}_f, \overline{p}_m$ given by (35), (44) and (45) respectively.

$$\overline{\boldsymbol{q}}_{\boldsymbol{k}}' = \frac{\overline{\boldsymbol{p}}_{\boldsymbol{m}} - \overline{\boldsymbol{k}}_{\boldsymbol{f}}\overline{\boldsymbol{q}}_{\boldsymbol{k}}}{\overline{\boldsymbol{c}}_{\boldsymbol{f}}} \tag{46}$$

Having introduced both the DM and the DL form of the Reynolds equation, the method followed in order to evaluate the fluid pressure and the bearing forces, as well as the equations describing the foil structure, it would be useful to provide a visualization of the behavior of this model. A static problem is considered, meaning that the time derivatives of the fluid pressure $\dot{p}$, journal's displacements $\dot{x}_j, \dot{y}_j$, and the foil's deformation $\dot{q}_k$ will be equal to zero. The DM form of the aforementioned model was chosen in order to perform several case-studies, and the appropriate transformations took place after the executions were over so as to introduce the DL version of the variables, in the figures below. The computation of the results for the static problem was achieved by a Newton-Raphson method implemented by the 'fsolve' solver in Matlab, on an i7 processor with 8 GB RAM memory.

The main object of these simulations, more specifically, is to observe the bearing's static behavior with regard to its foil compliance and the rotational speed of the journal. In other words, these make up the changing operational parameters of this process. In Table 2.1, the numeric values of the constant parameters of the static problem are introduced:

The comparative analysis was executed for three different cases of the DL compliance $\overline{\alpha}_f$; a stiff foil where $\overline{\alpha}_f$ = 0.01, a compliant foil where $\overline{\alpha}_f$ = 1, and for the median value of compliancy where $\overline{\alpha}_f$ = 0.1. For each case, three different values of the rotational speed were considered, with the first being Ω = 1650 r/s, the second Ω = 6550 r/s and the last one Ω = 13000 r/s. For ease of reference and the sake of uniformity in the final results, it would be more appropriate to express the three values of the rotational speed in their DL form. Therefore, for the first case the DL value of the rotational speed would be $\overline{\Omega} = 1$, for the second $\overline{\Omega} = 4$, and for the third one $\overline{\Omega} = 8$. The position of the foil fixation was assumed at angle θ = 90°.

Table 2.1: Constant parameters for the case-study analysis in the static problem

Parameters	Values
Ambient pressure, p_0 (N/m^2)	10^5
Viscosity, μ (mNs/m^2)	0.018
Radius of the journal, R (mm)	19.086
Length of the bearing, L (mm)	38.172
Clearance, c_r (μm)	36
Loss factor, η	0.001
Sommerfeld number S range	S_{min} = 0.05 S_{min} = 1.5

The Sommerfeld number S (range shown in Table 2.1) is defined by the following equation with Ω in (rad/s) and all the rest magnitudes defined also in SI $(Pa \cdot s, m)$:

$$\boldsymbol{S} = \frac{\mathbf{1}}{\mathbf{2}\boldsymbol{\pi}}\left(\frac{\boldsymbol{R}}{\boldsymbol{c_r}}\right)^{\mathbf{2}} \frac{\boldsymbol{\mu}\mathbf{\Omega LD}}{\mathbf{W}} \qquad \textbf{(47)}$$

where W marks the load applied on the bearing. As it can be easily observed, it contains all the design parameters of the bearing and one may draw several conclusions when it comes to investigating how the journal and foil respond in case of applying different loads. Scaling (47) by $p_0 LR$ renders the DL form of the applied load, denoted by $\overline{W}$. Fig. 2.5 depicts the influence of load $\overline{W}$ in journal's displacement $\overline{y}_j$, while Fig. 2.6 the Sommerfeld's number S with respect to journal eccentricity ε. The process followed for the extraction of these figures consists of several runs, where the compliance $\overline{\alpha}_f$ and rotational speed $\overline{\Omega}$ were constant ($\overline{\alpha}_f = \{0.01, 0.1, 1\}$ and $\overline{\Omega} = \{1, 4, 8\}$ respectively) and S varying in the range $S = [0.05, 1.5]$.

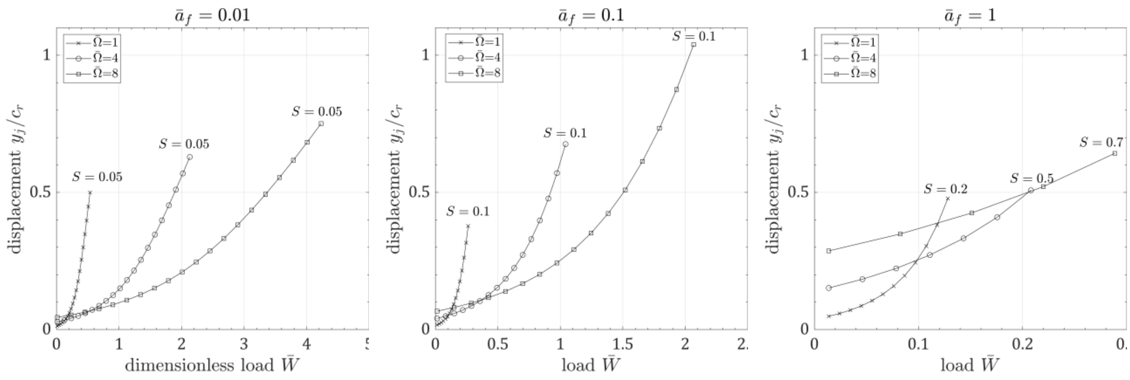

(a) (b) (c)

Fig. 2.5: Vertical displacement $\overline{y}_j$ over load $\overline{W}$; (a) $\overline{\alpha}_f$ = 0.01, (b) $\overline{\alpha}_f$ = 0.1, (c) $\overline{\alpha}_f$ = 1;
× $\overline{\Omega}$ = 1, □ $\overline{\Omega}$ = 4, ○ $\overline{\Omega}$ = 8

Eq. (47) demonstrates, the alteration of load $\overline{W}$, is solely dependent on the alteration of the inversely proportional variable S. Starting from $S_{max} = 1.5$ in both figures, for each case of $\overline{\alpha}_f$ and $\overline{\Omega}$, two types of conclusions can be drawn. First, by comparing the three curves that each subfigure contains, one can clearly observe that for a certain value of $\overline{\alpha}_f$ and by increasing $\overline{\Omega}$, while S remains constant, $\overline{W}$ inevitably rises -

affirming (47) - and ε as well. One of the significant observations, though, is that this increase takes place in a non-linear way, proving the non-linearity of this model, caused by the induced bearing forces. Second, by examining each one of the three subfigures with respect to the other, and for the same arithmetic value of $\overline{\Omega}$ and S, it can be noticed that when $\overline{\alpha}_f$ increases, the vertical displacement $\overline{y}_j$ and eccentricity ε may be also increasing, but the DL load $\overline{W}$ follows an opposite path. In other words, as the foil becomes more elastic, the eccentricity of the journal and its components (horizontal and vertical displacements) increase, while the bearing can take lower loads. This can be seen clearly in Fig. 2.7c, where S cannot reach lower values than $S = 0.2$, in comparison to the other two cases (a), (b), due to the fact that the foil is too elastic to manage taking higher loads and produce additional results. As the rotational speed of the journal rises, the foil is deformed even more, deflecting by two or even three times -witnessed in the first case where $\overline{\alpha}_f$ = 0.01- the radius clearance c_r. Regarding the induced pressure, Fig. 2.7 provides visualization of how it is applied over the journal and foil structure, forcing the top foil to be deformed by this way averting any undesirable contact between the journal and the bearing. Apparently, it is maximized at $180° \leq \theta \leq 270°$ in all cases, while it is equal to the ambient pressure p_0 around the foil fixation point (again at θ = 90° for the static problem).

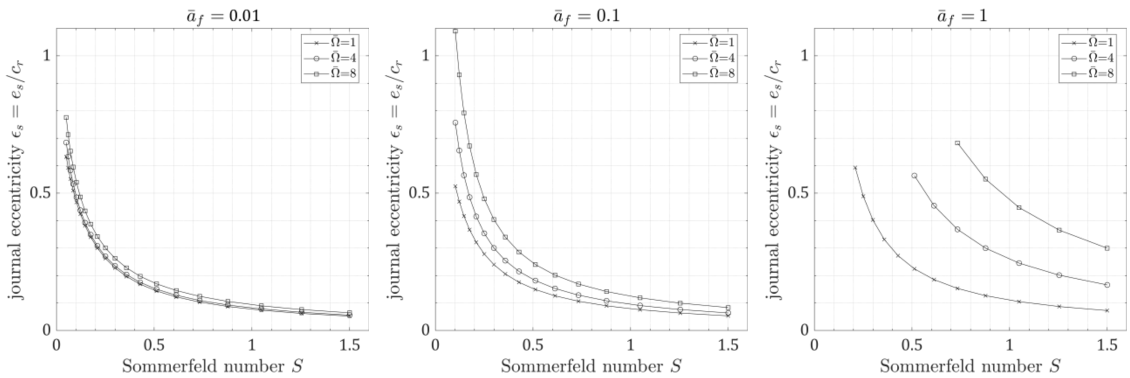

(a) (b) (c)

Fig. 2.6: Journal's eccentricity ε over Sommerfeld number S;
(a) $\overline{\alpha}_f$ = 0.01, (b) $\overline{\alpha}_f$ = 0.1, (c) $\overline{\alpha}_f$ = 1; × $\overline{\Omega}$ = 1, □ $\overline{\Omega}$ = 4, ○ $\overline{\Omega}$ = 8

A representation of the journal's locus, i.e. the trajectory that the equilibrium points form after each of the aforementioned runs is executed, the foil deformation and the pressure distribution, applied between the journal and the top foil, is depicted at Fig. 2.7. As Sommerfeld number S decreases, in all cases, the equilibrium points follow a linear path in the beginning.

In the figures below, a three-dimensional (3D) representation of the pressure distribution is given for the three chosen cases of compliance $\overline{\alpha}_f$, while the dimensionless rotating speed $\overline{\Omega}$ is considered $\overline{\Omega} = 4$, and a sensitivity analysis takes place so as to examine the influence of the discretization grid (N_x, N_z) with respect to the pressure. More specifically, for three different sets of discretization points, the maximum pressure that prompts each time is being compared to the respective maximum pressure values that the other two sets give. The line connecting the data points is almost parallel to the horizontal semi-axis of the figure, meaning that almost no difference is detected in the arithmetic values of the maximum pressure of each case. A discretization grid of (N_x, N_z) = (29,10) is considered reliable and will be applied in the dynamic problem.

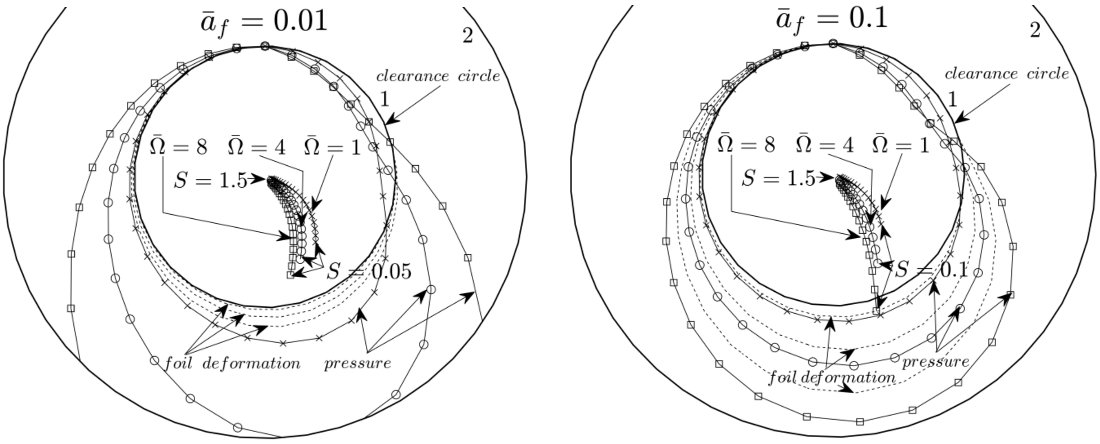

(a) (b) (c)

Fig. 2.7: Representation of journal's locus, foil deformation $\bar{q}$ and pressure distribution $\bar{p}$;
▬ Clearance circle, --- Foil deformation, — Pressure
(a) $\overline{\alpha}_f$ = 0.01, (b) $\overline{\alpha}_f$ = 0.1, (c) $\overline{\alpha}_f$ = 1; × $\overline{\Omega}$ = 1, □ $\overline{\Omega}$ = 4, ○ $\overline{\Omega}$ = 8

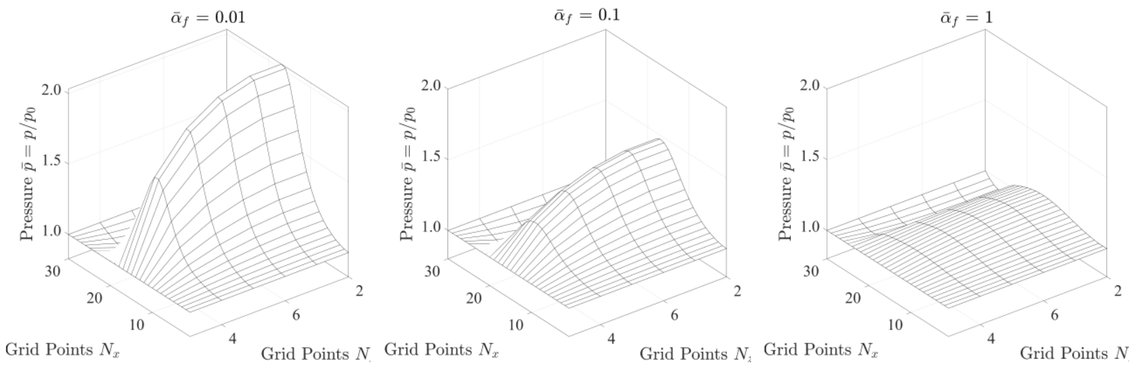

(a) (b) (c)

Fig. 2.8: Pressure $\overline{p}$ with respect to the foil compliance $\overline{\alpha}_f$ for $\overline{\Omega}$ = 4; (a) $\overline{\alpha}_f$ = 0.01, (b) $\overline{\alpha}_f$ = 0.1, (c) $\overline{\alpha}_f$ = 1

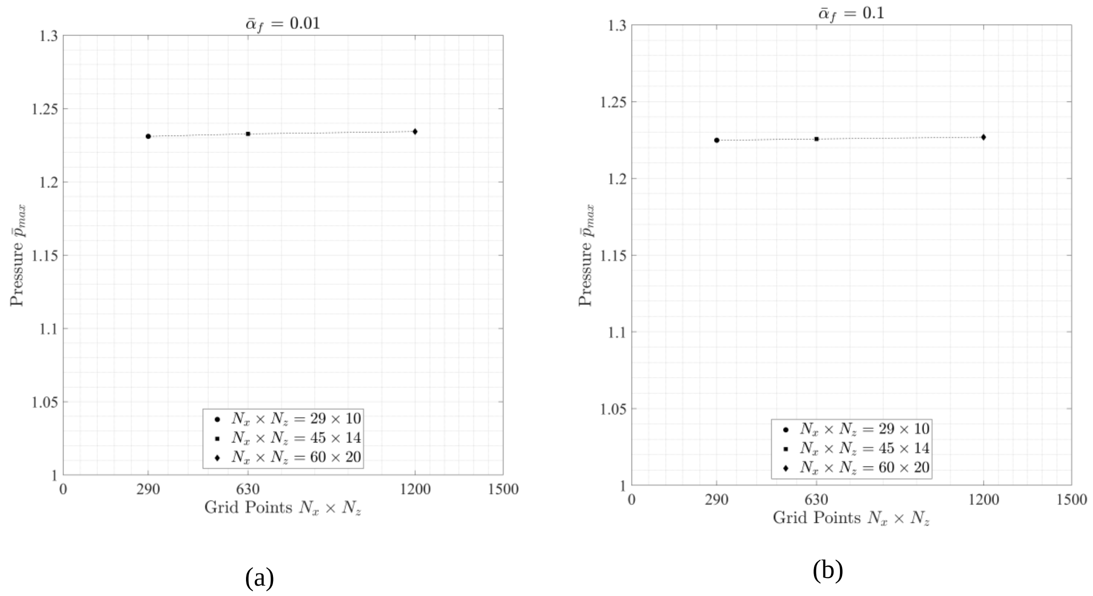

Fig. 2.9: Sensitivity analysis with regard to maximum applied pressure $\overline{p}_{max}$ over different discretization grids; (a) $\overline{a}_f$ = 0.01, (b) $\overline{a}_f$ = 0.1; ● $N_x \times N_z$ = 29 × 10, ■ $N_x \times N_z$ = 45 × 14, ♦ $N_x \times N_z$ = 60 × 20

2.2 Model of the flexible rotor

Fig. 2.10 shows a symmetric flexible Jeffcott rotor carrying a disc mass m_d at its center and two journal masses m_j at its ends. The rotor's shaft is considered elastic. The coordinates $O_d(x_d, y_d)$ and $O_j(x_j, y_j)$ represent the geometric centers of the disc and the journal respectively and make up the four degrees of freedom (4-DOF) of the rotor.

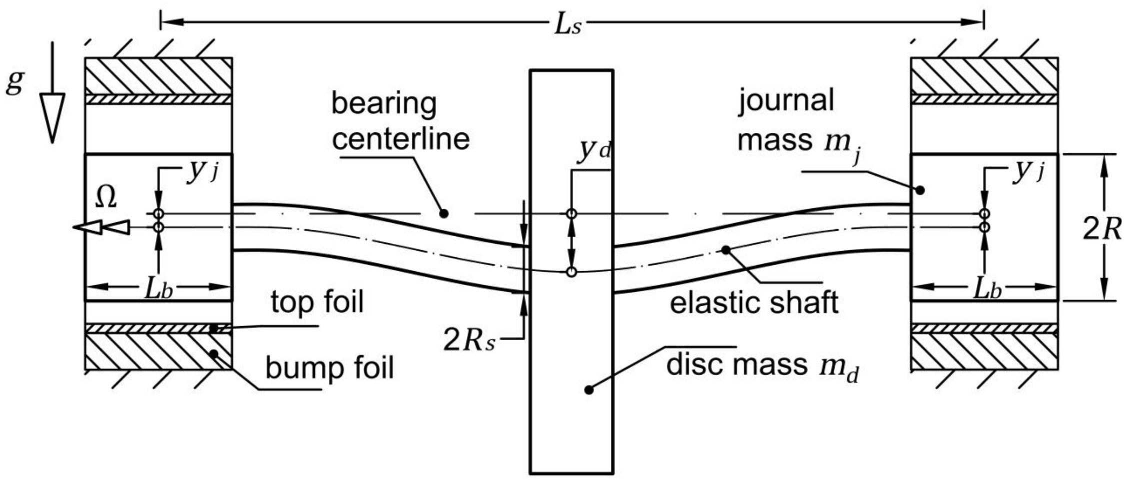

Fig. 2.10: Representation of a symmetric flexible Jeffcott rotor mounted on two identical bearings

The equations of the Jeffcott rotor are expressed, based on Fig. 2.3 modelling, and solved for the second order derivatives of the journal's and disc's displacements:

- Journal

$$2m_j\ddot{x}_j - k_s(x_d - x_j) = 2F_{Bx} \Rightarrow \ddot{x}_j = \frac{k_s(x_d - x_j)}{2m_j} + \frac{F_{Bx}}{m_j} \tag{48}$$

$$2m_j\ddot{y}_j - k_s(y_d - y_j) = 2F_{By} - 2m_j g \Rightarrow \ddot{y}_j = \frac{k_s(y_d - y_j)}{2m_j} + \frac{F_{By}}{m_j} - g \tag{49}$$

- Disc

$$m_d\ddot{x}_d + k_s(x_d - x_j) = m_d F_{Ux} \Rightarrow \ddot{x}_d = -\frac{k_s(x_d - x_j)}{m_d} + F_{Ux} \tag{50}$$

$$m_d\ddot{y}_d + k_s(y_d - y_j) = m_d F_{Uy} - m_d g \Rightarrow \ddot{y}_d = -\frac{k_s(y_d - y_j)}{m_d} + F_{Uy} - g \tag{51}$$

where k_s is the shaft stiffness coefficient,

$$F_i = F_i(x_j, y_j, x_d, y_d, \dot{x}_j, \dot{y}_j, \dot{x}_d, \dot{y}_d, \Omega, t), \qquad i = x, y \tag{52}$$

The bearing forces, mentioned in section 2.1.1, and F_{Ux}, F_{Uy} the components of the unbalance force defined as:

$$\begin{aligned} F_{Ux} &= \mathrm{e}[\Omega^2 \cos\varphi_r + \alpha \sin\varphi_r] \\ F_{Uy} &= \mathrm{e}[\Omega^2 \sin\varphi_r - \alpha \cos\varphi_r] \end{aligned} \tag{53}$$

with e being the unbalance eccentricity, g the gravitational constant, φ_r the journal's angle of rotation, Ω $(= \dot{\varphi}_r)$ the journal's angular velocity, and $\ddot{\varphi}_r$ $(= \alpha)$ the journal's angular acceleration. The shaft stiffness coefficient k_s has a physical dimension of force per unit length (N/m), and is given by:

$$k_s = \frac{\bar{k}_s m_d p_0^2 {c_r}^4}{36\mu^2 R^4} \tag{54}$$

where $\bar{k}_s$ is the dimensionless shaft stiffness coefficient and its numerical values will be determined in the case-studies performed in chapter 3.

For the run-up simulations, the angle of rotation -and its derivatives as well- are expressed by the following relations where α is constant:

$$\varphi_r = \frac{1}{2}\alpha t^2 \Rightarrow \dot{\varphi}_r = \Omega = \alpha t \Rightarrow \ddot{\varphi}_r = \alpha \tag{55}$$

Regarding the DL form of the Jeffcott rotor's model, the transformation process began by applying (20) to coordinates x_j, y_j, x_d, y_d and performing the appropriate differentiations in time τ, as shown below in (56)-(57) group of equations:

$$\bar{x}_i = \frac{x_i}{c_r} \Rightarrow \bar{x}_i' = \frac{\partial}{\partial\tau}\left(\frac{x_i}{c_r}\right) = \frac{\partial}{\partial t}\frac{\partial t}{\partial \tau}\left(\frac{x_i}{c_r}\right) = \frac{\partial}{\partial t}\left(\frac{x_i}{c_r}\right)\frac{\partial t}{\partial \tau} = \frac{\dot{x}_i}{c_r}\frac{6\mu R^2}{p_0 {c_r}^2} \tag{56}$$

$$\Rightarrow \overline{x}_i' = \frac{6\mu R^2}{p_0 {c_r}^3}\dot{x}_i \Rightarrow \overline{x}_i'' = \frac{\partial \overline{x}_i'}{\partial \tau} \Rightarrow \overline{x}_i'' = \frac{36\mu^2 R^4}{{p_0}^2 {c_r}^5}\ddot{x}_i$$

Similarly, the DL derivatives of y_i displacements are defined as:

$$\overline{y}_i' = \frac{6\mu R^2}{p_0 {c_r}^3}\dot{y}_i \Rightarrow \overline{y}_i'' = \frac{36\mu^2 R^4}{{p_0}^2 {c_r}^5}\ddot{y}_i \tag{57}$$

where $i = j, d$. Eventually, the DL equations of the motion of the Jeffcott rotor, again solved for the second order terms after applying the afore written transformations to (48)-(51), are:

- Journal

$$\overline{x}_j'' = \frac{m_d}{2m_j}\overline{k}_s(\overline{x}_d - \overline{x}_j) + \xi \overline{F}_{Bx} \tag{58}$$

$$\overline{y}_j'' = \frac{m_d}{2m_j}\overline{k}_s\left(\overline{y}_d - \overline{y}_j\right) + \xi \overline{F}_{By} - \sigma \tag{59}$$

- Disc

$$\overline{x}_d'' = -\overline{k}_s(\overline{x}_d - \overline{x}_j) + \overline{F}_{Ux} \tag{60}$$

$$\overline{y}_d'' = -\overline{k}_s\left(\overline{y}_d - \overline{y}_j\right) + \overline{F}_{Uy} - \sigma \tag{61}$$

where $\overline{k}_s$ the DL stiffness coefficient of the shaft, $\overline{F}_{Bx}, \overline{F}_{By}$ the DL bearing forces given by (32)-(33), ξ and σ DL parameters defined as:

$$\xi = \frac{36\mu^2 L R^5}{m_j p_0 {c_r}^5}, \qquad \sigma = \frac{36\mu^2 R^4 g}{{p_0}^2 {c_r}^5} \tag{62}$$

and

$$\begin{aligned} \overline{F}_{Ux} &= \varepsilon[\overline{\Omega}^2 \cos\overline{\varphi}_r + \overline{\alpha}\sin\overline{\varphi}_r] \\ \overline{F}_{Uy} &= \varepsilon[\overline{\Omega}^2 \sin\overline{\varphi}_r - \overline{\alpha}\cos\overline{\varphi}_r] \end{aligned} \tag{63}$$

the DL unbalance forces, with ε being the DL unbalance eccentricity given by:

$$\varepsilon = \frac{e}{c_r} \tag{64}$$

$\overline{\Omega}$ the DL angular velocity, see (18), and

$$\overline{\alpha} = \Lambda^{-2}\alpha, \qquad \overline{\varphi}_r = \frac{1}{2}\overline{\alpha}\tau^2 \tag{65}$$

the DL, constant angular acceleration given as a function of the DM angular acceleration α, and $\overline{\varphi}_r$ the angle of rotation respectively.

2.3 Composition and solution of the dynamic system

To summarize, the compliant gas foil bearing model is expressed as an Initial Boundary Value Problem described by two coupled nonlinear differential equations; the Reynolds equation which is a PDE of the fluid pressure p as a function of three independent variables -two of them being the spatial coordinates x, z and the third one, the time t-, and an ODE describing the deflection of the foil q, as a function of time t. The latter has to be solved multiple times in a gas foil bearing, since it takes into account one beam-like element each time, located in the circumference of the bearing, see Figs. 2.3 and 2.4.

The collocation points in which the gas pressure $p_{i,j}$ and the foil deflection q_i are evaluated (see Figs. 2.2-2.4), can be now introduced as a state-space vector [2]:

$$\boldsymbol{x_B} = [\boldsymbol{p_{1,1}}, \dots, \boldsymbol{p}_{\boldsymbol{N_x}, \frac{\boldsymbol{N_z}}{2}}, \boldsymbol{q_1}, \dots, \boldsymbol{q_{N_x}}]^{\boldsymbol{T}}, \qquad \boldsymbol{x_B} \in \mathbb{R}^{\left(\frac{N_z}{2}+1\right)N_x} \tag{66}$$

Eventually, the discretized bearing model is going to be a nonlinear system of coupled ODEs of 1st order:

$$\dot{\boldsymbol{x}}_{\boldsymbol{B}} = \boldsymbol{f}(\boldsymbol{x_B}), \qquad \boldsymbol{f}: \mathbb{R}^{\left(\frac{N_z}{2}+1\right)N_x} \to \mathbb{R}^{\left(\frac{N_z}{2}+1\right)N_x} \tag{67}$$

where $(N_x, N_z) = (29{,}10)$ and:

$$\dot{\boldsymbol{x}}_{\boldsymbol{B}} = [\dot{\boldsymbol{p}}_{\boldsymbol{1,1}}, \dots, \dot{\boldsymbol{p}}_{\boldsymbol{N_x}, \frac{\boldsymbol{N_z}}{2}}, \dot{\boldsymbol{q}}_{\boldsymbol{1}}, \dots, \dot{\boldsymbol{q}}_{\boldsymbol{N_x}}]^{\boldsymbol{T}} \tag{68}$$

The same process is being followed for the Jeffcott rotor model's ODEs. A state-space vector is introduced for the displacements x_j, y_j, x_d, y_d of the journal and the disc respectively, and their time derivatives $\dot{x}_j, \dot{y}_j, \dot{x}_d, \dot{y}_d$, where:

$$\begin{gathered} \boldsymbol{x_j = y(1)},\ \dot{\boldsymbol{x}}_{\boldsymbol{j}} = \boldsymbol{x_{j_t} = y(2)},\ \ \boldsymbol{y_j = y(3)},\ \dot{\boldsymbol{y}}_{\boldsymbol{j}} = \boldsymbol{y_{j_t} = y(4)} \\ \boldsymbol{x_d = y(5)},\ \dot{\boldsymbol{x}}_{\boldsymbol{d}} = \boldsymbol{x_{d_t} = y(6)},\ \ \boldsymbol{y_d = y(7)},\ \dot{\boldsymbol{y}}_{\boldsymbol{d}} = \boldsymbol{y_{d_t} = y(8)} \end{gathered} \tag{69}$$

Therefore, the state-space vector of the Jeffcott (4-DOF) rotor is:

$$\begin{aligned} \boldsymbol{x_R} &= [\boldsymbol{x_j}, \dot{\boldsymbol{x}}_{\boldsymbol{j}}, \boldsymbol{y_j}, \dot{\boldsymbol{y}}_{\boldsymbol{j}}, \boldsymbol{x_d}, \dot{\boldsymbol{x}}_{\boldsymbol{d}}, \boldsymbol{y_d}, \dot{\boldsymbol{y}}_{\boldsymbol{d}}]^{\boldsymbol{T}} \\ &= [\boldsymbol{y(1), y(2), y(3), y(4), y(5), y(6), y(7), y(8)}]^{\boldsymbol{T}} \end{aligned} \qquad \boldsymbol{x_R} \in \mathbb{R}^{8} \tag{70}$$

Eqs. (48)-(51) are now presented -with respect to state-space variables $y(n)$, where $n = 1, \dots, 8$- as first order ODEs. Specifically:

$$\dot{\boldsymbol{y}}(\boldsymbol{1}) = \boldsymbol{y(2)}, \qquad \dot{\boldsymbol{y}}(\boldsymbol{2}) = \frac{\boldsymbol{k_s(y(5) - y(1))}}{\boldsymbol{2m_j}} + \frac{\boldsymbol{F_{Bx}}}{\boldsymbol{m_j}} \tag{71}$$

$$\dot{\boldsymbol{y}}(\boldsymbol{3}) = \boldsymbol{y(4)}, \qquad \dot{\boldsymbol{y}}(\boldsymbol{4}) = \frac{\boldsymbol{k_s(y(7) - y(3))}}{\boldsymbol{2m_j}} + \frac{\boldsymbol{F_{By}}}{\boldsymbol{m_j}} - \boldsymbol{g} \tag{72}$$

$$\dot{\boldsymbol{y}}(\boldsymbol{5}) = \boldsymbol{y(6)}, \qquad \dot{\boldsymbol{y}}(\boldsymbol{6}) = -\frac{\boldsymbol{k_s(y(5) - y(1))}}{\boldsymbol{m_d}} + \frac{\boldsymbol{F_{Ux}}}{\boldsymbol{m_d}} \tag{73}$$

$$\dot{y}(7) = \boldsymbol{y(8)}, \qquad \dot{y}(8) = -\frac{\boldsymbol{k_s\big(y(7) - y(3)\big)}}{\boldsymbol{m_d}} + \frac{\boldsymbol{F_{Uy}}}{\boldsymbol{m_d}} - \boldsymbol{g} \tag{74}$$

The bearing forces $F_{Bx}.F_{By}$ are evaluated by applying numerical integration of the pressure distribution which is defined at all the respective grid points. The (71)-(74) group of ODEs can be written in matrix form as:

$$\dot{\boldsymbol{x}}_{\boldsymbol{R}} = \boldsymbol{f}(\boldsymbol{x_R}), \qquad \boldsymbol{f}: \mathbb{R}^{\boldsymbol{8}} \to \mathbb{R}^{\boldsymbol{8}} \tag{75}$$

Eventually, both for the bearing and the rotor model, an overall state-vector can be introduced:

$$\boldsymbol{x_{BR}} = [\boldsymbol{x_B^T}, \boldsymbol{x_R^T}]^{\boldsymbol{T}}, \qquad \boldsymbol{x_{BR}} \in \mathbb{R}^{\left(\frac{N_z}{2}+1\right)N_x+8} \tag{76}$$

and the overall model can be represented in matrix form as:

$$\dot{\boldsymbol{x}}_{\boldsymbol{BR}} = \boldsymbol{f}(\boldsymbol{x_{BR}}), \qquad \boldsymbol{f}: \mathbb{R}^{\left(\frac{N_z}{2}+1\right)N_x+8} \to \mathbb{R}^{\left(\frac{N_z}{2}+1\right)N_x+8} \tag{77}$$

To conclude, the nodes representing the fluid pressure $p_{i,j}$ and the foil deflection q_i can be introduced as a dimensionless state vector and the bearing model can be written as a nonlinear system of dimensionless, coupled first order ODEs, shown below:

$$\overline{\boldsymbol{x}}_{\boldsymbol{B}}' = \overline{\boldsymbol{f}}(\overline{\boldsymbol{x}}_{\boldsymbol{B}}), \qquad \overline{\boldsymbol{f}}: \mathbb{R}^{\left(\frac{N_z}{2}+1\right)N_x} \to \mathbb{R}^{\left(\frac{N_z}{2}+1\right)N_x} \tag{78}$$

where, $(N_x, N_z) = (29{,}10)$ and

$$\overline{\boldsymbol{x}}_{\boldsymbol{B}} = [\overline{\boldsymbol{p}}_{\boldsymbol{1,1}}, \dots, \overline{\boldsymbol{p}}_{N_x,\frac{N_z}{2}}, \overline{\boldsymbol{q}}_{\boldsymbol{1}}, \dots, \overline{\boldsymbol{q}}_{N_x}]^{\boldsymbol{T}}, \qquad \overline{\boldsymbol{x}}_{\boldsymbol{B}} \in \mathbb{R}^{\left(\frac{N_z}{2}+1\right)N_x} \tag{79}$$

Regarding the rotor model, the state vector for the eccentricity of the journal and the disc, in combination with their time derivatives (´) (with respect to dimensionless time), is given by

$$\begin{aligned}\overline{\boldsymbol{x}}_{\boldsymbol{R}} &= [\overline{\boldsymbol{x}}_{\boldsymbol{j}}, \overline{\boldsymbol{x}}_{\boldsymbol{j}}', \overline{\boldsymbol{y}}_{\boldsymbol{j}}, \overline{\boldsymbol{y}}_{\boldsymbol{j}}', \overline{\boldsymbol{x}}_{\boldsymbol{d}}, \overline{\boldsymbol{x}}_{\boldsymbol{d}}', \overline{\boldsymbol{y}}_{\boldsymbol{d}}, \overline{\boldsymbol{y}}_{\boldsymbol{d}}']^{\boldsymbol{T}} \\ &= [\overline{\boldsymbol{y}}(\boldsymbol{1}), \overline{\boldsymbol{y}}(\boldsymbol{2}), \overline{\boldsymbol{y}}(\boldsymbol{3}), \overline{\boldsymbol{y}}(\boldsymbol{4}), \overline{\boldsymbol{y}}(\boldsymbol{5}), \overline{\boldsymbol{y}}(\boldsymbol{6}), \overline{\boldsymbol{y}}(\boldsymbol{7}), \overline{\boldsymbol{y}}(\boldsymbol{8})]^{\boldsymbol{T}}\end{aligned} \qquad \overline{\boldsymbol{x}}_{\boldsymbol{R}} \in \mathbb{R}^{\boldsymbol{8}} \tag{80}$$

Eqs. (44)-(47) can now be written

$$\acute{\overline{\boldsymbol{y}}}(\boldsymbol{1}) = \overline{\boldsymbol{y}}(\boldsymbol{2}), \qquad \acute{\overline{\boldsymbol{y}}}(\boldsymbol{2}) = \frac{\boldsymbol{m_d}}{\boldsymbol{2m_j}} \overline{\boldsymbol{k}}_{\boldsymbol{s}}\big(\overline{\boldsymbol{y}}(\boldsymbol{5}) - \overline{\boldsymbol{y}}(\boldsymbol{1})\big) + \boldsymbol{\xi}\, \overline{\boldsymbol{F}}_{\boldsymbol{Bx}} \tag{81}$$

$$\acute{\overline{\boldsymbol{y}}}(\boldsymbol{3}) = \overline{\boldsymbol{y}}(\boldsymbol{4}), \qquad \acute{\overline{\boldsymbol{y}}}(\boldsymbol{4}) = \frac{\boldsymbol{m_d}}{\boldsymbol{2m_j}} \overline{\boldsymbol{k}}_{\boldsymbol{s}}(\overline{\boldsymbol{y}}(\boldsymbol{7}) - \overline{\boldsymbol{y}}(\boldsymbol{3})) + \boldsymbol{\xi}\, \overline{\boldsymbol{F}}_{\boldsymbol{By}} - \boldsymbol{\sigma} \tag{82}$$

$$\acute{\overline{\boldsymbol{y}}}(\boldsymbol{5}) = \overline{\boldsymbol{y}}(\boldsymbol{6}), \qquad \acute{\overline{\boldsymbol{y}}}(\boldsymbol{6}) = -\overline{\boldsymbol{k}}_{\boldsymbol{s}}(\overline{\boldsymbol{y}}(\boldsymbol{5}) - \overline{\boldsymbol{y}}(\boldsymbol{1})) + \overline{\boldsymbol{F}}_{\boldsymbol{Ux}} \tag{83}$$

$$\acute{\overline{\boldsymbol{y}}}(\boldsymbol{7}) = \overline{\boldsymbol{y}}(\boldsymbol{8}), \qquad \acute{\overline{\boldsymbol{y}}}(\boldsymbol{8}) = -\overline{\boldsymbol{k}}_{\boldsymbol{s}}\big(\overline{\boldsymbol{y}}(\boldsymbol{7}) - \overline{\boldsymbol{y}}(\boldsymbol{3})\big) + \overline{\boldsymbol{F}}_{\boldsymbol{Uy}} - \boldsymbol{\sigma} \tag{84}$$

The (81)-(84) group of ODEs can be written in matrix form as:

$$\overline{\boldsymbol{x}}_{\boldsymbol{R}}' = \overline{\boldsymbol{f}}(\overline{\boldsymbol{x}}_{\boldsymbol{R}}), \qquad \overline{\boldsymbol{f}}: \mathbb{R}^{\mathbf{8}} \to \mathbb{R}^{\mathbf{8}} \tag{85}$$

and the overall state-vector of the dimensionless problem, which combines both bearing's and rotor's state vectors, will be:

$$\overline{\boldsymbol{x}}_{\boldsymbol{BR}} = [\overline{\boldsymbol{x}}_{\boldsymbol{B}}^{\boldsymbol{T}}, \overline{\boldsymbol{x}}_{\boldsymbol{R}}^{\boldsymbol{T}}]^{\boldsymbol{T}}, \qquad \overline{\boldsymbol{x}}_{\boldsymbol{BR}} \,\boldsymbol{\epsilon}\, \mathbb{R}^{\left(\frac{\boldsymbol{N_z}}{\mathbf{2}}+\mathbf{1}\right)\boldsymbol{N_x}+\mathbf{8}} \tag{86}$$

The overall model represented by a set of coupled nonlinear first order ODEs is defined as:

$$\overline{\boldsymbol{x}}_{\boldsymbol{BR}}' = \overline{\boldsymbol{f}}(\overline{\boldsymbol{x}}_{\boldsymbol{BR}}), \qquad \overline{\boldsymbol{f}}: \mathbb{R}^{\left(\frac{\boldsymbol{N_z}}{\mathbf{2}}+\mathbf{1}\right)\boldsymbol{N_x}+\mathbf{8}} \to \mathbb{R}^{\left(\frac{\boldsymbol{N_z}}{\mathbf{2}}+\mathbf{1}\right)\boldsymbol{N_x}+\mathbf{8}} \tag{87}$$

The system in Eq. (87) can be very stiff, depending on the shaft properties and bump foil properties, and for that reason the MATLAB ode15s solver [67] is used for the evaluation of response through time integration. The time response presents interesting features due to the nonlinearity introduced by the gas forces. The specific system presents similar response for both low and high bump foil damping, respectively shown in Figs. 2.11 and 2.12. This is discussed in detail in the following Section where the quality of motion is analyzed. In Figs. 2.11 and 2.12 one may notice that different types of bifurcations occur as the parameter of rotating speed changes. Applying the specifications of Table 2.2 the time response of the system in Fig. 2.10 is evaluated and presented in Fig. 2.11 for foil loss factor $\eta = 0.003$, and in Fig. 2.12 for foil loss factor $\eta = 0.1$.

[67] Mark W. Reichelt and Lawrence F. Shampine, 8-30-94 Copyright 1984-2014 The MathWorks, Inc.

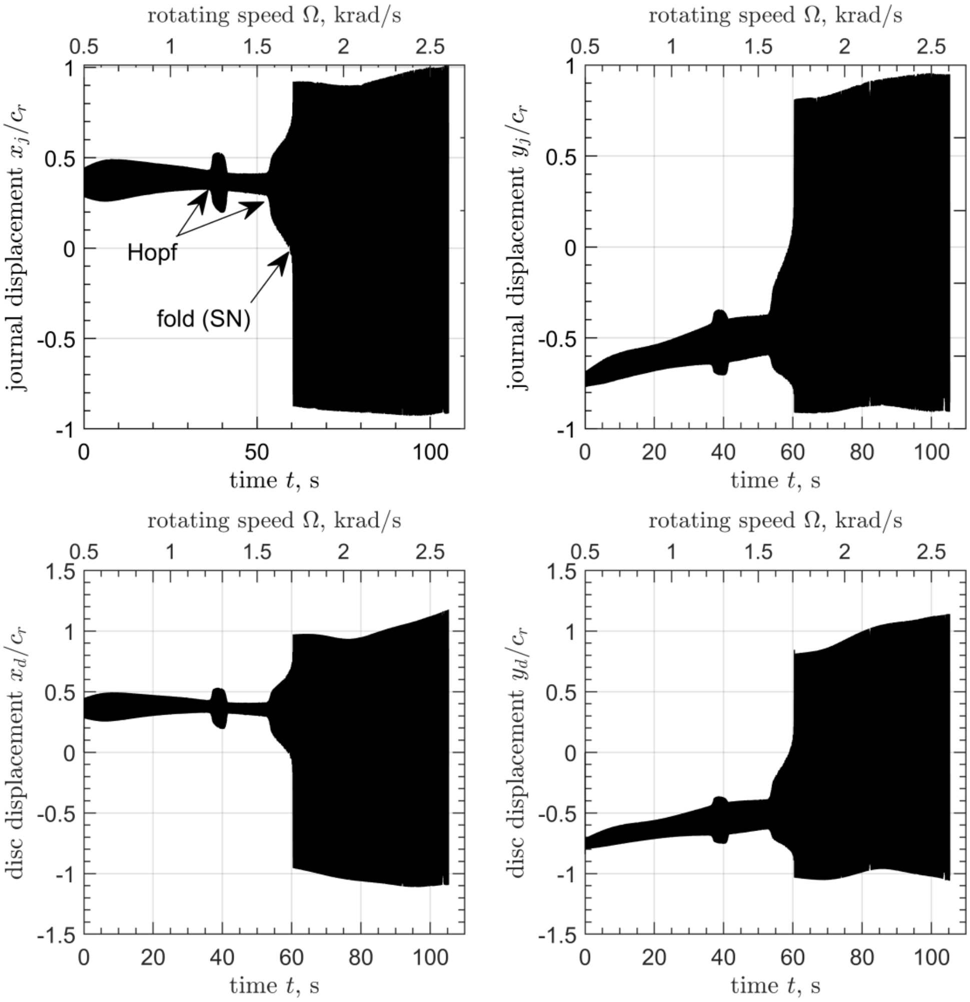

Fig. 2.11: Time response evaluated during the run-up of the unbalanced system with the specifications of Table 2.2 and foil loss factor $\eta = 0.003$. Respective bifurcation type is shown in the upper left chart; SN: Saddle Node (fold) bifurcation

Table 2.2: parameters used in the run-up simulation of the system of Figure 2.10. Bearing specifications are considered as in Table 2.1

Parameter	Value	Parameter	Value
Shaft dimensionless stiffness, $\bar{k}_s$	1	Disc mass m_d	3 kg
Dimensionless foil compliance, $\bar{a}_f$	0.01	Journal mass m_j	0.3 kg
Rotating acceleration a	20 rad/s^2	Unbalance $m_d \cdot$ e	7.5·10^{-6} kgm

Such quality of response is usual for high-speed rotors on gas foil bearings and the engineer should assess whether the integrity of the system is compromised regarding the type of instability appearing with the respective motion. A rotating system without the presence of bifurcation during run-up and run-down would render the optimum design. However, this is not always possible and many rotating systems have to operate reliably with the presence of bifurcations, e.g. turbosystems. A large variety of time response with respect of design properties is discussed in Chapter 3.

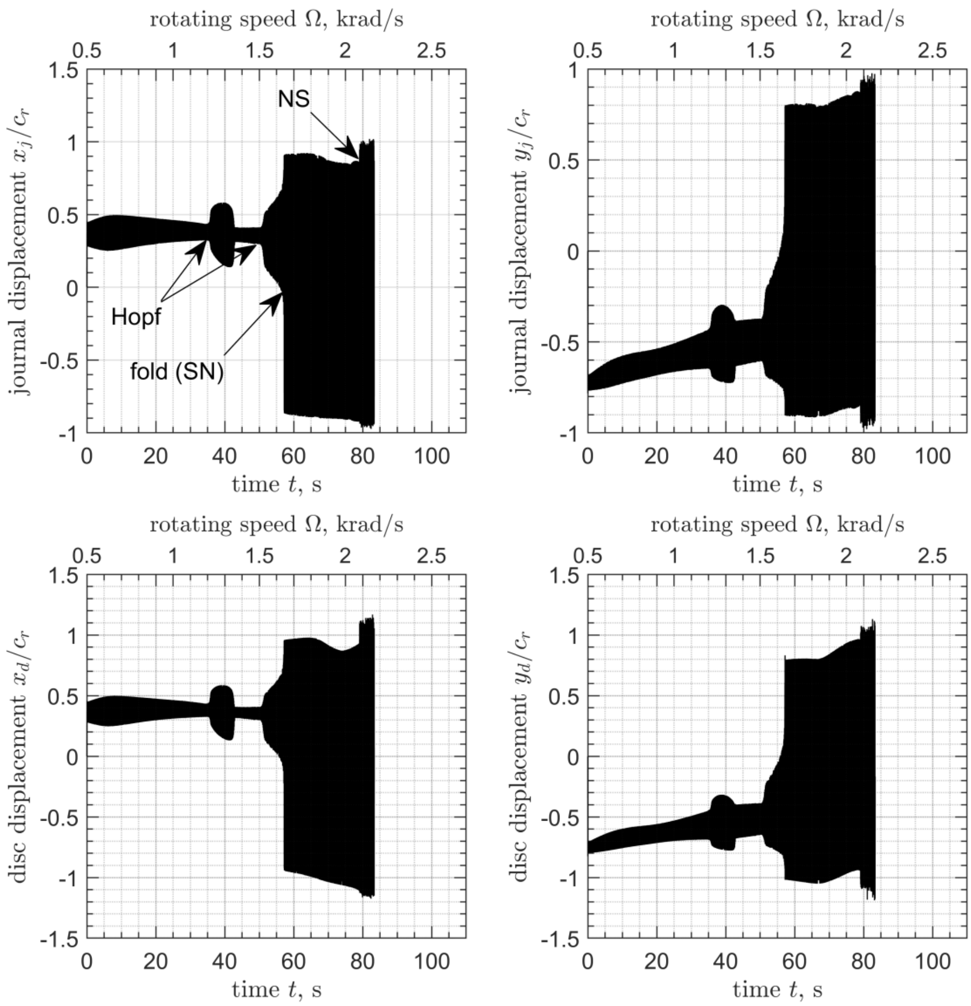

Fig. 2.12: Time response evaluated during the run-up of the unbalanced system with the specifications of Table 2.2 and foil loss factor $\eta = 0.1$. Respective bifurcation type is shown in the upper left chart; SN: Saddle Node (fold) bifurcation, NS: Neimark Sacker bifurcation

2.4 Quality of Motion and Stability

2.4.1 Study of the quality of motion

The stability of the autonomous system (system with a perfectly balanced rotor) is studied in this Section. Regarding the rotating speed (bifurcation parameter) and the design properties (foil properties and shaft properties), the system may develop four types of motions:

1) Asymptotically stable motion around a fixed-point equilibrium
2) Unstable motion around a fixed-point equilibrium
3) Orbital asymptotically stable motion around a limit cycle (stability envelop)
4) Unstable motion around a limit cycle (stability envelop)

In this work, the first two cases are studied in regards of stability. However, all cases are presented in time response evaluated in the next Chapter, and in this Section with indicative results.

In general, stable motion around fixed-point equilibrium is the desired status for a rotating system; this is not always achieved, or possible, though. Considering the time response depicted in Fig. 2.12 the following events are noticed in sequence of increasing speed regarding stability. The system defined in Table 2.2 with foil loss factor $\eta = 0.1$ (see Fig. 2.12 for time response) is examined in continue. Fig. 2.21 at the end of the Section may be also considered simultaneously with the figures mentioned in continue.

When the system rotates with low speed $\Omega < 1200\, rad/s$, the system experiences stable motions around equilibrium for any initial condition, see Fig. 2.13 (and Fig. 2.21). The trajectory of the autonomous system will asymptotically converge at a fixed point; see Fig. 2.13b, while the unbalanced system (non-autonomous) will develop stable orbits around the equilibrium (fixed point). The higher the unbalance is, the larger the orbital motion gets, see Fig. 2.13a. Furthermore, the system may experience a resonance due to the stiffness and mass properties of the shaft which place a critical speed in the specific speed domain.

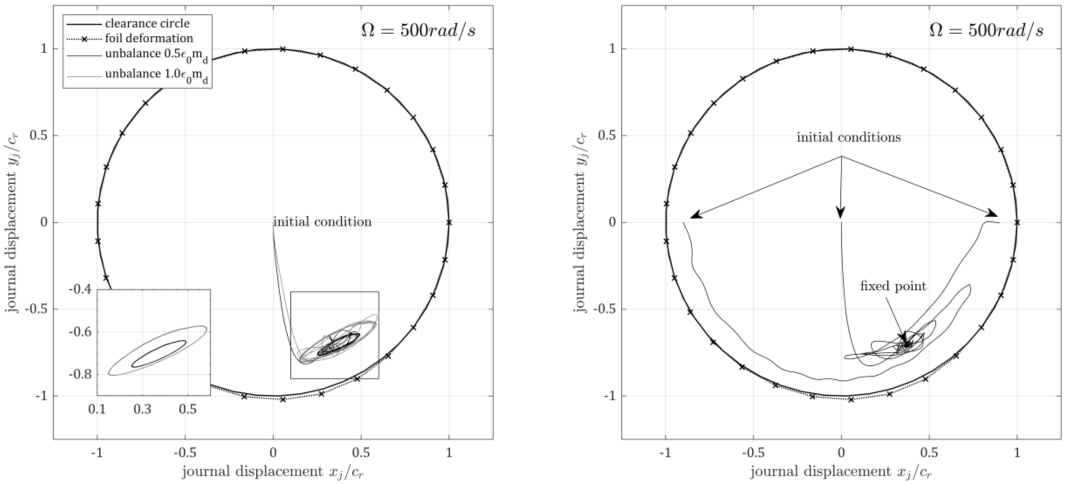

(a) (b)

Fig. 2.13: Trajectories of the journal for the system defined in Table 2.2 with foil loss factor $\eta = 0.1$ at $\Omega = 500\ rad/s$. a) non-autonomous system released from bearing center for two different unbalance magnitudes. b) autonomous system (perfectly balanced) released from different initial positions.

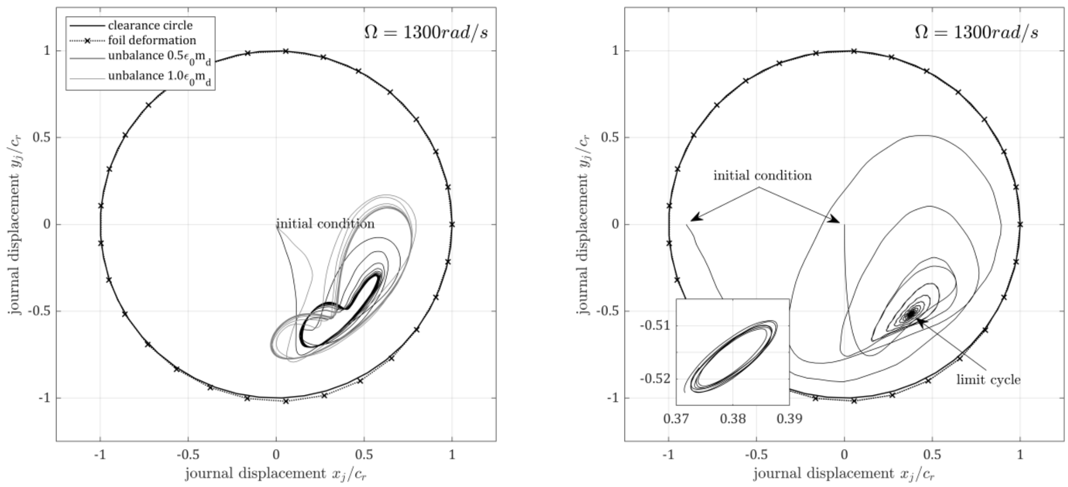

(a) (b)

Fig. 2.14: Trajectories of the journal for the system defined in Table 2.2 with foil loss factor $\eta = 0.1$ at $\Omega = 1300\ rad/s$. a) non-autonomous system released from bearing center for two different unbalance magnitudes. b) autonomous system (perfectly balanced) released from initial position.

As the system increases speed, and approximately after $\Omega = 1200\ rad/s$ (see Fig. 2.12 and Fig. 2.21), a Hopf-Andronov bifurcation occurs and stable limit cycles are generated, see Fig. 2.14b for $\Omega = 1300\ rad/s$. At this speed, a pair of complex eigenvalues of the Jacobian matrix of the system crosses the imaginary axis and the fixed-point equilibrium is not stable anymore. The limit cycles attract the trajectory of the system when released from different initial positions. However, as in the case of rotating speed $\Omega = 500\ rad/s$, a stable branch of solutions may appear close to the clearance circle. The motion of the unbalance system is periodic with period $2T_d$, where $T_d = 2\pi/1300$ is the driving period of the system (unbalance force period). This is a phase locked motion as verified from the Poincaré maps in continue. The autonomous system executes stable limit cycle motions when released from different initial conditions, see Fig. 2.14b. The period of the limit cycle motions is close to $2T_d$ (higher than), and can be evaluated using advanced tools for the study of periodic motions, like e.g. shooting method.

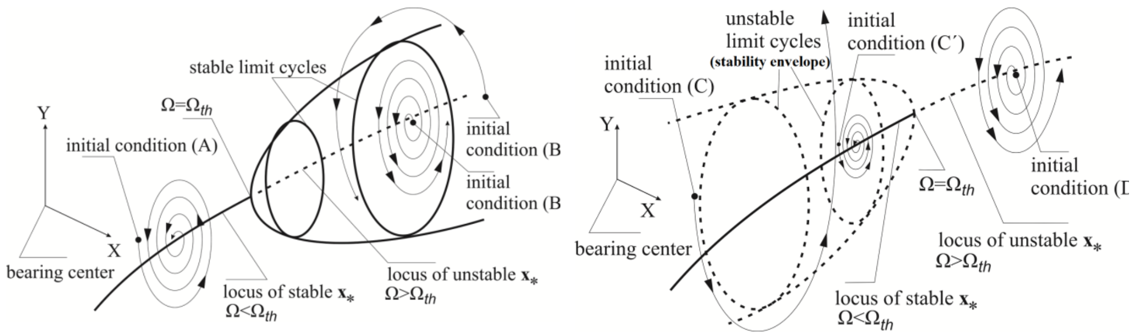

(a) (b)

Fig. 2.15: Representation of a) supercritical, and b) subcritical Hopf bifurcation

It should be mentioned that a Hopf bifurcation does not always generate stable limit cycles. The case of unstable limit cycles after a Hopf bifurcation is also likely in rotating systems; this is the case of subcritical Hopf bifurcations. Both cases may be realized with Fig. 2.15. At the case of subcritical Hopf bifurcation, the system motion is limited only by physical constraints (rotor stator contact) and its operation cannot be sustained at most cases. However, this is not the case here, but it will be included in Chapter 3. In Fig. 2.15 one can see the definition of Ω_{th} where the Hopf bifurcation occurs. This is the threshold speed of instability and in this work it will refer to the rotating speed where the first Hopf bifurcation occurs.

Increasing speed further, at approximately $\Omega = 1350\ rad/s$, see Fig. 2.12 (and Fig. 2.21), another Hopf bifurcation occurs and the system obtains again stable fixed points. This is not the most common scenario in rotating systems though. Usually, the Hopf bifurcation is followed by a saddle node bifurcation as described in continue.

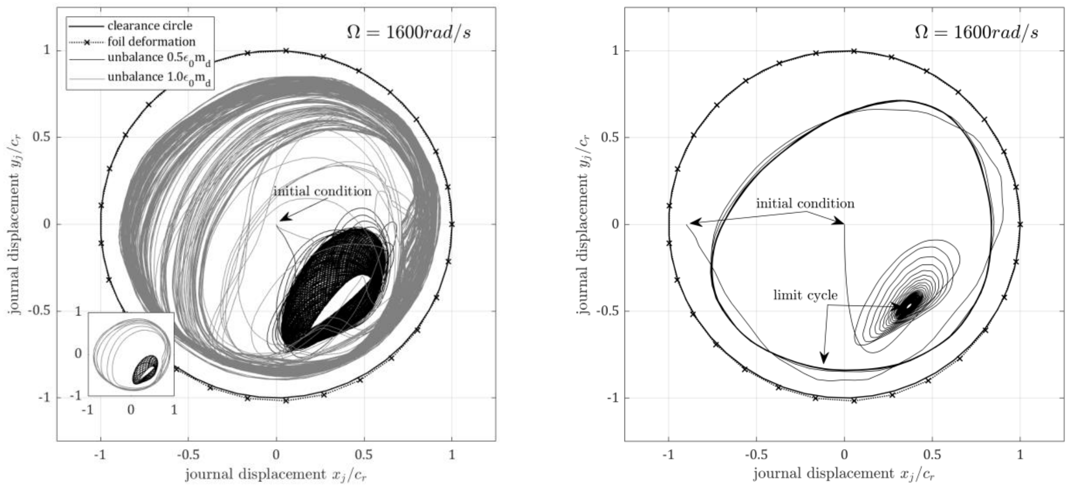

(a) (b)

Fig. 2.16: Trajectories of the journal for the system defined in Table 2.2 with foil loss factor $\eta = 0.1$ at $\Omega = 1600\ rad/s$. (a) non-autonomous system released from bearing center for two different unbalance magnitudes. (b) autonomous system (perfectly balanced) released from different initial positions.

Increasing the rotating speed further, at approximately $\Omega = 1500\ rad/s$, another Hopf bifurcation occurs, and like before, stable limit cycles are generated; this is a case of supercritical Hopf bifurcation. At this case it is clear that the system motion may attracted either by the stable limit cycle when the initial condition is close to it, e.g. at the bearing center, see Fig. 2.16b (when the speed is slightly higher $\Omega = 1600\ rad/s$), or by another branch of solutions existing close to clearance circle, when the initial condition is close to it, see Fig. 2.16b (and Fig. 2.21). The unbalance magnitude will render the respective motion in the non-autonomous system, see Fig. 2.16a, for the same initial conditions. Quasi-periodic motions are developed in the non-autonomous system for both cases of unbalance; this will be shown in continue with the use of Poincaré maps.

Increasing rotating speed at approximately $\Omega = 1650\ rad/s$ a saddle node bifurcation occurs and the system will develop only one type of trajectory, regardless the initial position of the balanced system, see Fig. 2.17b, or the unbalance magnitude, see Fig. 2.17a, for the speed of $\Omega = 1800\ rad/s$ (see also Fig. 2.21). The quasi-periodic motion at this case is close to the clearance circle, see Fig. 2.17, and the system is supposed to suffer from unstable whirling. This is the quality of motion for every rotating speed lower than $\Omega = 2100\ rad/s$, see Fig. 2.12.

At approximately $\Omega = 2100\ rad/s$ another type of bifurcation, the Neimark-Sacker (NS) bifurcation occurs. This bifurcation generates limit cycles which are bounded (attracted) from a torus-like shape of solution branches. Neimark-Sacker bifurcation can be supercritical or subcritical. Like in Hopf bifurcation, stable limit cycles will be generated after a supercritical Neimark-Sacker bifurcation, while unstable limit cycles will be generated after a subcritical Neimark-Sacker bifurcation. The motion is depicted in Fig. 2.18 for $\Omega = 2200\ rad/s$.

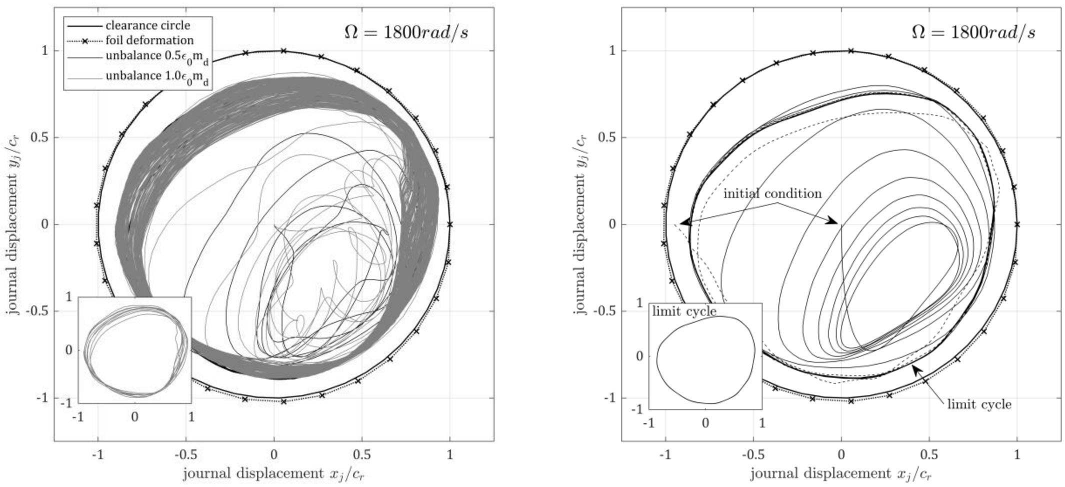

(a) (b)

Fig. 2.17: Trajectories of the journal for the system defined in Table 2.2 with foil loss factor $\eta = 0.1$ at $\Omega = 1800\ rad/s$. (a) non-autonomous system released from bearing center for two different unbalance magnitudes. (b) autonomous system (perfectly balanced) released from different initial positions.

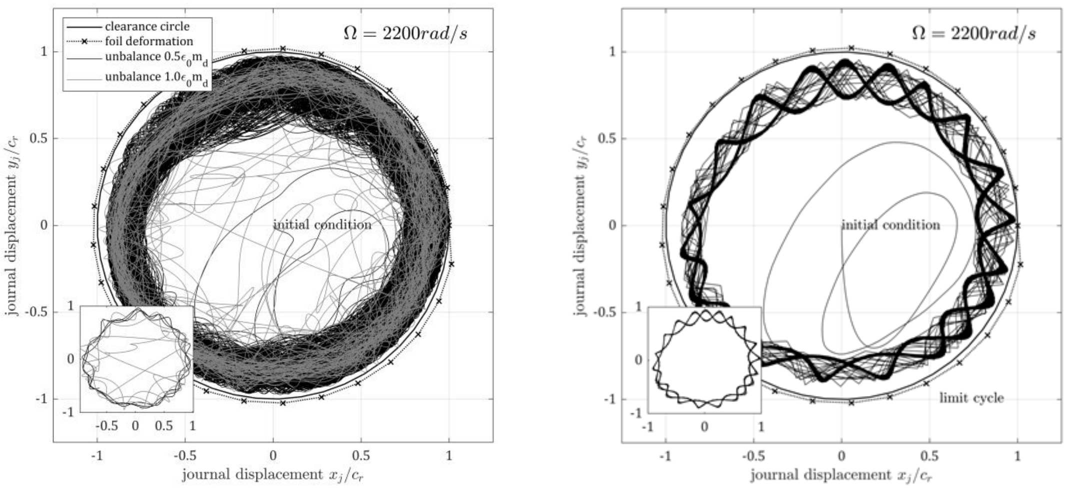

(a) (b)

Fig. 2.18: Trajectories of the journal for the system defined in Table 2.2 with foil loss factor $\eta = 0.1$ at $\Omega = 2200\ rad/s$. (a) non-autonomous system released from bearing center for two different unbalance magnitudes. (b) autonomous system (perfectly balanced) released from different initial positions.

After a Neimark-Sacker bifurcation, the system can hardly retain operation and integrity, and operation should be tripped. The motion can be described as whip (referring to respective oil-whip instability in oil film bearings) and the most likely scenario is that rotor-stator contact will be taking place as the journal rotates. The motion may become chaotic as is shown in continue.

The respective Poincaré maps of the trajectories depicted in Figs. 2.13a-2.14a and Figs. 2.16a-2.18a are evaluated and presented in Fig. 2.19 when physical coordinates are used, and in Fig. 2.20 when state space coordinates are applied. At $\Omega = 500\,rad/s$ periodic motions of period $1T_d$ are detected and Poincaré maps consist of one point, see Figs. 2.19a and 2.20a. At $\Omega = 1300\,rad/s$ periodic motions of period $2T_d$ are detected and Poincaré maps consist of two points, see Figs. 2.19b and 2.20b. These are examples of so-called phase-locked motions.

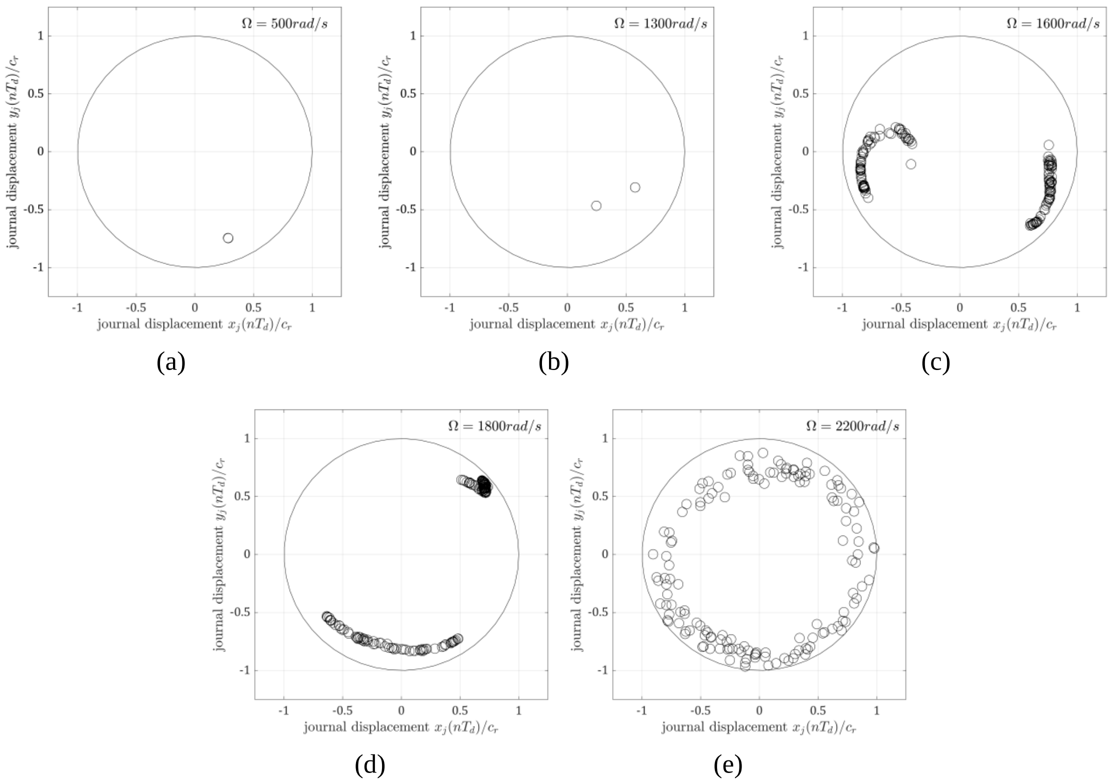

Fig. 2.19: Poincaré map of physical coordinates of the journal orbits evaluated in Figs. 13-17. (a) $\Omega = 500\,rad/s$, (b) $\Omega = 1300\,rad/s$, (c) $\Omega = 1600\,rad/s$, (d) $\Omega = 1800\,rad/s$, (e) $\Omega = 2200\,rad/s$

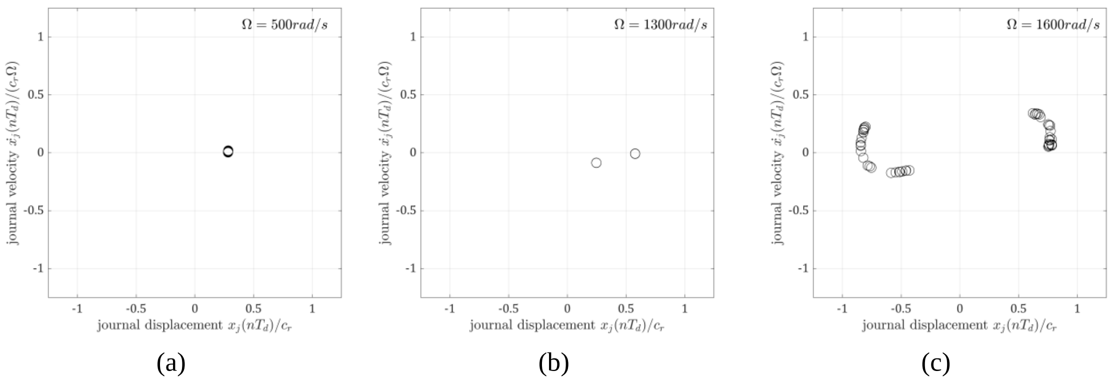

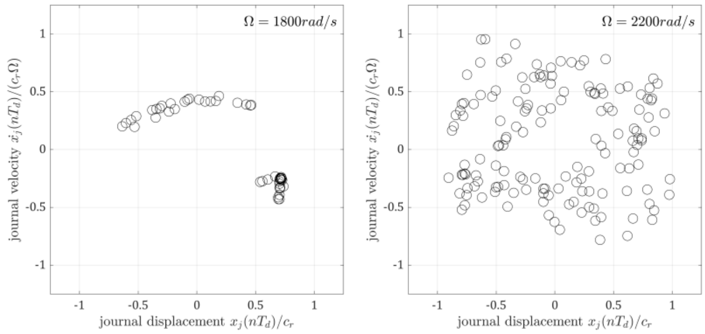

Fig. 2.20: Poincaré map of state space coordinates of the journal orbits evaluated in Figs. 13-17. (a) $\Omega = 500\ rad/s$, (b) $\Omega = 1300\ rad/s$, (c) $\Omega = 1600\ rad/s$, (d) $\Omega = 1800\ rad/s$, (e) $\Omega = 2200\ rad/s$

At $\Omega = 1600\ rad/s$ quasi-periodic motions are detected and Poincaré maps consist of points (not clearly discretized) in a geometrically defined shape, see Figs. 2.19c and 2.20c. The same quality of quasi-periodic motion is detected also for the motion at $\Omega = 1800\ rad/s$, see Figs. 2.19d and 2.20d. Chaotic motion is identified at $\Omega = 2200\ rad/s$ where Poincaré maps consist of arbitrarily located points in non-geometrically defined shape, see Figs. 2.19e and 2.20e. This is better realized in Fig. 2.20e where the characteristic cloud appears. However, chaotic motion may be interpreted also in a Poincaré map with geometrically defined shape.

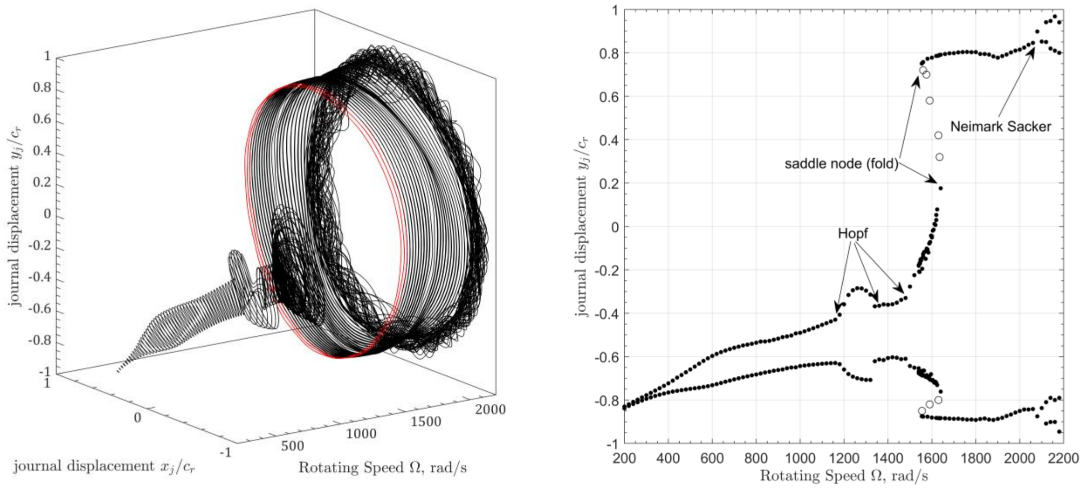

Fig. 2.21: (a) Limit cycles evaluated for the non-autonomous (unbalanced) system; (b) max-min values in vertical plane and respective type of bifurcation

2.4.2 Stability assessment of fixed-point equilibrium

The system of Eq. (77), is studied on the stability of its fixed-point equilibrium. The size of the system is $n \times n$, where $n = (N_z/2+1)N_x + 8$, and the bifurcation parameter is Ω. Therefore, the system is repeated for convenience as in Eq. (88).

$$\dot{\boldsymbol{x}}_{\boldsymbol{n}\times\mathbf{1}} = \boldsymbol{f}_{\boldsymbol{n}\times\mathbf{1}}(\boldsymbol{x}_{\boldsymbol{n}\times\mathbf{1}}, \boldsymbol{\Omega}) \quad \textbf{(88)}$$

At first, the equilibrium points of the system $\mathbf{x}_*(\Omega)$ (critical points, or fixed points) have to be evaluated for the different values of Ω, using a numerical method, e.g. Newton-Raphson. For each fixed point, the Jacobian matrix $\mathbf{J}$ is defined in Eq. (89). The eigenvalues have to be evaluated simultaneously and then to be ordered as $Re(\lambda_{1,2}) > Re(\lambda_{3,4}) > Re(\lambda_{5,6}) > \ldots > Re(\lambda_{n-1,n})$.

The interest is to find the Ω_{th} for which the eigenvalues of $\mathbf{J}(\Omega_{th})$ contain a pair $\lambda_{1,2} = \mathrm{a}(\Omega_{th}) \pm \mathrm{i}\cdot\mathrm{b}(\Omega_{th})$ where $Re(\lambda_{1,2}) = \mathrm{a}(\Omega_{th}) = 0$.

$$\mathbf{J}(\Omega_{th}) = \left.\begin{bmatrix} \frac{\partial f_1}{\partial x_1} & \frac{\partial f_1}{\partial x_2} & \cdots & \frac{\partial f_1}{\partial x_n} \\ \frac{\partial f_2}{\partial x_1} & \frac{\partial f_2}{\partial x_2} & \cdots & \frac{\partial f_2}{\partial x_n} \\ \vdots & \vdots & \ddots & \vdots \\ \frac{\partial f_n}{\partial x_1} & \frac{\partial f_n}{\partial x_2} & \cdots & \frac{\partial f_n}{\partial x_n} \end{bmatrix}\right|_{\Omega=\Omega_{th}} \quad \textbf{(89)}$$

The reader has to check whether $Re(\lambda_1'(\Omega_{th})) = Re\left(\left.\frac{\partial \lambda_1}{\partial \Omega}\right|_{\Omega=\Omega_{th}}\right) = \mathrm{a}'(\Omega_{th})$ and $\mathrm{b}(\Omega_{th})$ are non-zero quantities, and $Re(\lambda_k) < 0$ for $k = 3,4,\ldots n$. If the above are satisfied, then the system undergoes a Hopf-Andronov (or simply Hopf) bifurcation as Ω crosses Ω_{th}.

Several systems have been assessed at their fixed-point equilibrium, as described above, for several design properties of shaft stiffness $\bar{k}_s$, bump foil stiffness $\bar{a}_f$, and bump foil loss factor η. More specifically, three cases of shaft stiffness are examined: $\bar{k}_s = 0.1$ for slender rotor with high elasticity (corresponding to slenderness ratio $L/D > 10$), $\bar{k}_s = 1$for intermediate shaft elasticity (corresponding to slenderness ratio $1 < L/D < 10$), and $\bar{k}_s = 10$ for low shaft elasticity (corresponding to a rigid rotor). Several values for $\bar{a}_f$ at the range $0.01 < \bar{a}_f < 1$ ($\bar{a}_f = 0.01$ corresponds to rigid foil), and for loss factor η at the range $10^{-4} < \eta < 1$ are selected at the case study. The corresponding results are depicted in Fig. 2.21 where it is depicted that for specific properties of bump foil properties, the extension of threshold speed of instability to higher values is feasible. The extension may reach the value of 10 times in the system with $\bar{k}_s = 1$, or less for other cases of shaft stiffness; consider that for the case of $\bar{k}_s = 0.1$ some numerical issues were noticed and the graph Fig. 2.21a does not appear correctly. It is valuable to note that the extension of instability threshold speed appears for similar values of bump foil stiffness and loss factor at all three shafts checked.

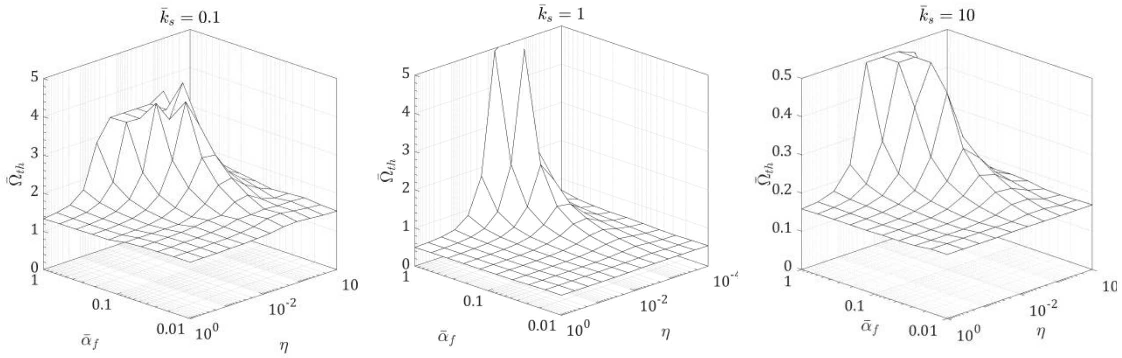

(a) (b) (c)

Fig. 2.22: Instability threshold speed $\overline{\Omega}_{th}$ as a function of bump foil compliance $\bar{a}_f$ and loss factor η for different shaft stiffness a) $\bar{k}_s = 0.1$, b) $\bar{k}_s = 1$, and c) $\bar{k}_s = 10$

This page has been intentionally left blank

3 RESULTS FOR UNBALANCE RESPONSE

In this chapter, several simulations are performed in order to observe the influence of the bump foil design parameters in regards to the stability of the non-autonomous (unbalanced) system. As key parameters for these studies are considered the rotating speed Ω and two of the selected design variables; the dimensionless foil compliance $\overline{\alpha}_f = 1/\overline{k}_f$ and the foil structure loss factor η. The results are obtained in two operating conditions of the Jeffcott rotor system, as mentioned before; first, for a linearly varying $\Omega = at$ -where $a = 20\, rad/s$- and second, for a stepped varying rotating speed for a specific time domain per step (500 driving periods per each value of rotating speed). In both cases, the initial rotating speed is assumed at $\Omega = 500\, rad/s$ while the maximum speed is supposed to exceed $\Omega = 2000\, rad/s$ depending on the two design parameters $\overline{\alpha}_f$, and η, and the respective quality of motion that the solver is able to approach. Different values of unbalance magnitude are applied in several cases.

Table 3.1: Changing parameters for the simulations executed in chapter 3.

Shaft dimensionless stiffness, $\overline{k}_s$	Foil dimensionless compliance, $\overline{\alpha}_f$	Foil loss factor, η	Unbalance eccentricity, e
A: $\overline{k}_s = 0.1$	1: $\overline{\alpha}_f = 0.01$	a: $\eta = 0.003$	1: $e = 2.5 \cdot 10^{-8}$ m
B: $\overline{k}_s = 1$	2: $\overline{\alpha}_f = 0.1$	b: $\eta = 0.01$	2: $e = 2.5 \cdot 10^{-6}$ m
C: $\overline{k}_s = 10$	3: $\overline{\alpha}_f = 1$	c: $\eta = 0.1$	

In terms of indication, for two different values of unbalance eccentricity $e = 0.5 \times 10^{-2} \times e_{iso}$ and $e = 0.5 \times e_{iso}$ -where $e_{iso} = 5 \times 10^{-6}\, m$- and $\overline{k}_s = 1, \overline{\alpha}_f = 0.01, \eta = 0.01$, the transient response together with its time-frequency decomposition diagram is evaluated during the run-up of each unbalanced system. Simultaneously, the response together with the respective bifurcation diagrams is obtained via the stepped run-up simulations. Again, it is important to note that the existence of a steady state response is a necessary condition in order to produce those bifurcation diagrams, hence the last 100 driving periods per speed step are taken into account. Furthermore, an additional plot per case will be introduced, containing orbit, Poincaré and FFT diagrams for different values of rotating speed Ω in order to examine thoroughly the motions that each case renders. The aforementioned evaluations are depicted in Figs. 3.1-3.4.

As rotating speed increases for the first of the two cases, see Fig. 3.1, where $e = 0.5 \times e_{iso}$, and approximately at $\Omega = 1250$ rad/s, a Hopf-Andronov bifurcation takes place, while by increasing the system's speed further, around $\Omega = 1350$ rad/s, another Hopf bifurcation occurs and the system returns to stable fixed points. One may notice that the system's behavior is almost identical with the one examined in section 2.4, with the sole difference between these two systems being the arithmetic value of the foil loss factor η, currently $\eta = 0.01$ and previously $\eta = 0.1$. Increasing the rotating speed further, at approximately $\Omega = 1550$ rad/s, a Hopf bifurcation occurs once again and stable limit cycles are induced. At $\Omega = 1700$ rad/s, a saddle node bifurcation occurs, resulting to the development of one type of trajectory for every speed value until approximately $\Omega = 2150$ rad/s, as will be shown in continue in Fig. 3.2. Eventually, by the time the rotating speed exceeds $\Omega = 2150\,\mathrm{rad/s}$, the system experiences a Neimark-Sacker bifurcation where whip motion is observed, most likely leading to journal-bearing contact. It is expected that the system will not retain its operation after a Neimark-Sacker bifurcation due to the violent motions of the journal.

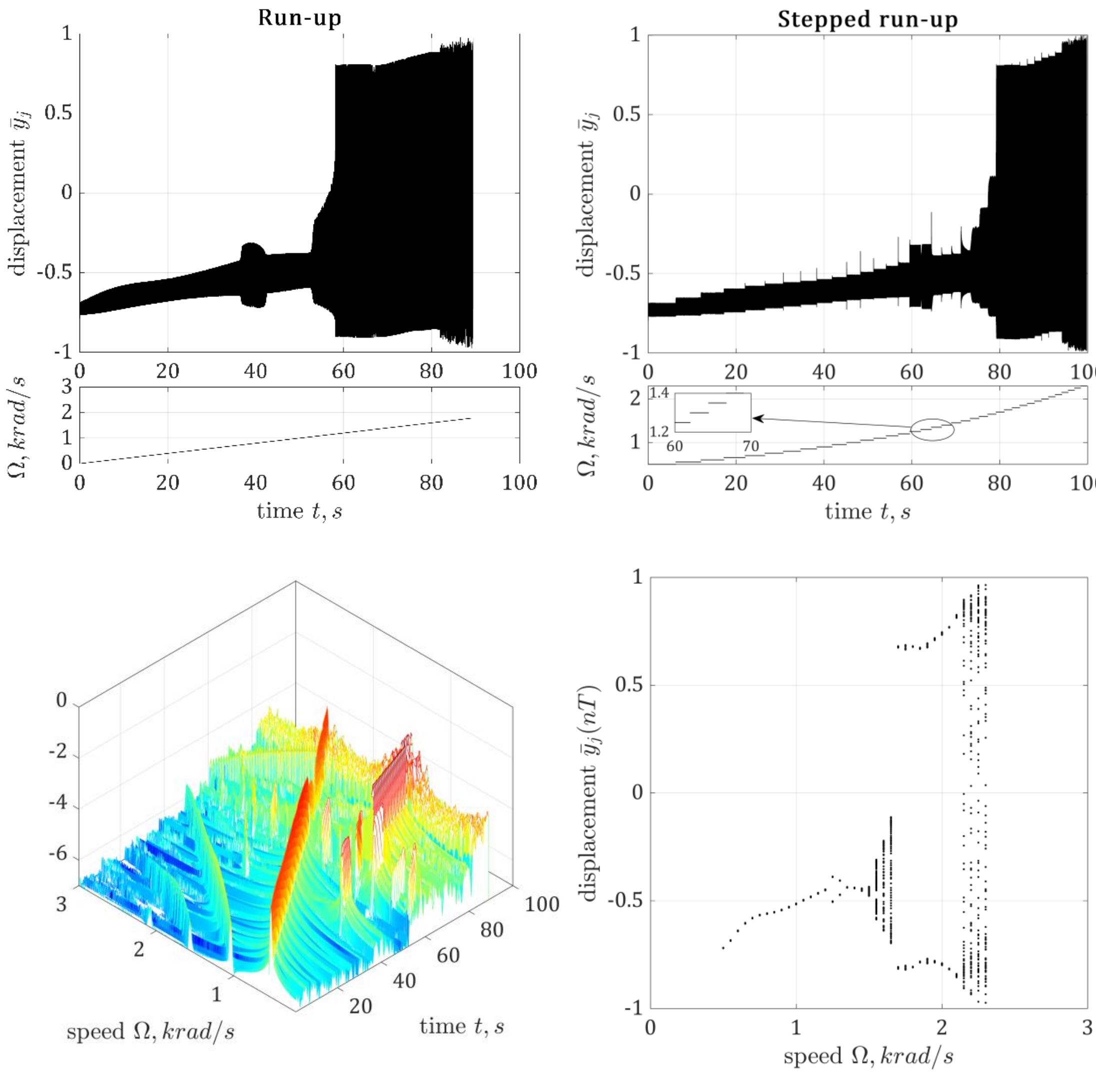

Fig. 3.1: (left) Transient response and time-frequency decomposition of the journal's vertical displacement $\overline{y}_j$. (right) Response of the vertical displacement $\overline{y}_j$ after a stepped run-up execution and bifurcation diagram. Parameters: $e = 0.5\ \times e_{iso} = 2.5 \times 10^{-6}\ m, \overline{K}_s = 1, \overline{\alpha}_f = 0.01, \eta = 0.01$ (case B1b2)

Fig. 3.2 shows the orbit, Poincaré and FFT diagrams of the vertical displacement of the journal at various rotating speeds, for the first case of the unbalance eccentricity $e = 0.5\ \times e_{iso}$. At speed $\Omega = 1000\,\mathrm{rad/s}$, the response of the journal is of period $1T_d$, confirmed by the respective Poincaré map, see Fig. 3.2a, which shows a single point. A super-synchronous vibration is detected from the FFT plot, which shows two distinct peaks; one at the synchronous speed and another at a super-synchronous frequency. These super-synchronous vibrations can be also detected in the STFT diagram, shown in Fig. 3.1. According to that, super-synchronous vibrations are expected throughout the whole duration of the executed simulation, while sub-synchronous vibrations should be expected too after a certain point in time. At speed $\Omega = 1250\,\mathrm{rad/s}$, the Hopf bifurcation mentioned in the previous paragraph occurs and the motion becomes period $2T_d$. The Poincaré map shows two distinct points, while the FFT plot shows four distinct peaks; one at the synchronous speed, two at super-synchronous frequencies, and for first time one major component at a sub-synchronous frequency.

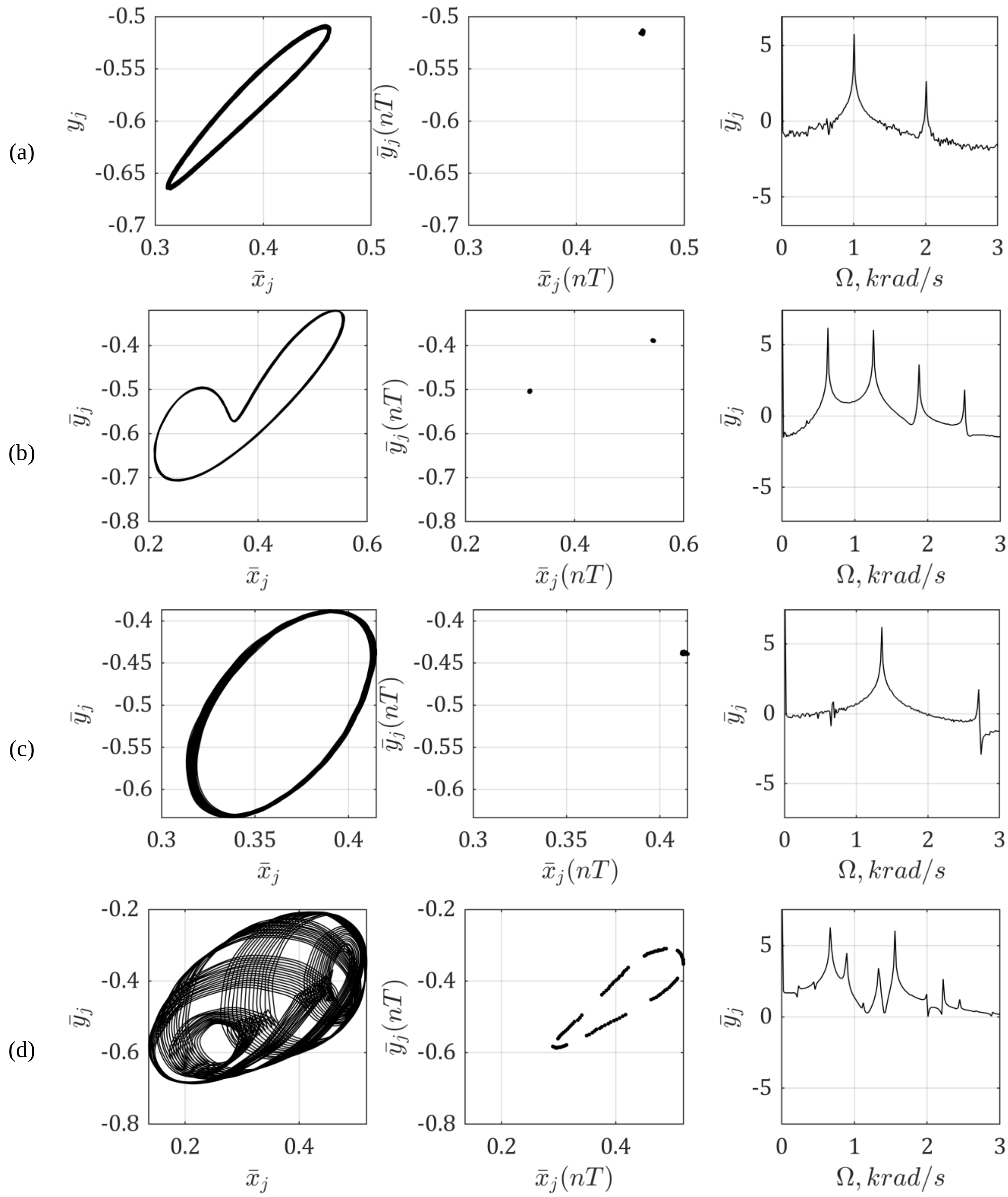

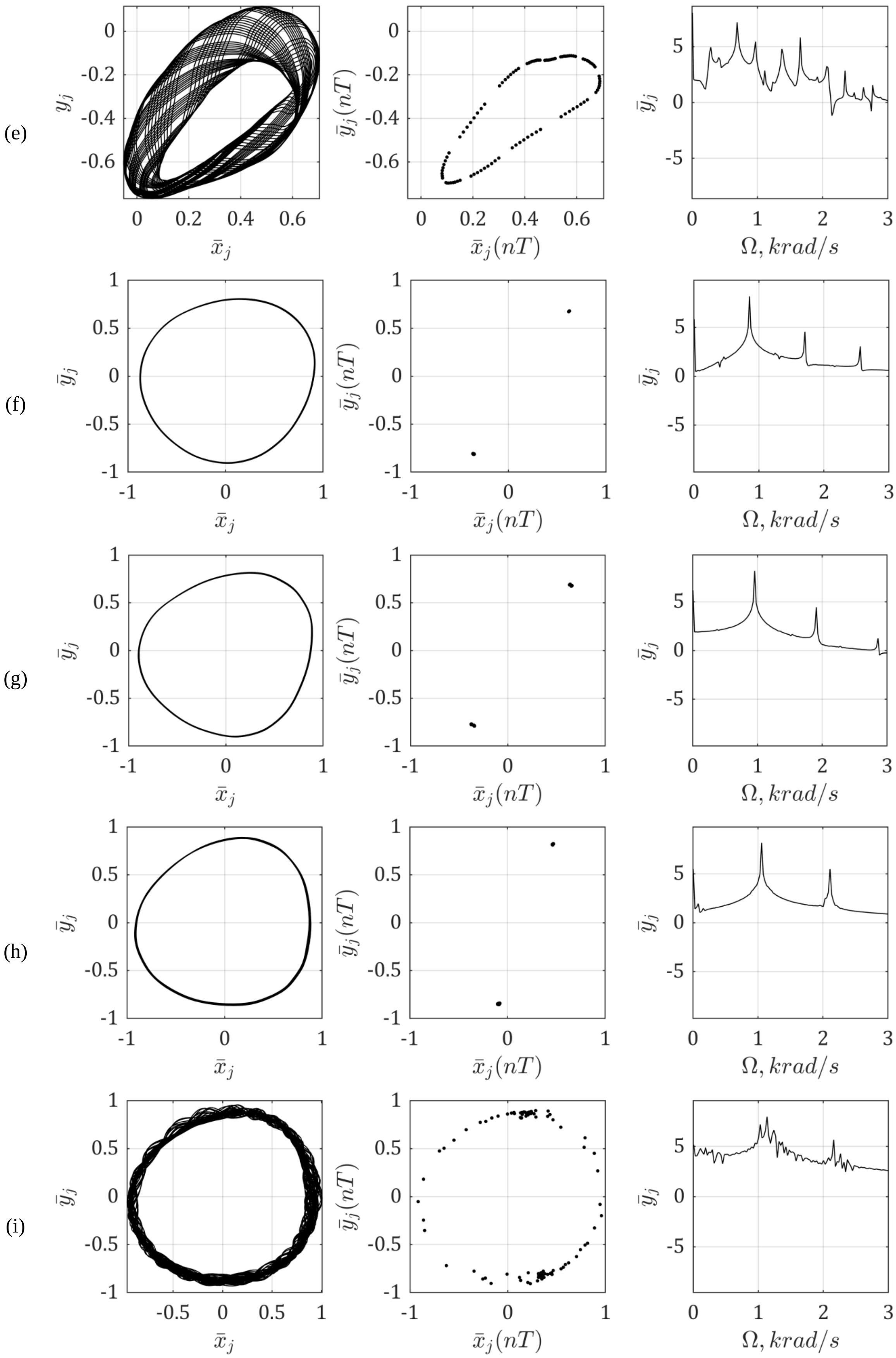
(e)
(f)
(g)
(h)
(i)
$\bar{x}_j$
$\bar{y}_j$
$\bar{x}_j(nT)$
$\bar{y}_j(nT)$
$\Omega, krad/s$

Fig. 3.2: Orbit, Poincaré and FFT diagrams for different speed Ω at unbalance $e = 0.5 \times e_{iso} = 2.5 \times 10^{-6}\ m$: (a) $\Omega = 1000\ rad/s$, (b) $\Omega = 1250\ rad/s$, (c) $\Omega = 1350\ rad/s$, (d) $\Omega = 1550\ rad/s$, (e) $\Omega = 1650\ rad/s$, (f) $\Omega = 1700\ rad/s$, (g) $\Omega = 1900\ rad/s$, (h) $\Omega = 2100\ rad/s$, (i) $\Omega = 2150\ rad/s$

At a slightly higher speed $\Omega = 1350$ rad/s, the motion returns to the period $1T_d$ state (after a 2nd Hopf bifurcation has taken place), and a larger orbital motion is detected in comparison to the previous one at $\Omega = 1000$ rad/s. At the next examined speed $\Omega = 1550$ rad/s, the motion converts to quasi-periodic; a conclusion then can be drawn via the Poincaré map depicted in Fig. 3.2d where the points form a geometrically defined shape but the points cannot be distinguished, affirming the quasi-periodic nature of the motion. The FFT plot shows a multitude of sub-synchronous and super-synchronous vibrations that arise at this rotating speed.

The same quality of a quasi-periodic motion takes place at speed $\Omega = 1650$ rad/s, see Fig. 3.2e. With a slight increase in rotating speed, specifically at $\Omega = 1700$ rad/s, the system experiences a saddle node bifurcation and a period $2T_d$ motion is observed, with the orbit extending up to the clearance circle. The same quality of motion applies until approximately $\Omega = 2150$ rad/s. By the time speed exceeds this value, the motion converts to quasi-periodic and, if further increase of speed takes place, it becomes chaotic.

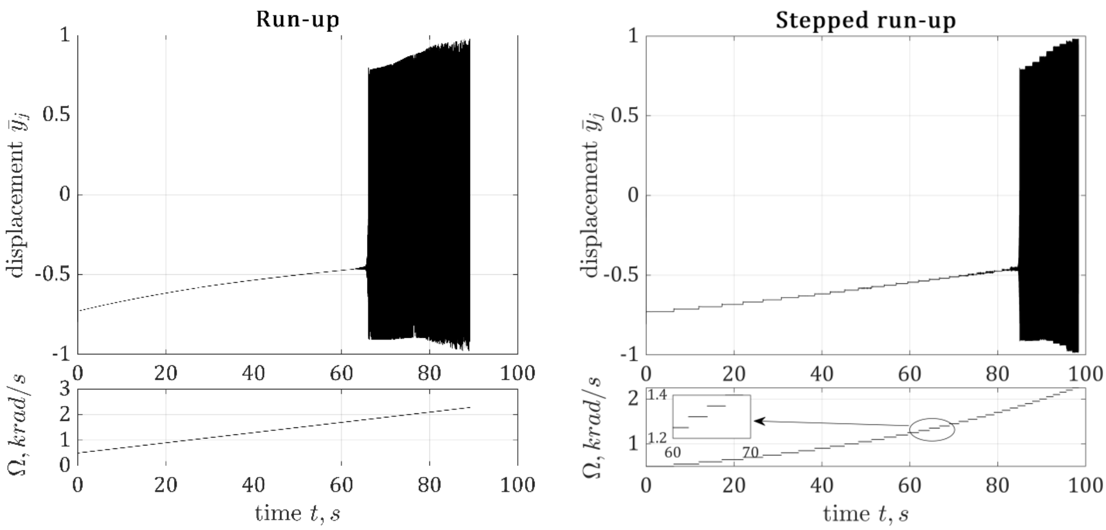

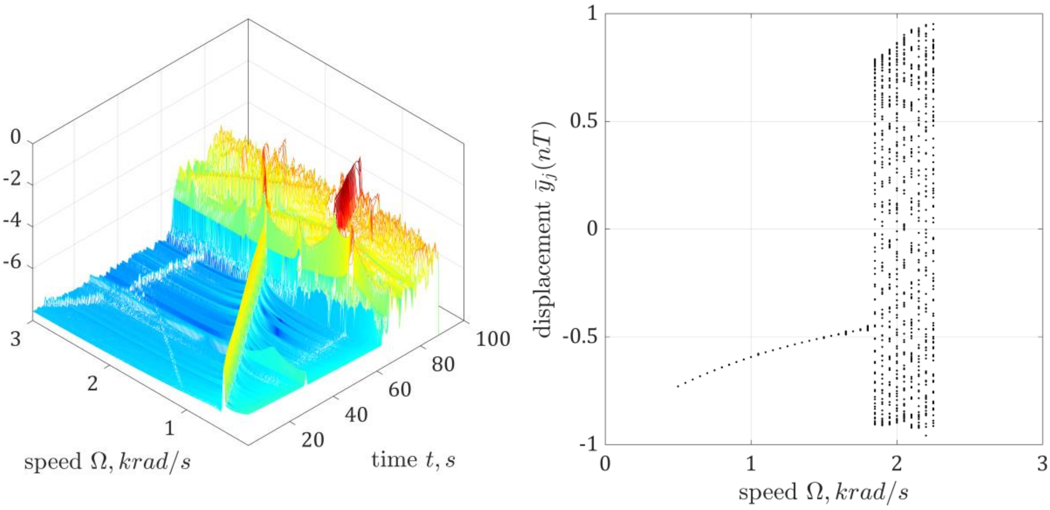

Fig. 3.3: (left) Transient response and time-frequency decomposition of the journal's vertical displacement $\overline{y}_j$; (right) Response of the vertical displacement $\overline{y}_j$ after a stepped run-up execution and bifurcation diagram; Parameters: $e = 0.5\ \times 10^{-2} \times e_{iso} = 2.5 \times 10^{-8}\ m, \overline{K}_s = 1, \overline{\alpha}_f = 0.01, \eta = 0.01$ (case B1b1)

The vertical response of the journal with the corresponding STFT and bifurcation diagrams, for a lower unbalance eccentricity $e = 0.5\ \times 10^{-2} \times e_{iso} = 2.5 \times 10^{-8}$ is depicted in Fig. 3.3. Both a run-up and a stepped run-up were executed in order to obtain them, following the same process as in the previous case. One may claim that there is no pluralism detected in this case's motions in comparison to the first one, where the unbalance eccentricity is a hundred times greater than the current. When the system rotates with speed lower than $\Omega = 1850\,\mathrm{rad/s}$, stable motions around specific equilibrium point/points are observed, with few exceptions breaking this norm, as will be shown subsequently, where quasi-periodic motions are developed. At $\Omega = 1850\,\mathrm{rad/s}$, a supercritical Hopf-Andronov bifurcation occurs, with stable limit cycles being generated right after, inducing multi-periodic and quasi-periodic motions that will be shown and explained subsequently.

The respective orbits, Poincaré maps and FFTs for the second case are depicted below, in Fig. 3.4. At rotating speed $\Omega = 1000\ rad/s$, the response of the journal's center is multi-periodic. More accurately, a period $3T_d$ motion is observed from the Poincaré map, which shows three distinct points. The FFT plot shows that, except for the synchronous, both subsynchronous and supersynchronous frequency vibrations arise. At speed $\Omega = 1200\ rad/s$, the journal's center vibration is synchronous with period $1T_d$, as a single point and single peak suggest in Poincaré and FFT maps respectively, see Fig. 3.4b. As the system increases speed, at approximately $\Omega = 1500\ rad/s$, a quasi-periodic motion is unveiled, while a synchronous and of a higher amplitude subsynchronous vibrations are noticed from the respective FFT diagram. Right after, the system obtains again stable fixed points, until the speed of the system reaches $\Omega = 1700\ rad/s$, where the periodic quality of motion gradually transforms to quasi-periodic once again. This can be ascertained at a slightly higher speed $\Omega = 1800\ rad/s$, where the quasi-periodic nature of the motion is obvious. Approximately after $\Delta t = 2.5\ s$ the rotating speed becomes $\Omega = 1850\ rad/s$.

The Hopf-Andronov bifurcation occurs and the motion becomes multi-periodic as long as the rotating speed remains lower than $\Omega = 2150\ rad/s$. Two peaks are visible in the FFT plots, meaning that the synchronous and another subsynchronous vibration are dominating at this range of speed. The subsynchronous one is characterized by higher amplitudes than the one at the running frequency. The STFT diagram, see Fig. 3.3, constitutes another tool that proves the presence of these higher amplitude subsynchronous vibrations and one may observe them at around $t = 70\ s$. Finally, at approximately $\Omega = 2150\ rad/s$, the previously multi-periodic motion converts to quasi-periodic, due to the Neimark-Sacker bifurcation occurrence, and several subsynchronous vibrations make their appearance, not yet in a way that can be compared with the two already dominating. The motion is depicted in Fig. 3.4i.

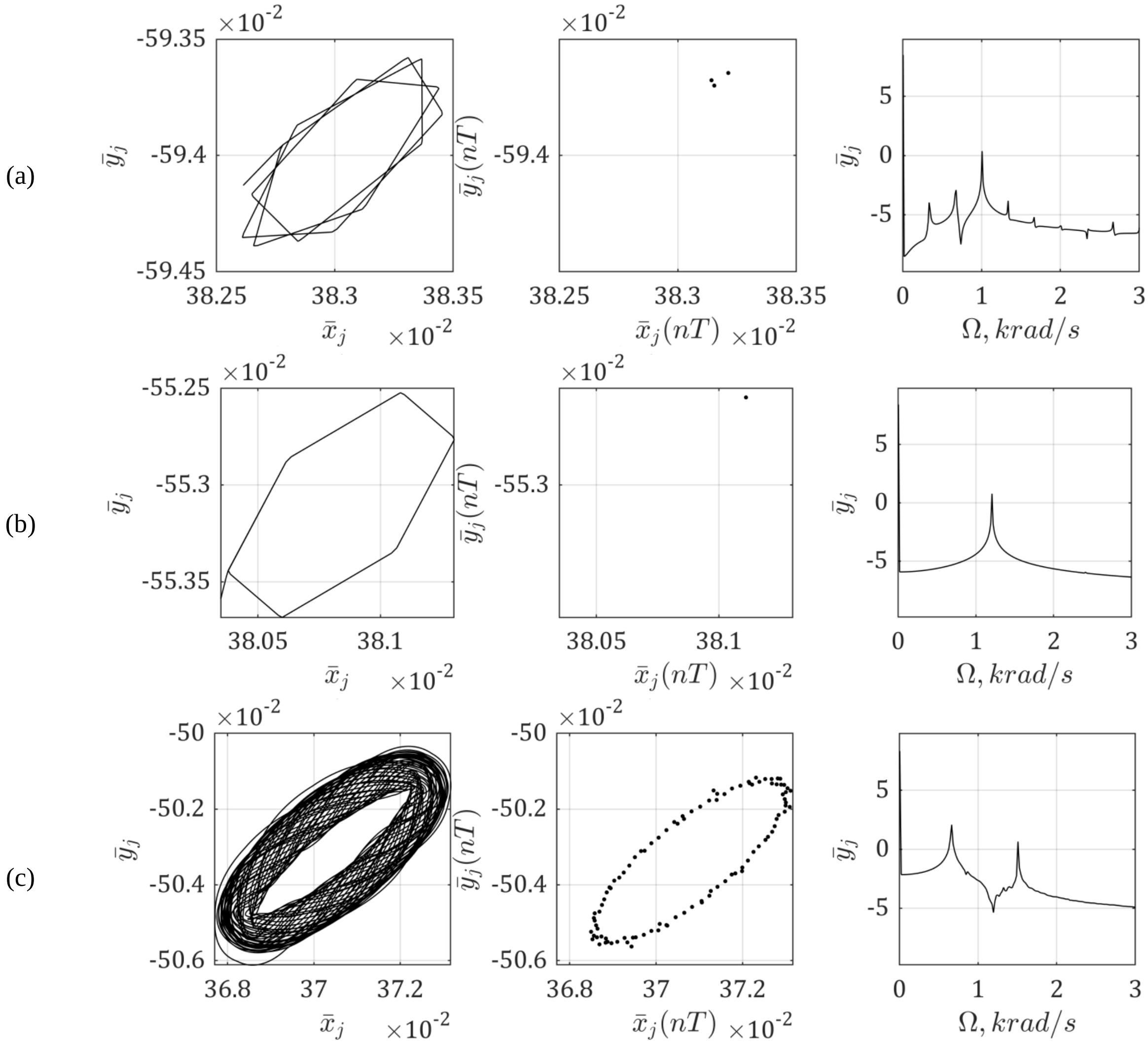

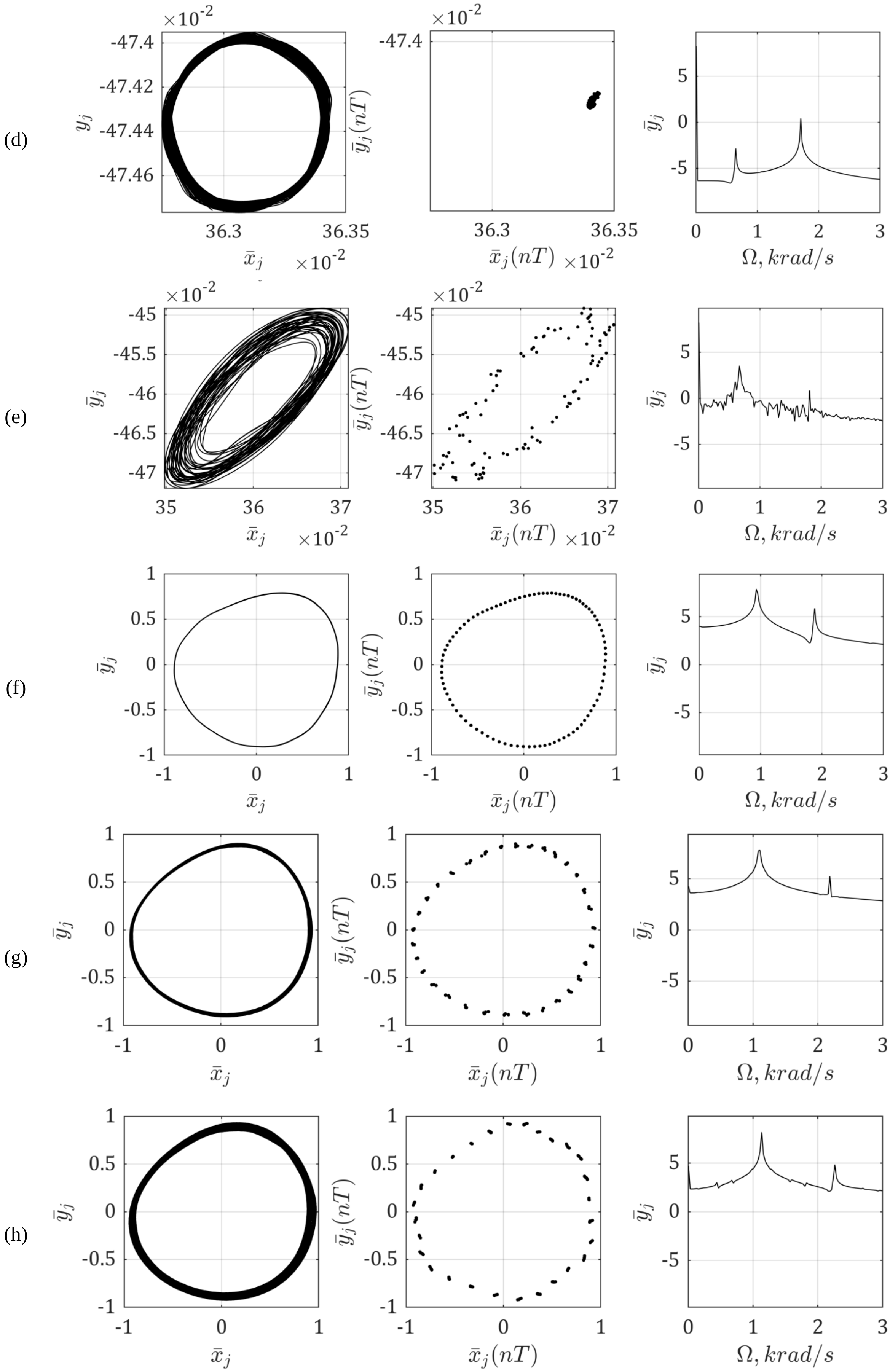
(d)
(e)
(f)
(g)
(h)
$\times 10^{-2}$
$\bar{y}_j$
$\bar{x}_j$
$\bar{y}_j(nT)$
$\bar{x}_j(nT)$
$\Omega, krad/s$
-47.4
-47.42
-47.44
-47.46
36.3
36.35
-45
-45.5
-46
-46.5
-47
35
36
37
1
0.5
0
-0.5
-1
5
-5
2
3

(i)

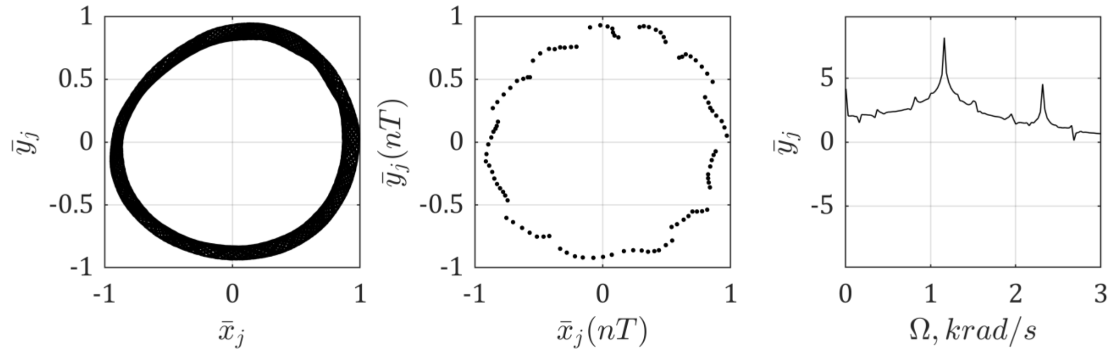

Fig. 3.4: Orbit, Poincaré and FFT diagrams for different speed Ω at unbalance $e = 0.5 \times 10^{-2} \times e_{iso} = 2.5 \times 10^{-8}\ m$: (a) $\Omega = 1000\ rad/s$, (b) $\Omega = 1200\ rad/s$, (c) $\Omega = 1500\ rad/s$, (d) $\Omega = 1700\ rad/s$, (e) $\Omega = 1800\ rad/s$, (f) $\Omega = 1850\ rad/s$, (g) $\Omega = 2050\ rad/s$, (h) $\Omega = 2100\ rad/s$, (i) $\Omega = 2150\ rad/s$

3.1 The influence of bump foil compliance in the unbalance response

The compliance $\overline{\alpha}_f$ of the bump foil structure constitutes one of the design parameters of this study, and one of the most influential factors when it comes to the dynamics of the rotor model. The foil compliance plays a critical role in terms of system's stability, which corresponds directly with the bifurcations' occurrence. Therefore, a series of diagrams are presented subsequently, where a comparative analysis for three different cases of foil compliance takes place; a stiff ($\overline{\alpha}_f = 0.01$), an intermediate ($\overline{\alpha}_f = 0.1$) and a compliant ($\overline{\alpha}_f = 1$) foil. The specifications of Table 3.1 are used during this investigative process.

Fig. 3.5 shows the STFT plots for each case of the dimensionless foil compliance, produced during the respective run-up simulations, and the corresponding bifurcation diagrams evaluated during the stepped run-up simulations. Significant conclusions can be drawn, especially by the bifurcation diagrams where major differences can be detected.

Table 3.2: Parameters used in the run-up and stepped run-up simulations of the system. Bearing specifications are considered as in Table 2.1

Parameter	Value	Parameter	Value
Shaft dimensionless stiffness, $\bar{k}_s$	1	Disc mass, m_d	3 kg
Foil loss factor, η	0.1	Journal mass, m_j	0.3 kg
Rotating acceleration, a	20 rad/s^2	Unbalance, $m_d \cdot$ e	$2.5 \cdot 10^{-6}$ kgm

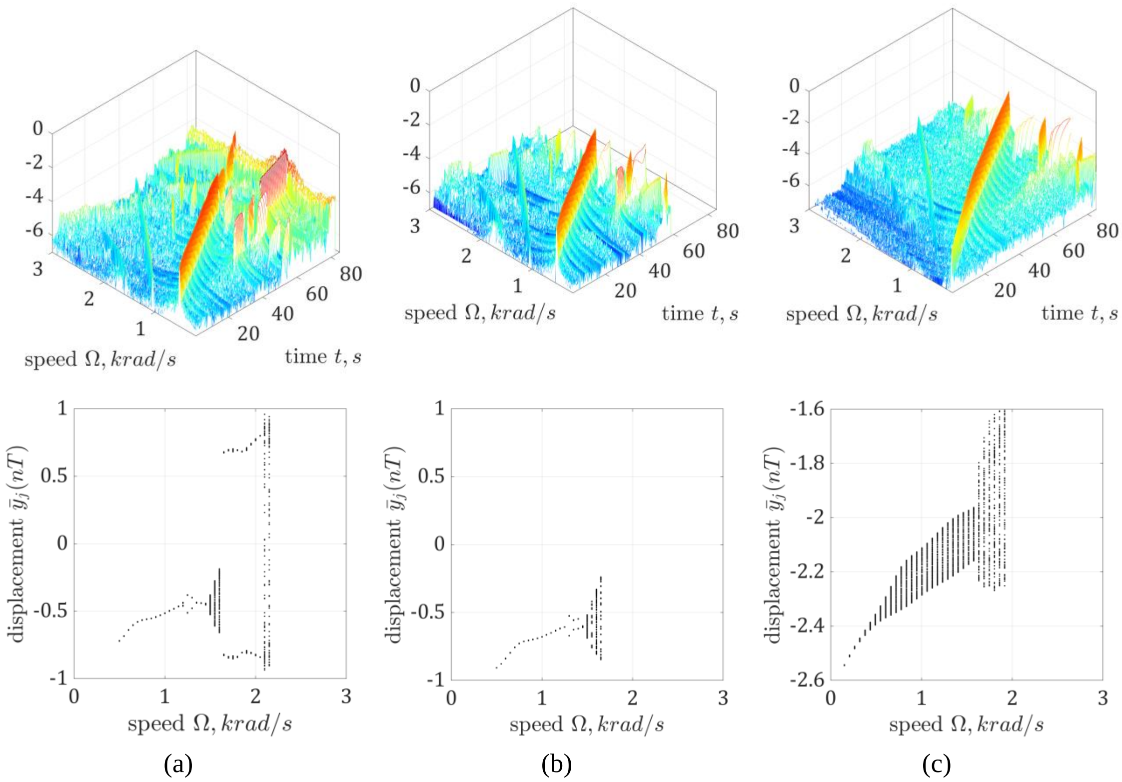

Fig. 3.5: (top) Time-frequency decomposition of the journal's transient response; (bottom) Bifurcation diagram obtained after a stepped run-up simulation; Parameters: $e = 0.5 \times e_{iso} = 2.5 \times 10^{-6}\ m, \overline{K}_s = 1, \eta = 0.1$; (a) $\overline{\alpha}_f = 0.01$, (b) $\overline{\alpha}_f = 0.1$, (c) $\overline{\alpha}_f = 1$

Starting from left to right, i.e. from the stiff foil to the most compliant, it is important to mention the different bifurcation types that the three systems experience. Fig. 3.5a shows the STFT and bifurcation diagrams for the stiff case, which was examined thoroughly in Section 2.4. In there, as rotating speed increases, at $\Omega = 1200\ rad/s$ a Hopf bifurcation takes place generating stable limit cycles, while at $\Omega = 1350\ rad/s$ another Hopf Bifurcation occurs, and the system returns to obtaining stable fixed points. At $\Omega = 1500\ rad/s$, another supercritical Hopf bifurcation occurs, meaning that once again stable limit cycles are generated. As the system increases speed, at $\Omega = 1650\ rad/s$, it experiences a saddle node bifurcation until rotating speed exceeds $\Omega = 2100\ rad/s$, when the last bifurcation type for this case is detected; the Neimark-Sacker bifurcation where the whip motion and, as a result, instability prevail.

Regarding the second case, at approximately $\Omega = 1300\ rad/s$ a Hopf bifurcation takes place inducing stable limit cycles, while at $\Omega = 1450\ rad/s$ another one occurs and the system obtains stable fixed points as it did at speed values lower than $\Omega = 1300\ rad/s$. With a slight speed increase, at $\Omega = 1500\ rad/s$, the system experiences once again a Hopf-Andronov bifurcation. Even if the first two cases presented many similarities in their dynamic behavior until a certain arithmetic value of Ω, the major difference between them lies ahead; the latest Hopf bifurcation that occurred in the second case is not followed by any other types of bifurcations. The solver breaks at speed $\Omega = 1650\ rad/s$ and the simulation is terminated. This obstacle may have been overcome if a different solver was chosen, such as 'ode45s' (implementing Runge-Kutta method), extending in this way the simulation and reaching higher rotating speed Ω.

Last, the compliant system from the very beginning experiences multi-periodic motions which generate stable limit cycles. In order to verify this, and rule out the possibility of an early occurred Hopf bifurcation, the initial rotating speed was considered at $\Omega = 200\, rad/s$. As it was expected, the system obtained stable fixed points at low speeds, but, as the speed was increasing, those converted to the afore written multi-periodic motions. At approximately $\Omega = 1650\, rad/s$, a subcritical Hopf bifurcation occurs, generating unstable limit cycles and chaotic motion. The system can hardly retain operation and integrity, and probably -with further increase in rotating speed- an undesirable rotor-stator contact will be taking place.

To summarize, one may notice that the least compliant foil, even if it experiences Hopf bifurcations slightly earlier than the intermediate one and much earlier than the most compliant, it can manage reaching higher rotating speeds without risking to compromise the operation of the system. Additionally, the most compliant foil, under the specifications given in the beginning of the section, reaches to instability quite early. With regard to the time-frequency decomposition of the transient response per case, it is concluded that as foil compliance $\overline{\alpha}_f$ increases, less and of a lower amplitude self-excited vibrations are induced. Fig. 3.5a shows the STFT plot for the stiff system. It can be easily observed that, especially after approximately $t = 40\, s$, subsynchronous frequency vibrations arise with a higher amplitude than the synchronous one, while in the other two cases, even if both sub and super-synchronous vibrations may be arising too, they are not of the same multitude and amplitude with their respective synchronous ones.

Figs. 3.6-3.8 provide the results of a comparative case-study that is being conducted for the first design parameter, the dimensionless foil compliance. In each figure, for a certain speed value, an orbit plot, a Poincaré map, and an FFT diagram are obtained for three different values of the dimensionless foil compliance ($\overline{\alpha}_f = \{0.01, 0.1, 1\}$), having secured that in every case steady state prevails. The chosen speeds, for the performed case-study, are $\Omega = \{1200, 1300, 1650\}\, rad/s$. Since selecting a higher rotating speed was not feasible, due to the fact that the solver broke during the second simulation ($\overline{\alpha}_f = 0.1$) at speed $\Omega = 1650\, rad$, this was the best-case scenario for the current comparative analysis.

Fig. 3.6 shows the results obtained at speed $\Omega = 1200\, rad/s$ for each one of the foil compliance values, providing the reader with the ability to distinguish major differences when it comes to the behavior among stiff or more compliant foil structures. Starting from the stiffest foil, see Fig. 3.6a, one may notice a period $2T_d$ motion from the Poincaré map, due to a Hopf bifurcation that occurs at this speed generating stable limit cycles. The FFT diagram shows four distinct peaks, with two of them being of a much higher amplitude explaining the two-periodic motion. Simultaneously, for $\overline{\alpha}_f = 0.1$, a period $1T_d$ motion is observed and stable fixed points are obtained by the system, while for the most compliant foil ($\overline{\alpha}_f = 1$) the Poincaré map shows a multi-periodic motion. It is of significant importance to mention that the orbital motions and the points shown in the Poincaré maps, are detected in lower vertical displacement values, as the foil becomes more compliant. As the foil compliance $\overline{\alpha}_f$ increases, the vertical displacement $\overline{y}_j$ of the journal decreases (or the modulus of $\overline{y}_j$ increases), and the eccentricity of the journal increases as well. At speed $\Omega = 1300\ rad/s$, the stiff foil still experiences period $2T_d$ motion.

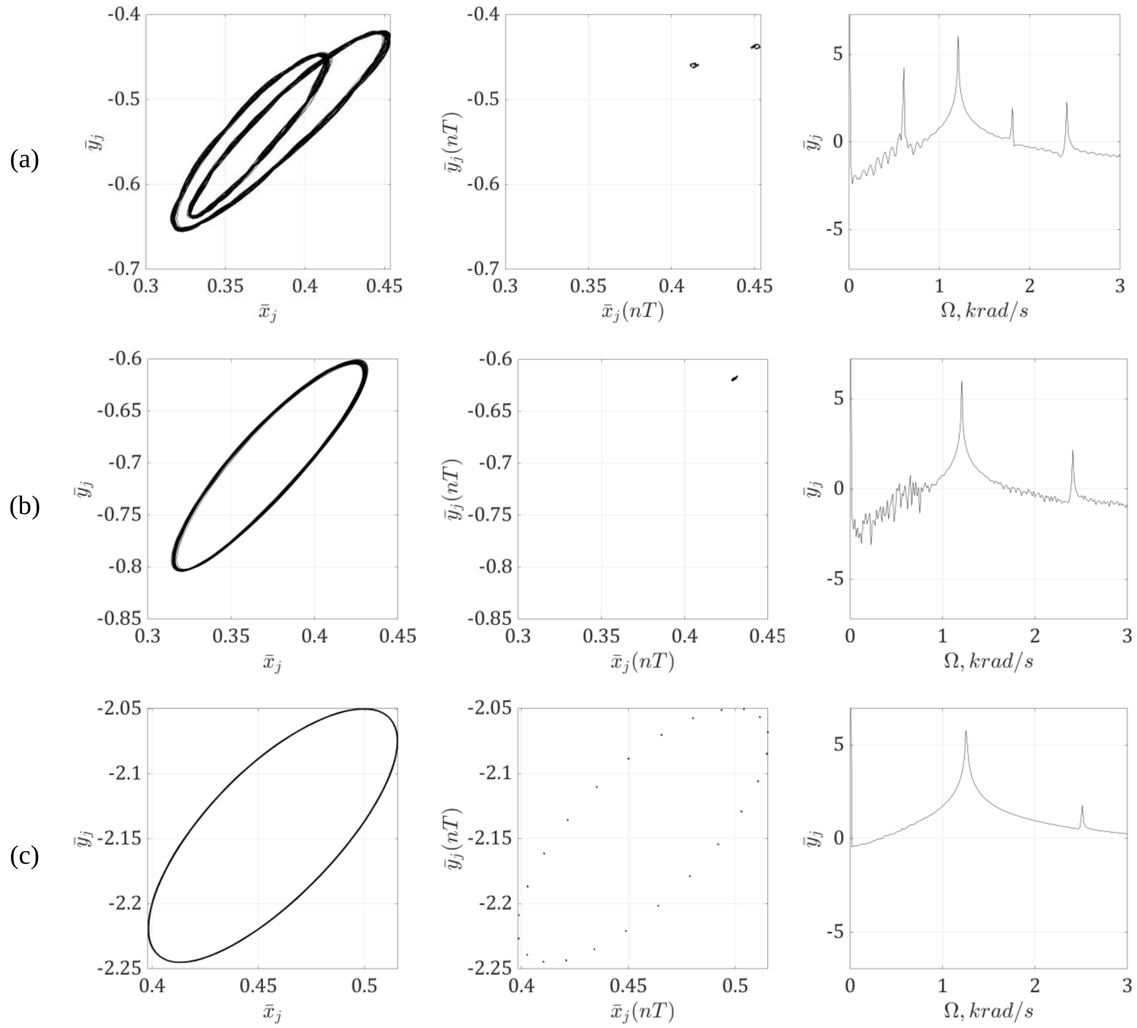

Fig. 3.6: Orbit, Poincaré and FFT diagrams at $\Omega = 1200$ rad/s with foil compliance (a) $\overline{\alpha}_f = 0.01$, (b) $\overline{\alpha}_f = 0.1$, $\overline{\alpha}_f = 1$

No alteration in terms of the motion's quality is detected in the most compliant foil ($\overline{\alpha}_f = 1$), and a multi-periodic motion continues to exist, as Fig. 3.7b depicts. The major difference is noticed in the second case, where $\overline{\alpha}_f = 0.1$. At this speed, a Hopf bifurcation occurs for the first time and periodic motions of period $2T_d$ are detected. The Poincaré map consists of two points, see Fig. 3.7b. Apparently, the two stiffest system trajectories geometrically form a similar orbital motion, after both of them experience Hopf bifurcation for first time. One may observe that as the foil compliance increases, the eccentricity does too. Specifically, the Poincaré distinct points in Fig. 3.7a are noticed in the range $\boldsymbol{\overline{y}_j = (-0.5, -0.4)}$, while in Fig. 3.7b in the range $\boldsymbol{\overline{y}_j = (-0.7, -0.5)}$ and in Fig. 3.7c, the multi-periodic motion of the system takes place in the range $\boldsymbol{\overline{y}_j = (-2.25, -2)}$.

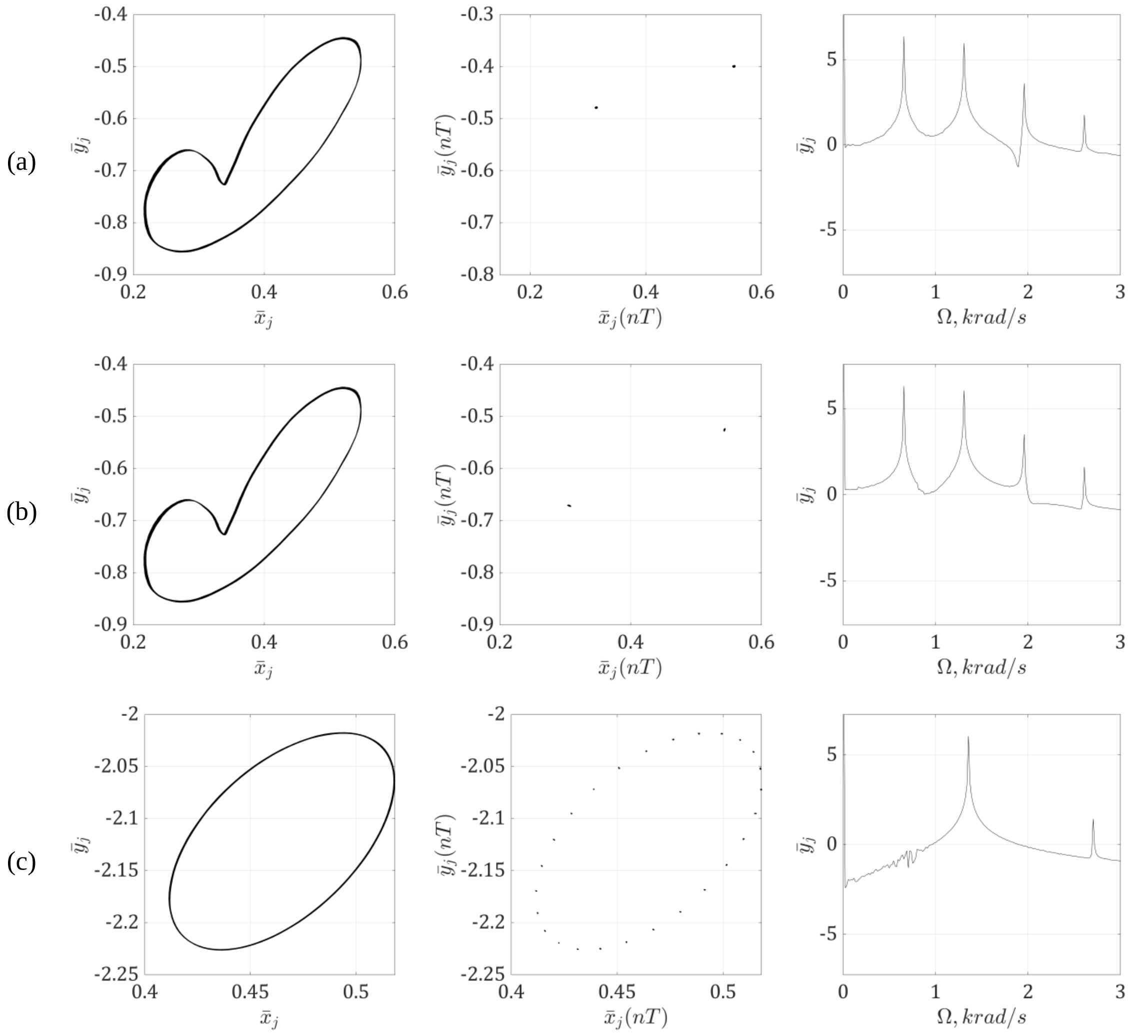

Fig. 3.7: Orbit, Poincaré and FFT diagrams at $\Omega = 1300$ rad/s with foil compliance (a) $\overline{\alpha}_f = 0.01$, (b) $\overline{\alpha}_f = 0.1$, $\overline{\alpha}_f = 1$

At approximately $\Omega = 1500$ rad/s, the first two systems experience a Hopf bifurcation, while the third one does not, until further increase of the rotating speed to $\Omega = 1650$ rad/s. At the same speed, though, the stiffest system ($\overline{\alpha}_f = 0.01$) experiences a saddle node bifurcation. In the following figure, the orbit, Poincaré and FFT diagrams are presented for the three systems, at speed $\Omega = 1650\ rad/s$. The first system, see Fig. 3.8a, develops one type of trajectory close to the clearance circle. The respective Poincaré map shows two distinct points, unveiling the period $2T_d$ motion of the stiff model. Regarding the second case, see Fig. 3.8b, multi-periodic motions are detected, as shown in the Poincaré map which consists of clearly discretized points in a geometrically defined shape. The corresponding FFT diagrams are characterized by multiple peaks, representing the several frequency vibrations of this, multi-periodic motion. Last, the most compliant foil develops unstable limit cycles, as the orbit map indicates in Fig. 3.8c. This is the result of a subcritical Hopf bifurcation and, according to the Poincaré map, leads to chaotic motions and several peaks in the FFT diagram.

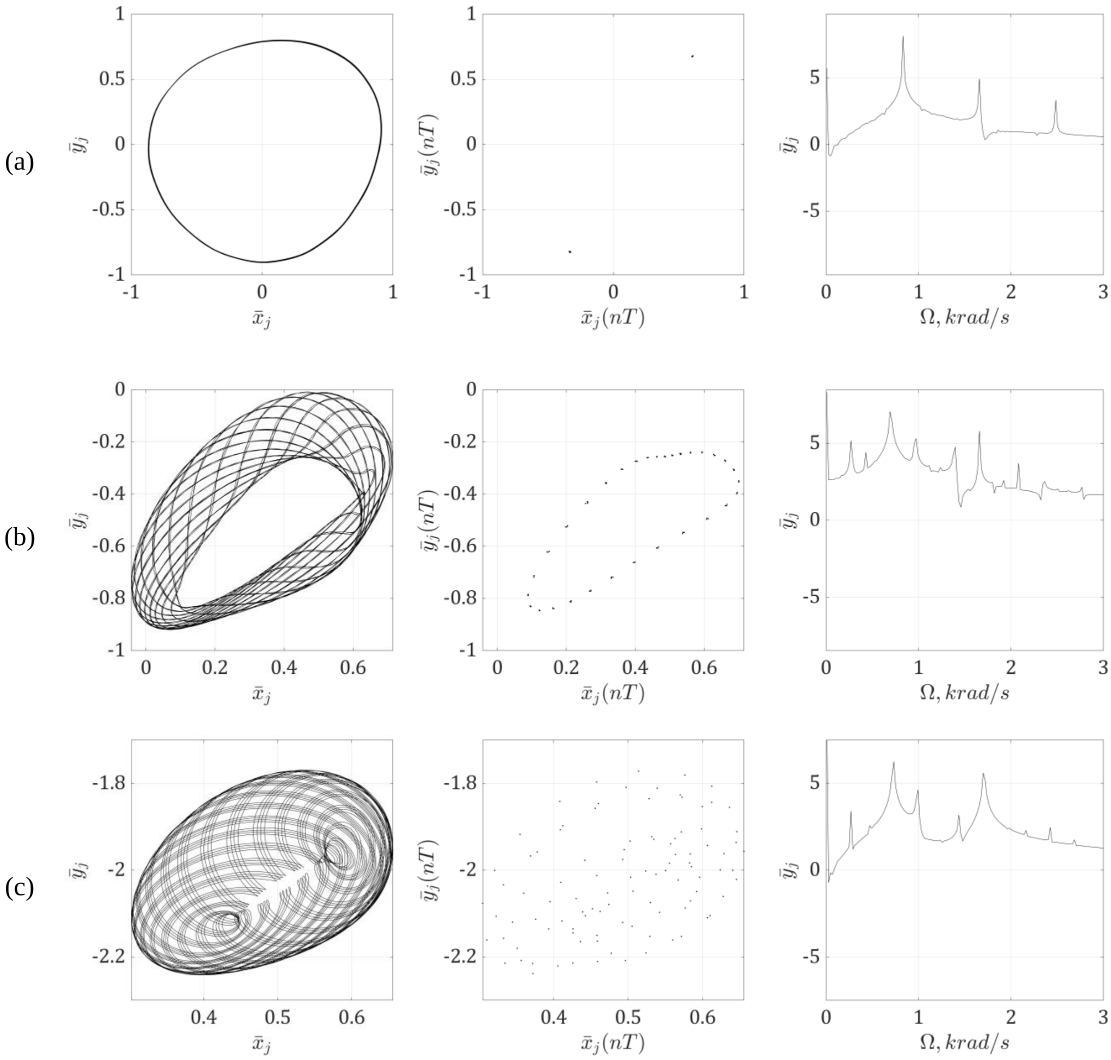

Fig. 3.8: Orbit, Poincaré and FFT diagrams at $\Omega = 1650$ rad/s with foil compliance (a) $\overline{\alpha}_f = 0.01$, (b) $\overline{\alpha}_f = 0.1$, $\overline{\alpha}_f = 1$

3.2 The influence of bump foil loss factor in the unbalance response

In order to investigate the influence of the loss factor on the dynamics of the rotor, the STFT and bifurcation plots are investigated with loss factor being the only changing parameter in this section. Right after, the same process is followed as in section 3.1 in order to obtain the orbit, Poincaré and FFT diagrams, for three different values of loss factor $\eta = \{0.003, 0.01, 0.1\}$. A comparative analysis takes place, where for certain rotating speeds the behavior of each system is studied and several conclusions can be drawn.

Fig. 3.9 shows the time-frequency decomposition of the transient response of the journal and the respective bifurcations plots, obtained via the stepped run-up simulations. From left to right, the loss factor increases, from its lowest value $\eta = 0.003$ to the highest $\eta = 0.1$. Regarding the first case, when the system rotates with low speed $\Omega < 1250\ rad/s$, it experiences stable motions around equilibrium for any initial condition, and the bifurcation plot shows only one distinct point at those speeds. At speed $\Omega = 1250\ rad/s$, a Hopf bifurcation occurs and stable limit cycles are induced, until $\Omega = 1350\ rad/s$, where another Hopf bifurcation occurs and the system returns to the previous quality of motion, obtaining stable fixed points. Increasing speed further, at approximately $\Omega = 1600\ rad/s$, a Hopf bifurcation occurs once again and stable limit cycles are induced. Following this supercritical Hopf bifurcation, at approximately speed $\Omega = 1700\ rad/s$, a saddle node bifurcation occurs and the system develops one type of trajectory, close to the clearance circle regardless the initial position of the unbalance magnitude. From now on, period $2T_d$ motions are induced, as the respective Poincaré map indicates, evaluated for a much higher speed $\Omega = 2050\ rad/s$, see Fig. 3.12a.

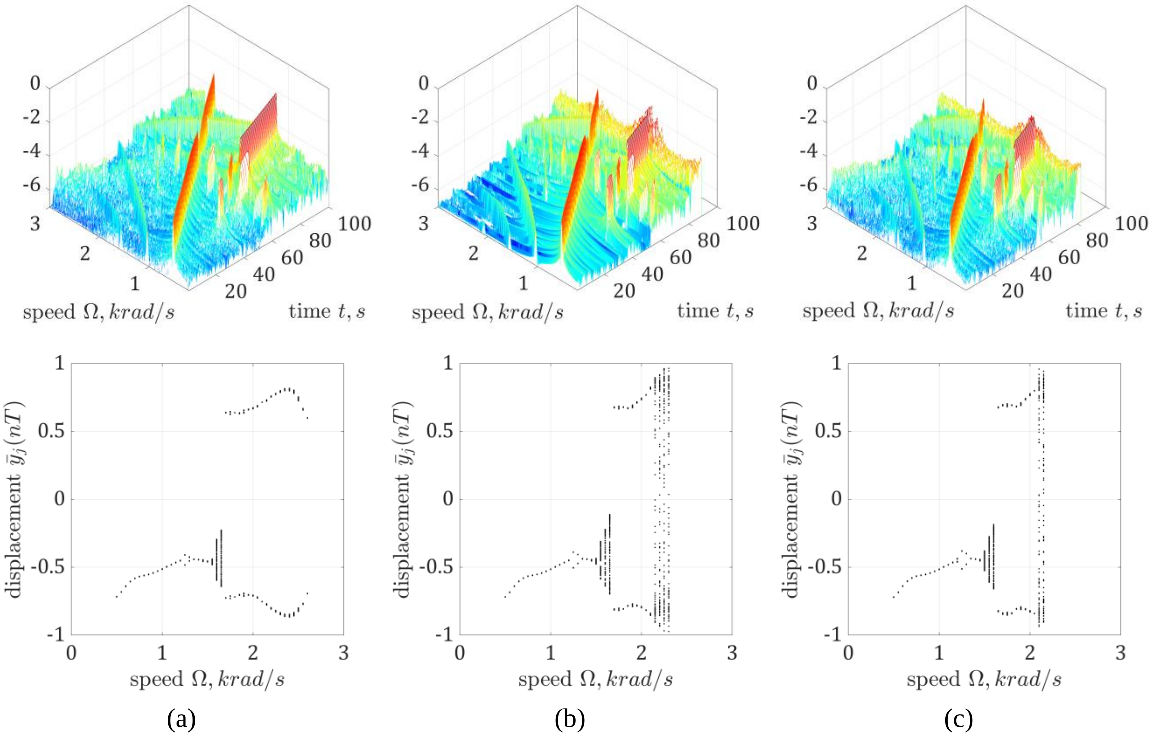

Fig. 3.9: (top) Time-frequency decomposition of the journal's transient response. (bottom) Bifurcation diagram obtained after a stepped run-up simulation; Parameters: $e = 0.5\ \times e_{iso} = 2.5 \times 10^{-6}\ m, \bar{K}_s = 1, \bar{\alpha}_f = 0.01$; (a) $\eta = 0.003$, (b) $\eta = 0.01$, (c) $\eta = 0,1$

The rest of the two cases follow a similar behavior in regards to the quality of motions with the first one until speed $\Omega = 2050\ rad/s$. Specifically, for loss factor $\eta = 0.01$, the first Hopf bifurcation occurs at exactly the same speed $\Omega = 1250\ rad/s$, while the second one takes place again at the same speed $\Omega = 1350\ rad/s$. In between the two Hopf bifurcations, stable limit cycles are generated. As the system increases speed further, at approximately $\Omega = 1550\ rad/s$ ($50\ rad/s$ earlier than the first case), another Hopf bifurcation occurs and quasi-periodic motions are developed. At speed $\Omega = 1700\ rad/s$, a saddle node bifurcation occurs, until speed $\Omega = 2150\ rad/s$. At this point, a Neimark-Sacker bifurcation occurs, and stable limit cycles will be generated. Fig. 3.9b shows that the transition to the next quality of motion is achieved gradually, leading to the conclusion that the Neimark-Sacker bifurcation is supercritical and explaining the aforementioned existence of stable limit cycles. With further increase in speed, the journal will most likely experience contact with the bearing and the operation trips.

Regarding the last system, where $\eta = 0.1$, at speed $\Omega = 1200\,rad/s$ the first Hopf bifurcation occurs, and period $2T_d$ motion prevails, as the corresponding Poincaré map shows in continue. At approximately $\Omega = 1350\,rad/s$, the second Hopf bifurcation occurs and the system returns to the previous state, where stable motions around equilibrium are detected. As speed increases, at approximately $\Omega = 1500\,rad/s$, the system experiences the third Hopf bifurcation, resulting to whirl motion under stable limit cycles. At $\Omega = 1650\,rad/s$, a saddle node bifurcation occurs, approximately $50\,rad/s$ earlier than the previous two cases. Finally, at rotating speed $\Omega = 2100\,rad/s$, a subcritical Neimark-Sacker bifurcation occurs, resulting to unstable limit cycles. Once again, the bifurcation diagram, see Fig. 3.9c, proves the unstable nature of the limit cycles, since the transition to this motion is not gradual. With further increase at speed, the system will experience rotor-stator contact.

The orbit, Poincaré, and FFT diagrams are evaluated in Figs. 3.10-3.12, for three different values of rotating speed, so as to investigate the quality of motion per case at the same time point. Fig. 3.10 shows the results that the simulations extracted for $\Omega = 1200\,rad/s$. Regarding the first system, where $\eta = 0.003$, period $1T_d$ motion is observed, since the Poincaré map shows a single distinct point, see Fig. 3.10a. The FFT plot indicates the presence of a subsynchronous and a supersynchronous vibration frequency in addition, with much lower amplitudes than the synchronous one though. The STFT diagram, shown in Fig. 3.9a, affirms the presence of these frequencies as well. The same quality of motion is detected in the second system too. However, this is not the case in the third one. The system, at this speed, experiences a Hopf bifurcation and the single period motion converts to period $2T_d$.

In continue, at approximately $\Omega = 1650\,rad/s$, the motion of the first two systems transforms to quasi-periodic, after both experiencing a Hopf-Andronov bifurcation. The corresponding FFT plots show several peaks, see Figs. 3.11a-b. The last system ($\eta = 0.1$) renders a period $2T_d$ motion, as a result of the saddle node bifurcation that occurred at this speed. A close-to-clearance circle trajectory is detected, as it is expected when a saddle node bifurcation occurs.

(a)

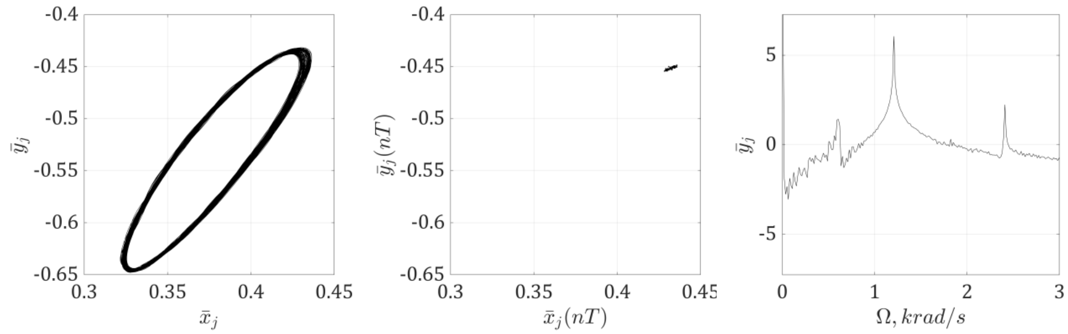

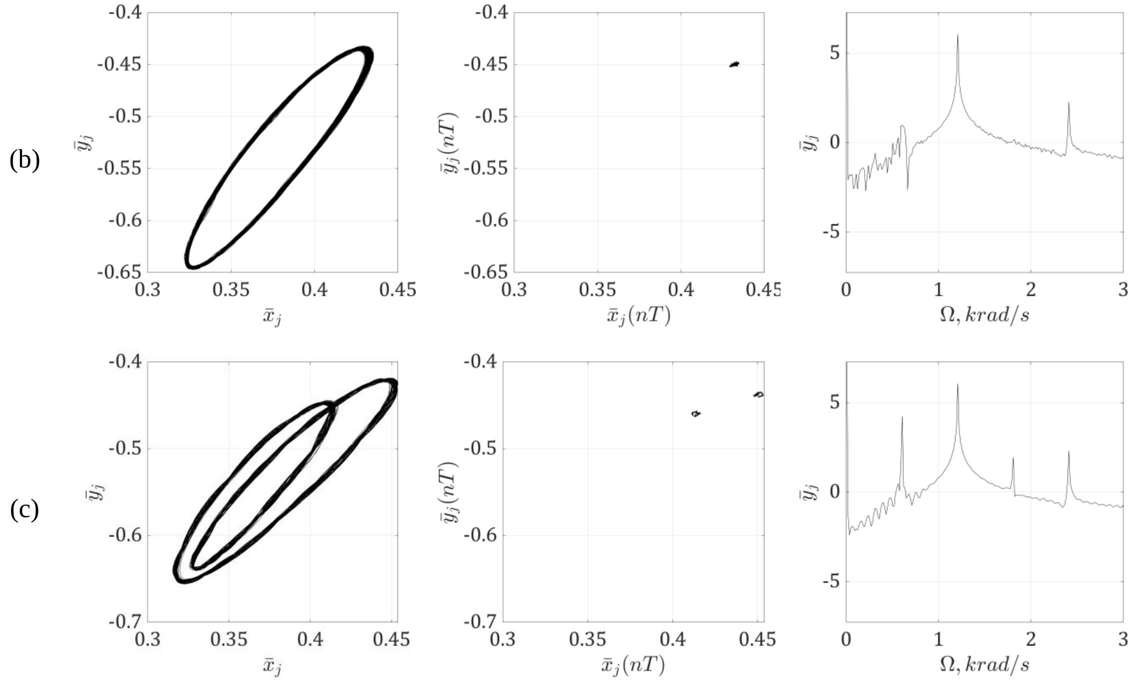

Fig. 3.10: Orbit, Poincaré and FFT diagrams at $\Omega = 1200\,\text{rad/s}$ with foil loss factor (a) $\eta = 0.003$, (b) $\eta = 0.01$, $\eta = 0.1$

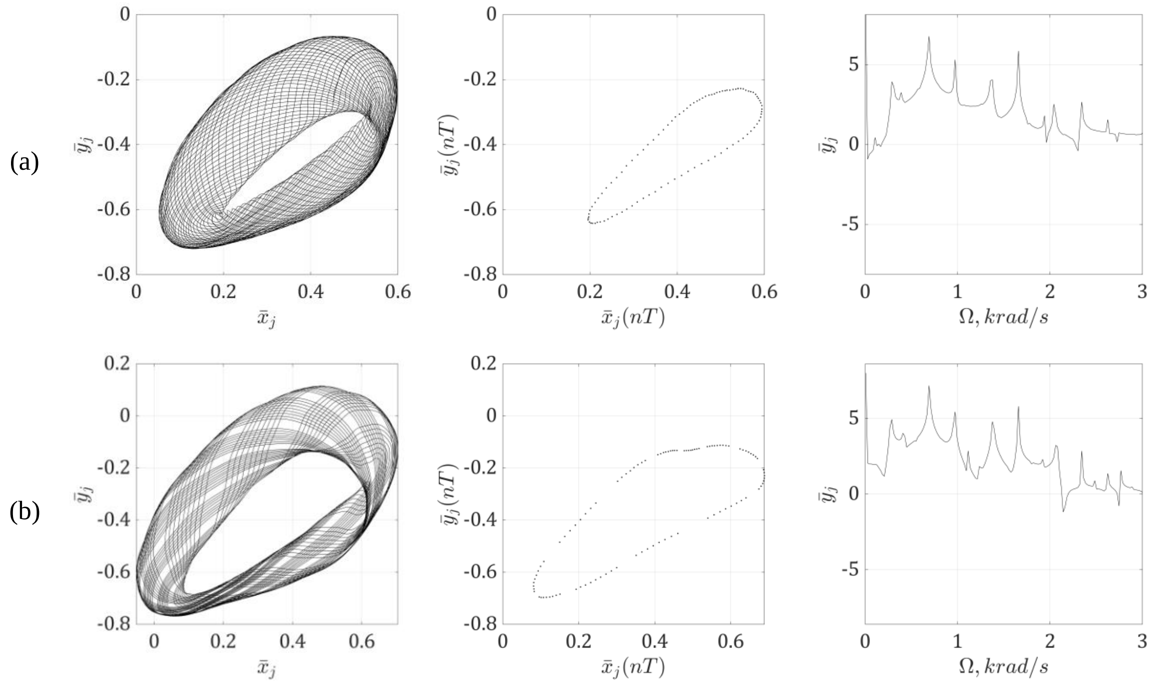

(c)

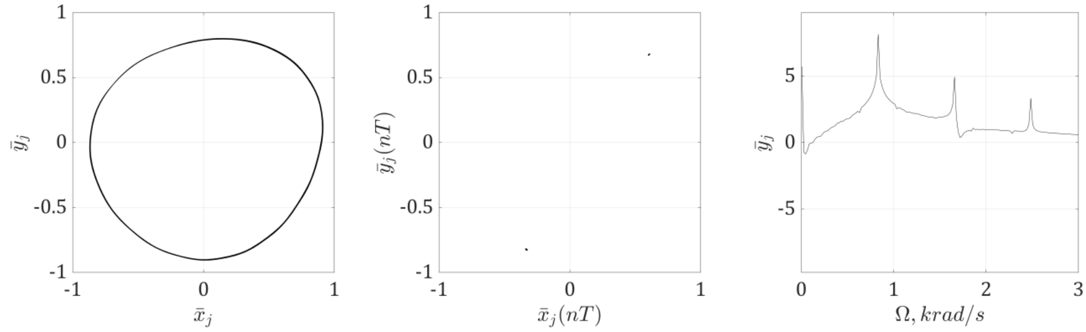

Fig. 3.11: Orbit, Poincaré and FFT diagrams at $\Omega = 1650$ rad/s with foil loss factor (a) $\eta = 0.003$, (b) $\eta = 0.01$, $\eta = 0.1$

To conclude, Fig. 3.12 renders the respective diagrams for a significantly higher speed. Exceeding $\Omega = 2000\, rad/s$, and more precisely at $\Omega = 2150\, rad/s$, interesting observations can be made. One may notice different types of bifurcations in this part. With regard to the first case, where the value of the damping factor is the lowest one, there is no alteration in the quality of the motion. The period $2T_d$ motion continues to exist, the trajectory of the journal is still close to the clearance circle and the FFT plot shows clearly two distinct peaks, which represent the two vibration frequencies of the motion -- the synchronous and a subsynchronous one. After the saddle node bifurcation that occurred at approximately $\Omega = 1650\, rad/s$, minor alteration took place. With further speed increase, the solver breaks and the simulation terminate.

The second system, though, experiences a supercritical Neimark-Sacker bifurcation, as previously mentioned, and quasi-periodic motions are detected. The FFT plot shows several peaks, not clearly discretized though, see Fig. 3.12b. Last but not least, for the third system ($\eta = 0.1$), the corresponding diagrams represent once again quasi-periodic motions, which constitute the result of a subcritical Neimark-Sacker bifurcation. The most remarkable observation that can be made is that for the selected design parameters ($\bar{K}_s = 1, \bar{\alpha}_f = 0.01$) and an unbalance eccentricity $m_d \cdot \mathrm{e} = 7.5 \times 10^{-6}$ kgm the system shows similar behavior until rotating speed reaches $\Omega = 2150\, rad/s$, regardless the value of the loss factor. However, by the time Ω surpasses this value and as the loss factor η of the gas foil bearing increases, the quality of motion of the system varies decisively. For the lowest value of the loss factor, $\eta = 0.003$, the simulation is terminated at $\Omega = 2600\, rad/s$, without any other bifurcation type occurring, while for the intermediate one, $\eta = 0.01$, a supercritical Neimark-Sacker bifurcation occurs and the simulation is terminated at $\Omega = 2300$ rad/s. Last, for the highest value, $\eta = 0.1$, a subcritical Neimark-Sacker occurs and the solver breaks at $\Omega = 2150$ rad/s. Therefore, for the lowest values of loss factor, the system is able to reach higher amounts of speed without experiencing Neimark-Sacker bifurcations, averting to get closer to instability.

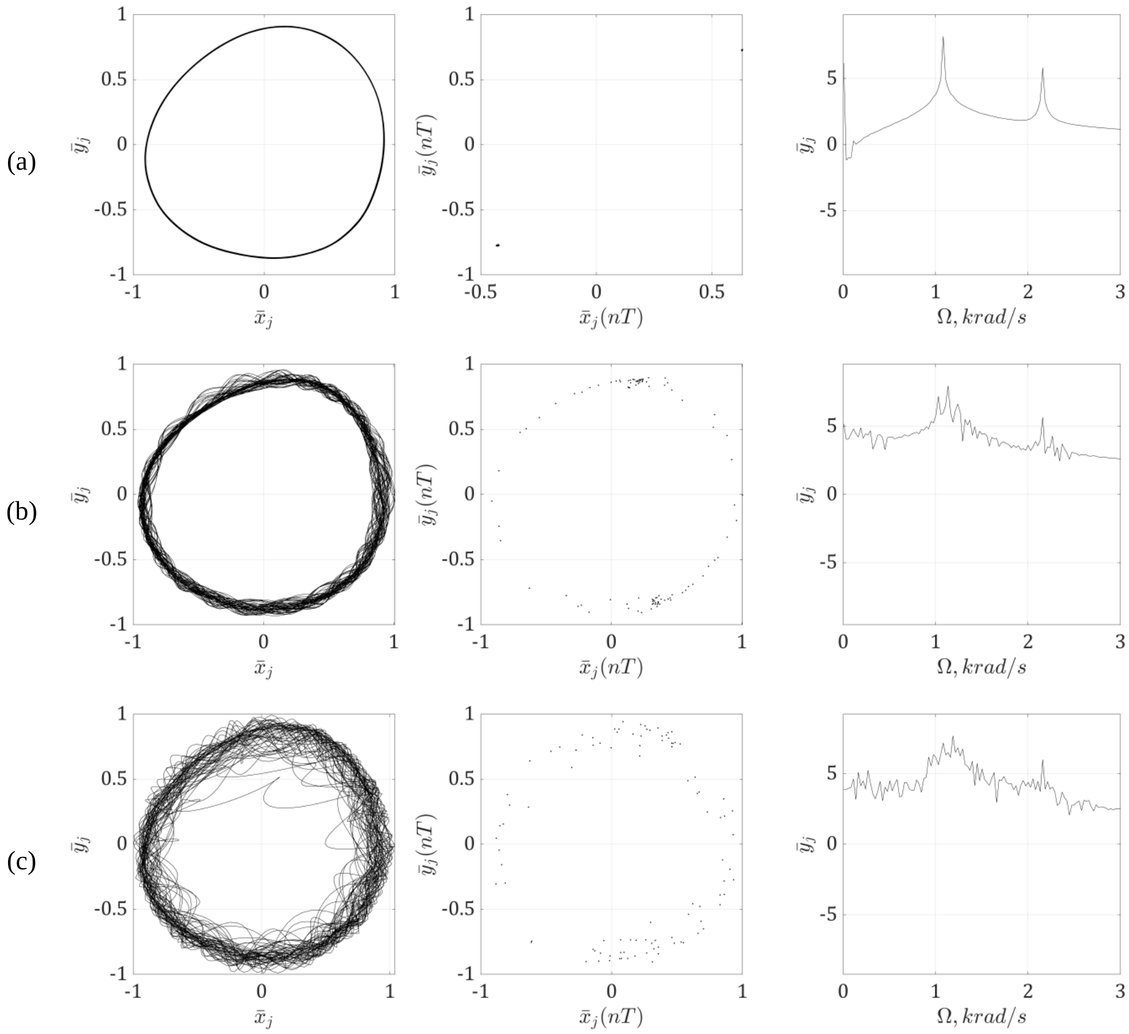

Fig. 3.12: Orbit, Poincaré and FFT diagrams at $\Omega = 2150\,\mathrm{rad/s}$ with foil loss factor (a) $\eta = 0.003$, (b) $\eta = 0.01$, $\eta = 0.1$

3.3 Energy flow

The work of gas forces and of forces acting on the top foil, by foil springs and foil dampers are evaluated for a closed trajectory of the journal motion during the performed stepped run-ups for the designated in Table 3.1 cases. The equations utilized for the work computations are defined in Eq. (90) for the total work of gas forces W_g, in Eq. (91) for the total work of the forces acting on the inner surface of the top foil W_f, in Eq. (92) for the total work of the bump foil spring W_{k_f}, and in Eq. (93) for the total work of the bump foil damper W_{c_f}:

$$\boldsymbol{W_g = W_{g_x} + W_{g_y} = \sum F_{B_x} \times \Delta x_j + F_{B_y} \times \Delta y_j} \tag{90}$$

$$\boldsymbol{W_f = \sum F_m \times \Delta q = \sum (p_m \cdot R \cdot \Delta\theta \cdot \Delta z) \times \Delta q} \tag{91}$$

$$W_{k_f} = \sum F_{k_f} \times \Delta q = \sum (k_f \cdot R \cdot \Delta\theta \cdot L \cdot q) \times \Delta q \tag{92}$$

$$W_{c_f} = \sum F_{c_f} \times \Delta q = \sum (F_m - F_{k_f}) \times \Delta q \tag{93}$$

The dimensional bearing forces F_{B_x}, F_{B_y} are given by (14)-(15), p_m is the mean pressure over the length L of the bearing, see (40), and F_m is the respective mean force. As Δx_j, Δy_j are denoted the difference of horizontal and vertical displacements between two consecutive points of the orbit, while the same applies to the respective consecutive orbit points when it comes to the evaluation of the foil displacement difference Δq.

The process followed so as to ensure that the works were evaluated in a closed orbit, and extract -in this way- valid results, lies ahead: a certain "if statement" is introduced, where by the time an orbit point surpasses for the second time a vertical axis created by the first plotted orbit point -meaning that this point belongs to the vertical axis- then the evaluation has to be terminated. However, having observed several trajectories' instances in the previous sections, one may claim that the geometry of an orbit is not always circular or elliptical so as to ensure that a closed loop is achieved. At these cases, the closed loop process has to implement manually.

The main target of the current evaluations is to provide the reader with conclusions, regarding the energy flow of the systems studied. Fig. 3.13 shows three different systems, sharing the same properties in all design parameters, except for the loss factor which starting from the first system, increases and takes values $\eta = \{0.003, 0.01, 0.1\}$. The rest of the design variables are the shaft stiffness and the foil compliance, where $\bar{k}_s = 1$ and $\bar{a}_f = 0.01$ respectively, while the unbalance eccentricity is given as $e = 2.5 \times 10^{-6}$ kgm.

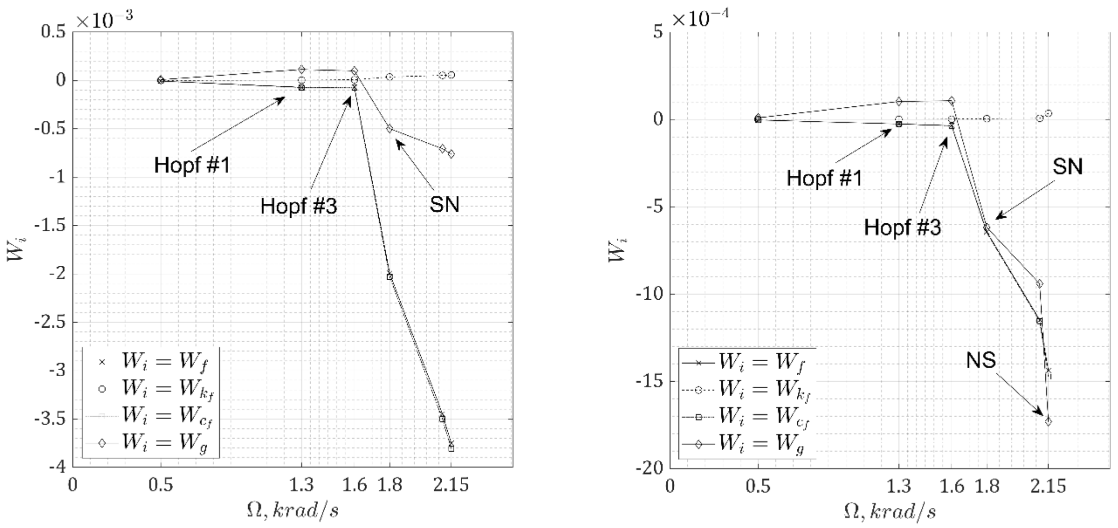

(a) (b)

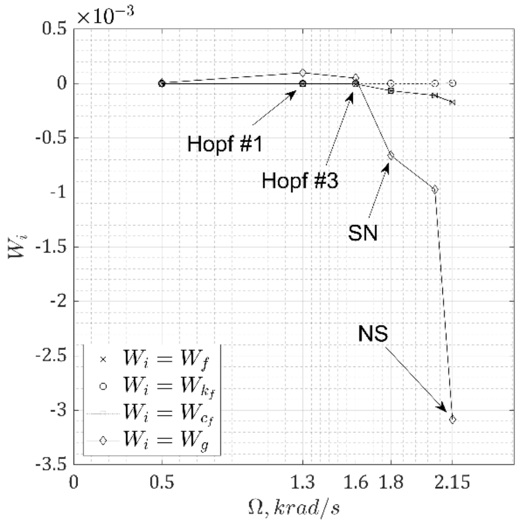

(c)

Fig. 3.13: Works W_i evaluated for different values of rotating speed Ω, shaft stiffness $\bar{k}_s = 1$, foil compliance $\bar{a}_f = 0.01$, unbalance eccentricity $e = 2.5 \times 10^{-6}$ kgm, and three different properties of loss factor η: (a) $\eta = 0.003$ (case B1a2) – $\Omega = \{500,1300,1600,1800,2100,2150\}\ rad/s$, (b) $\eta = 0.01$ (case B1b2) - $\Omega = \{500,1300,1600,1800,2100,2150\}\ rad/s$, (c) $\eta = 0.1$ (case B1c2) – $\Omega = \{500,1300,1600,1800,2050,2150\}\ rad/s$.

It should be noted that the evaluation of work is executed for certain rotating speeds that are chosen deliberately when major incidents occur, i.e. bifurcations, and slightly earlier before they take place during the stepped run-up of each system. Briefly, the first system (B1a2) experiences a Hopf bifurcation at speed $\Omega = 1250\ rad/s$, and another one Hopf bifurcation at $\Omega = 1350\ rad/s$, where in the first case stable limit cycles are induced while in the second the system returns to stable fixed points. At speed $\Omega = 1600\ rad/s$, another Hopf bifurcation occurs, leading to whirl motion, right before a saddle node bifurcation occurs at $\Omega = 1700\ rad/s$ and period $2T_d$ is detected. The second system experiences the first Hopf bifurcation again at speed $\Omega = 1250\ rad/s$, the second at $\Omega = 1350\ rad/s$ and the third one at $\Omega = 1550\ rad/s$. A saddle node bifurcation occurs at rotating speed $\Omega = 1700\ rad/s$, and last, a supercritical Neimark-Sacker bifurcation at $\Omega = 2150\ rad/s$. The third system experiences the same types of bifurcations (first Hopf at $\Omega = 1250\ rad/s$, second Hopf at $\Omega = 1350\ rad/s$, third Hopf at $\Omega = 1500\ rad/s$ and saddle node at $\Omega = 1650\ rad/s$), as explained thoroughly in this chapter, except for the Neimark-Sacker bifurcation that occurs in the end which in this case is subcritical and takes place at $\Omega = 2100\ rad/s$.

Regarding the energy flow, Fig. 3.13 shows that in each case great similarities are observed. The importance of bifurcations is reflected and one may notice that the energy flow experiences its most significant variations when certain types of bifurcations occur. Specifically, in all three cases, as speed increases the work of gas forces is positive and remains positive throughout the three Hopf bifurcations that occur. However, by the time the saddle node bifurcation occurs, the work renders negative values until the end of the simulation, meaning that energy consumption exists from this point on. With regard to the foil damper and the foil in general, from the very beginning energy consumption exists and a steep descent is detected when the saddle node bifurcation occurs, inducing even greater energy consumption. Another noteworthy conclusion is that, as the foil damping factor (loss factor) increases, the maximum modulus of the work of gas forces per case increases too, while the respective maximum modulus of the work value, that the foil damping forces and the forces acting on top foil in general produce, decreases.

Interesting observations can be also made for another value of shaft stiffness, with the parameter of loss factor η to be retained as the one changing. Specifically, the shaft stiffness will convert to $\bar{k}_s = 10$, making the shaft of the new systems ten times stiffer than the shaft of the previous case-study. The new cases under investigation are now the (C1a2), (C1b2), and (C1c2).

Before getting into the Fig. 3.14 analysis, it is useful to provide the reader with the necessary information, regarding the bifurcations occurred in each system. In the first case, a supercritical Hopf bifurcation occurs at speed $\Omega = 1300\, rad/s$, generating stable limit cycles, while at $\Omega = 1350\, rad/s$ another Hopf bifurcation occurs and the system returns to stable fixed points. At speed $\Omega = 1600\, rad/s$, the system experiences a third Hopf bifurcation and presents whirl motion. Last, at $\Omega = 1750\, rad/s$, a saddle node bifurcation occurs and a two-periodic motion prevails until the end of the simulation. Concerning the second case, the same bifurcation types are detected for the largest part of the simulation, although at different values of speed Ω. The first Hopf bifurcation occurs at $\Omega = 1250\, rad/s$, the second at $\Omega = 1400\, rad/s$, and the third one at $\Omega = 1600\, rad/s$. In continue, at speed $\Omega = 1800\, rad/s$, the system experiences a saddle node bifurcation until speed's increase to $\Omega = 2200\, rad/s$, where a Neimark-Sacker bifurcation takes place. Last, the third system shows similar behavior with the previous one, except for the speed values where the respective bifurcations occur. At speed $\Omega = 1250\, rad/s$, the system experiences the first Hopf bifurcation, while the second occurs at $\Omega = 1350\, rad/s$ and the third one at $\Omega = 1500\, rad/s$. The saddle node bifurcation takes place at $\Omega = 1750\, rad/s$, and the Neimark-Sacker at approximately $\Omega = 2000\, rad/s$.

Fig. 3.14 shows the evaluated works for several rotating speeds before and after the bifurcations mentioned earlier occur. Once again, the figure indicates that before the saddle node bifurcation the work produced by gas forces remains positive. Right after, the work becomes negative until the simulation is terminated by the solver. The major arithmetic variations are detected when the saddle node and the Neimark-Sacker bifurcations occur. In addition, it is indicated that as the property of the loss factor increases, the maximum modulus of the gas forces work increases as well (or in absolute numbers decreases and greater energy consumption exists), while the maximum modulus of the works produced by the forces acting on the top foil and the foil damping forces follows a declining path.

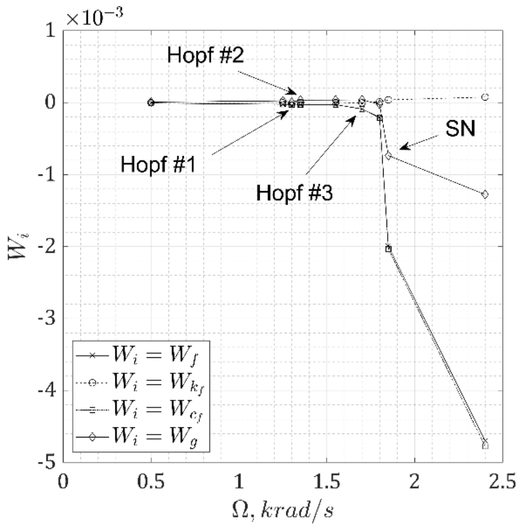

(a)

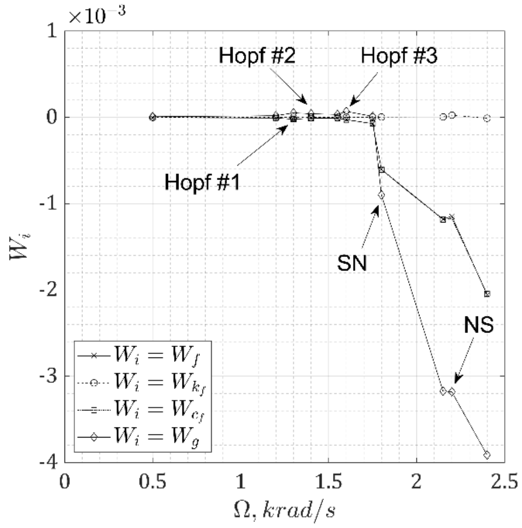

(b)

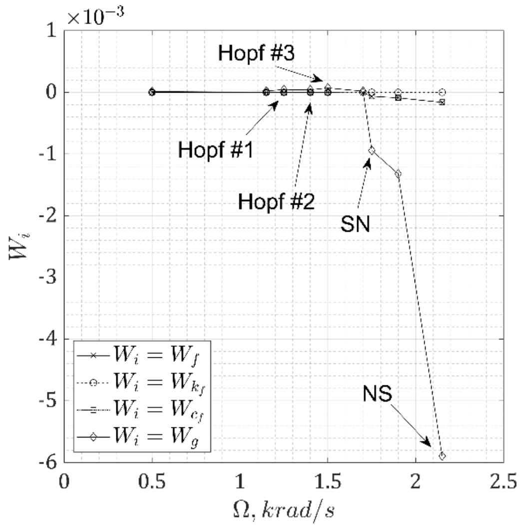

(c)

Fig. 3.14: Works W_i evaluated for different values of rotating speed Ω, shaft stiffness $\bar{k}_s = 10$, foil compliance $\bar{\alpha}_f = 0.01$, unbalance eccentricity $e = 2.5 \times 10^{-6}$ kgm, and three different properties of loss factor η: (a) $\eta = 0.003$ (case C1a2) – $\Omega = \{500,1250,1300,1350,1550,1700,1800,1850\}\ rad/s$, (b) $\eta = 0.01$ (case C1b2) - $\Omega = \{500,1200,1300,1400,1550,1600,1750,1800,2150,2200,2400\}\ rad/s$, (c) $\eta = 0.1$ (case C1c2) – $\Omega = \{500,1150,1250,1400,1500,1700,1750,1900,2150\}\ rad/s$.

To conclude, another case-study analysis takes place in Fig. 3.15. In comparison to the first one, what is modified is the foil compliance, which is equal to $\bar{\alpha}_f = 0.1$. Therefore, the under-investigation studies are now encoded as (B2a2), (B2b2), and (B2c2). Regarding the first case, as the rotating speed increases, period $1T_d$ motion is detected until approximately speed $\Omega = 2450\ rad/s$. Then, a Hopf bifurcation occurs, whip motion characterizes the system and with a slight speed increase the simulation is terminated. The second system experiences single periodic motion until speed $\Omega = 1700\ rad/s$, when a supercritical Hopf bifurcation occurs and whirl motion is rendered. The third system, where the highest foil damping is given as a specification, experiences a Hopf bifurcation at approximately speed $\Omega = 1300\ rad/s$. Period $1T_d$ motion is established, not for long though since another Hopf bifurcation occurs at $\Omega = 1350\ rad/s$ and the system returns to stable motions around fixed equilibrium points. At approximately $\Omega = 1500\ rad/s$, another Hopf bifurcation occurs and stable limit cycles are generated. With further increase of the rotating speed, the solver breaks and the simulation is terminated.

Similar observations with the previous two analyses can be extracted through Fig. 3.15. By the time the subcritical Hopf bifurcation occurs in the first system, a significant change is detected in the work produced by the foil damper forces. The same applies to the produced by the forces acting on the top foil work in general, since the respective work of the foil spring forces is experiencing almost negligible variation. The gas forces work retains its positivity throughout the whole simulation and approaches zero value when the Hopf bifurcation takes place. This is not the case in the rest of the systems, though. The second system experiences several Hopf bifurcations, but the major difference in comparison to the first one is that all of them are supercritical. The gas forces work remains positive and energy contribution exists, but there is no indication of following a declining path towards zero value, as in the previous system. Quite the opposite, one may claim. A remarkable observation is that, after approximately $\Omega = 1700\ rad/s$, it seems that even the work produced by the foil spring forces begins rendering values different that zero. Concerning the third case, once again, when the third bifurcation occurs the gas forces work experiences a steep descent and, surprisingly enough (in comparison with the previously investigated systems), surpasses the horizontal axis x, taking a negative value. One may claim that this constitutes an abnormality in comparison to what has been depicted in the rest of this section's diagrams and there is no way to define the reason that induced this sign change. A different solver's utilization would be an indicated alternative in order to explain this observation.

To sum up, a noteworthy conclusion can be drawn from the three executed case-study analyses in this section; the impact that certain types of bifurcations have in the energy flow of a system. More specifically, this study supports that Hopf bifurcations may induce several arithmetic variations when it comes to evaluating the works produced by the gas and foil damper (and consequently the foil in general) forces. However, none of them provokes a sign change and, by extensively, alteration in the energy balance. A saddle node bifurcation, though, constitutes a "balance changer", if a term like this one is allowed, since it leads to the aforementioned sign change regarding the gas forces work. From this point of view energy balance is changed and the gas forces work introduce energy in to the system, resulting is self-excited vibrations of high amplitude, close to radial circle.

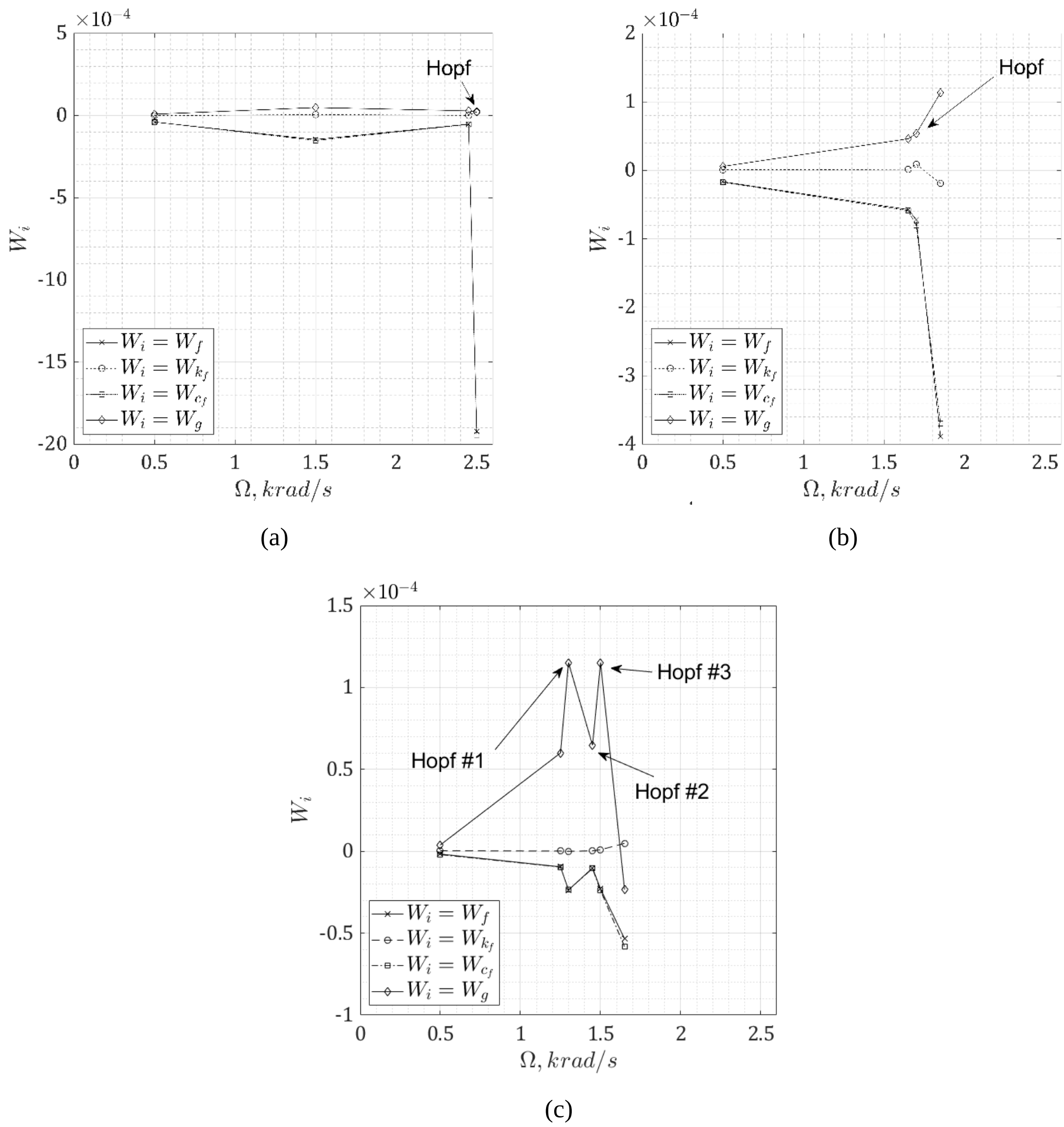

Fig. 3.15: Works W_i evaluated for different values of rotating speed Ω, shaft stiffness $\bar{k}_s = 1$, foil compliance $\bar{a}_f = 0.1$, unbalance eccentricity $e = 2.5 \times 10^{-6}$ kgm, and three different properties of loss factor η: (a) $\eta = 0.003$ (case B2a2) – $\Omega = \{500{,}1500{,}2450{,}2500\}\ rad/s$, (b) $\eta = 0.01$ (case B2b2) - $\Omega = \{500{,}1650{,}1700{,}1850\}\ rad/s$, (c) $\eta = 0.1$ (case B2c2) – $\Omega = \{500{,}1250{,}1300{,}1450{,}1500{,}1650\}\ rad/s$.

This page has been intentionally left blank

4 CONCLUSIONS

In this thesis, the nonlinear dynamic analysis of a flexible rotor supported on two identical gas foil bearings is carried out. The Reynolds PDE for compressible flow, an ODE describing the simplified bump foil structure and the respective second order ODEs for the rotor model are combined in a coupled vector and solved to acquire the gas pressure, the foil deformation and the journal's horizontal and vertical displacements. An extensive study regarding the quality of motion and stability takes place both for an autonomous (perfectly balanced rotor) and a non-autonomous system. The investigated cases (two different unbalance magnitudes were taken into consideration) show several types of motions, as the rotating speed increases.

In some sets of design parameters investigated, the response starts from stable motions around fixed-point equilibrium, and the motion converts to two-periodic where stable limit cycles are induced. Increasing the rotating speed, the system returns to stable fixed points, until further increase on speed, where quasi-periodic motions and the generation of stable limit cycles once again are induced. In other sets, eventually, chaotic motions are detected, the solver breaks and the simulation is terminated. Those changes in terms of motion's quality are provoked when several types of bifurcation occur, such as the Hopf-Andronov, saddle node and Neimark-Sacker bifurcations.

This investigation of non-autonomous (unbalanced) systems gets even more detailed in chapter 3, where a multitude of case-studies takes place. Firstly, two different systems are studied with their only difference being the unbalance eccentricity. The response and STFT diagrams are obtained via a run-up simulation for each case separately, as well as the bifurcation plots via a stepped run-up simulation. The respective system state trajectories, Poincaré maps and FFT plots are introduced for several rotating speeds and used for the dynamic behavior analysis of the rotor-bearing system. Subsequently, by changing different design variables, the analysis examines how the system motion corresponds to these variations. For instance, in section 3.1 where the key changing parameter is the foil compliance, a noteworthy observation is that, as the foil becomes more elastic (meaning that the foil compliance increases), the system tends to be less stable at higher rotating speeds, meaning that the motion trajectories extend close to radial clearance.

In section 3.2, the changing parameter is the foil damping (loss factor). It was observed that as the loss factor increases, the simulation is being terminated at a lower speed. In addition, the stiffest foil does not experience a Neimark-Sacker bifurcation, while the intermediate one experiences a supercritical Neimark-Sacker bifurcation, and the most compliant a subcritical Neimark-Sacker bifurcation. A common conclusion for both the foil compliance and the loss factor is that for certain rotating speeds -mainly when periodic and multi-periodic motions are generated- as they do increase, the eccentricity of the journal increases too.

The results of the performed analysis indicate highly nonlinear behavior. Periodic, multi-periodic, quasi-periodic and chaotic motions and respective variation in the nature of bifurcations are noticed in this work, which can be attributed to the reaction forces of the GFB. The last objective to investigate is the energy flow of the system where the influence of the design variables in terms of works produced by the gas, foil spring and foil damper forces is examined, and a potential correlation between the energy balance between components and the quality of bifurcations was sought. In general, it is expected to notice a change in this balance whenever a bifurcation occurs. The point though is to observe if a major variation takes place in the energy balance if a certain bifurcation type occurs. Indeed, what is of significant importance to be mentioned is the steep variation of the work produced by the gas and foil damper forces when a saddle node bifurcation occurs. Both of works experience a sign change and convert from negative quantities to positive ones, meaning that -after the occurrence of a saddle node bifurcation- energy contribution to the system exists and self-excitation is severely amplified. Similar trend is noticed during a Hopf bifurcation at lower speeds, with the respective works to appear with tendency to change sign.

Further work is demanded in future on the objective of limit cycle motion definition with one of the applicable methods, e.g. shooting method in combination with a continuation method of limit cycles. This will probably render the correlation of the energy flow in the system and the respective bifurcations more clearly for the various design sets.

5 REFERENCES

[1] T. Leister, C. Baum, W. Seemann (2017) On the Importance of Frictional Energy Dissipation in the Prevention of Undesirable Self-Excited Vibrations in Gas Foil Bearing Rotor Systems. Technische Mechanik, 37, 2-5, (2017), 280 – 290

[2] Heshmat, H.; Walowit, J. A.; Pinkus, O. (1983) Analysis of gas-lubricated foil journal bearings. Journal of Lubrication Technology, 105, 4, 647–655.

[3] Howard, S. A.; Bruckner, R. J.; DellaCorte, C.; Radil, K. C. (2007) Gas foil bearing technology advancements for closed Brayton cycle turbines. Tech. Rep. NASA TM-214470, National Aeronautics and Space Administration, United States of America.

[4] Howard, S. A. (1999) Rotordynamics and design methods of an oil-free turbocharger. Tech. Rep. NASA CR-208689, National Aeronautics and Space Administration, United States of America.

[5] Howard, S. A.; Bruckner, R. J.; Radil, K. C. (2010) Advancements toward oil-free rotorcraft propulsion. Tech. Rep. NASA TM-216094, National Aeronautics and Space Administration, United States of America.

[6] DellaCorte C., Zaldana, A., and Radil, K. (2004) A Systems Approach to the Solid Lubrication of Foil Air Bearings for Oil-Free Turbomachinery. STLE/ASME Joint International Tribology Conference, FL Oct. 2003

[7] Gross, W. A. (1962) Gas Film Lubrication, John Wiley and Sons, Inc.

[8] Heshmat, H., Shapiro, W., and Gray, S. (1982) Development of Foil Journal Bearings for High Load Capacity and High Speed Whirl Stability, ASME J. Lubr. Technol., 104, pp. 149–156.

[9] DellaCorte, C., and Wood, J. C. (1994) High Temperature Solid Lubricant Materials for Heavy Duty and Advanced Heat Engines, NASA TM-106570.

[10] Blok, H., and van Rossum, J. J. (1953) The Foil Bearing-A New Departure in Hydrodynamic Lubrication, ASLE J. Lubr. Eng., 9, pp. 316–330.

[11] Ma, J. T. S., 1965, ‘‘An Investigation of Self-Acting Foil Bearings,’’ASME J. Basic Eng., 87, pp. 837–846.

[12] Barnett, M. A., and Silver, A. (1970) Application of Air Bearings to High Speed Turbomachinery, SAE Paper 700720.

[13] DellaCorte, C., and Valco, M. J. (2000) Load Capacity Estimation of Foil Air Journal Bearings for Oil-Free Turbomachinery Applications, STLE Tribol. Trans., 43, pp. 795–801.

[14] Y Hou, Z H Zhu, C Z Chen. (2004) Comparative test on two kinds of new compliant foil bearing for small cryogenic turbo-expander. *Cryogenics*, 44: 69-72.

[15] Z. Y. Guo, K. Feng, T. Y. Liu, et al. (2018) Nonlinear dynamic analysis of rigid rotor supported by gas foil bearings: effects of gas film and foil structure on subsynchronous vibration. Mechanical Systems and Signal Processing, 107: 549-566.

[16] H Heshmat H. (1991) A feasibility study on the use of foil bearings in cryogenic turbopumps. 27th AIAA/SAE/ASME/ASEE Joint Conference, California, USA, June 24-26, AIAA-91-2103.

[17] M Saville, A Gu, R Capaldi (1991) Liquid hydrogen turbopump foil bearing. 27th AIAA/SAE/ASME/ASEE Joint Propulsion Conference and Exhibit, California, USA, June 24-26, AIAA-91-2108.

[18] J S McFarlane, M P Saville, S C Nunez (1995) Testing a 10000 lbf thrust hybrid motor with a foil bearing LOx turbopump. 31st AI-AA/SAE/ASME/ASEE Joint Propulsion Conference and Exhibit, California, USA, July 10-12, AIAA-95-2941.

[19] J M Stoltzfus, J Dees, A Gu, et al. (1992) Material compatibility evaluation for liquid oxygen turbopump fluid foil bearing. 28th AIAA/SAE/ASME/ASEE Joint Propulsion Conference and Exhibit, Tennessee, USA, July 6-8, AIAA-92-3403.

[20] A Gu (1994) Cryogenic foil bearing turbopumps. 32nd Aerospace Science Meeting & Exhibit, Nevada, USA, January 10-13, AIAA-94-0868.

[21] Bonello, P.; Pham, H. M. (2014) The efficient computation of the nonlinear dynamic response of a foil-air bearing rotor system. Journal of Sound and Vibration, 333, 15, 3459–3478.

[22] Hoffmann, R.; Pronobis, T.; Liebich, R. (2014) Non-linear stability analysis of a modified gas foil bearing structure. In: Proceedings of the 9th IFToMM International Conference on Rotor Dynamics, Milan, Italy.

[23] Baum, C.; Hetzler, H.; Seemann, W. (2015a) On the stability of balanced rigid rotors in air foil bearings. In: Proceedings of the SIRM 2015, Magdeburg, Germany.

[24] Peng, J.-P.; Carpino, M. (1993) Calculation of stiffness and damping coefficients for elastically supported gas foil bearings. Journal of Tribology, 115, 1, 20–27.

[25] J. Song, D. Kim (2007) Foil gas bearing with compression springs: analysis and experiments, Journal of Tribology 129:628–639.

[26] S.P. Bhore, A.K. Darpe (2013) Investigations of characteristics of micro/meso-scale gas foil journal bearings for 100-200W class micro-power system using first order slip velocity boundary condition and the effective viscosity model, Journal of Microsystem Technologies 19:509–523, http://dx.doi.org/ 10.1007/s00542-012-1639-1.

[27] S.P. Bhore, A.K. Darpe (2014) Rotordynamics of micro and mesoscopic turbomachinery: a review, Journal of Advances in Vibration Engineering 13 (1), in press.

[28] C. P. Ku, H. Heshmat (1992) Compliant foil bearing structural stiffness analysis: part1-theoretical model including strip and variable bump foil geometry, Journal of Tribology 114 (2) 394–400.

[29] J. P. Peng, M. Carpino (1997) Finite element approach to the prediction of foil bearing rotor dynamic coefficients, Journal of Tribology 119 (1) 85–90.

[30] I. Iordanoff (1997) Analysis of an aerodynamic compliant foil thrust bearing: method for a rapid design. Journal of Tribology 121 (4) (1996) 816-822.

[31] T. H. Kim, L. San Andres (2008) Heavily loaded gas foil bearings: a model anchored to test data, Journal Engineering for Gas Turbines and Power 130 (1) 012504–012508.

[32] L. San Andres, T. H. Kim (2008) Forced nonlinear response of gas foil bearing supported rotors, Tribology International 41 704–715.

[33] D. Kim (2007) Parametric studies on static and dynamic performance of air foil bearings with different top foil geometries and bump stiffness distributions, Journal of Tribology 129 (2):354–364.

[34] S. Le Lez, M. Arghir, J. Frene (2007) A new bump-type foil bearing structure analytical model, Journal of Engineering for Gas Turbines and Power 129 (4) 1047–1057.

[35] K. Feng, S. Kaneko (2010) An analytical model of bump-type foil bearings using a link spring structure and a finite element shell model, Journal of Tribology 132 (2) 1–11.

[36] S. Le Lez, M. Arghir, J. Frene (2009) Nonlinear numerical prediction of gas foil bearing stability and unbalanced response, Journal of Engineering for Gas Turbines and Power 131:012503–012512.

[37] S. P. Bhore, A. K. Darpe (2013) Nonlinear dynamics of flexible rotor supported on the gas foil journal bearings. Journal of Sound and Vibration 332:5135–5150.

[38] J. W. Lund (1968) Calculation of stiffness and damping properties of gas bearings, Journal of Lubrication Technology 793–804.

[39] C.-C. Wang, C.-K. Chen (2001) Bifurcation analysis of self-acting gas journal bearings, Journal of Tribology 123:755.

[40] M. Arghir, S. LeLez, J. Frene (2006) Finite-volume solution of the compressible Reynolds equation: linear and non-linear analysis of gas bearings, Proceedings of the Institution of Mechanical Engineers, PartJ: Journal of Engineering Tribology 220:617–627.

[41] J.-H. Song, D.Kim (2007) Foil gas bearing with compression springs: analyses and experiments, ASME Journal of Tribology 129:628–639.

[42] D. Lee, Y.-C. Kim, K.-W. Kim (2009) The dynamic performance analysis of foil journal bearings considering coulomb friction: rotating unbalance response, Tribology Transactions 52:146–156.

[43] S. LeLez, M. Arghir, J. Frêne (2009) Nonlinear numerical prediction of gas foil bearing stability and unbalanced response, Journal of Engineering for Gas Turbines and Power 131:012503.

[44] D. Kim (2007) Parametric studies on static and dynamic performance of air foil bearings with different top foil geometries and bump stiffness distributions, Journal of Tribology 129:354–364.

[45] J. Zhang, W. Kang, Y. Liu (2009) Numerical method and bifurcation analysis of Jeffcott rotor system supported in gas journal bearings, Journal of Computational and Nonlinear Dynamics 4 011007.

[46] P. Bonello, H. M. Pham (2014) The efficient computation of the nonlinear dynamic response of a foil–air bearing rotor system, Journal of Sound and Vibration 333:3459–3478.

[47] H. M. Pham, P. Bonello (2013) Efficient techniques for the computation of the nonlinear dynamics of a foil–air bearing rotor system, ASME TurboExpo: Turbine Technical Conference and Exposition, p.7.

[48] M. A. Hassini, M. Arghir (2014) A Simplified and Consistent Nonlinear Transient Analysis Method for Gas Bearing: Extension to Flexible Rotors, Düsseldorf, Germany, June 16–20. GT2014-25955.

[49] M. A. Hassini, M. Arghir (2013) A new approach for the stability analysis of rotors supported by gas bearings, Proceedings of ASME Turbo Expo 2013, pp.1–13.

[50] M. A. Hassini, M. Arghir (2012) A simplified nonlinear transient analysis method for gas bearings, Journal of Tribology 134:011704.

[51] J. S. Larsen, I. F. Santos (2015) On the nonlinear steady-state response of rigid rotors supported by air foil bearings-Theory and experiments, Journal of Sound and Vibration 346:284–297.

[52] J. S. Larsen, A. J.-T. Hansen, I. F. Santos (2014) Experimental and theoretical analysis of a rigid rotor supported by air foil bearings, Mechanics &Industry.

[53] J. S. Larsen, A. C. Varela, I. F. Santos (2014) Numerical and experimental investigation of bump foil mechanical behaviour, Tribology International 74:46–56.

[54] J. A. Walowit, J. N. Anno (1975) Modern Developments in Lubrication Mechanics, Applied Science Publishers, London.

[55] J. S. Larsen, I. F. Santos (2014) Efficient solution of the non-linear Reynolds equation for compressible fluid using the finite element method, Journal of the Brazilian Society of Mechanical Sciences and Engineering 1–13.

[56] B. Sternlicht, R. C. Elwell (1957) Theoretical and experimental analysis of hydrodynamic gas-lubricated journal bearings, American Society of Mechanical Engineers-Papers.

[57] J. S. Ausman (1961) An improved analytical solution for self-acting, gas-lubricated journal bearings of finite length, Journal of Basic Engineering 83:188–192.

[58] V. Stingelin (1963) Theoretische und experimentelle Untersuchungen an Gaslagern, PhDThesis, Eidgenössischen Technischen Hochschulein Zürich.

[59] W. J. Harrison (1913) The hydrodynamical theory of lubrication with special reference to air as a lubricant, Transactions Cambridge Philosophical Society 22:34–54.

[60] P. Samanta, N.C. Murmu, M.M. Khonsari (2019) The evolution of foil bearing technology. Tribology International 135:305–323.

[61] Baum C., Hetzler H., Schröders S., Leister T., Seemann W. (2020) A computationally efficient nonlinear foil air bearing model for fully coupled, transient rotor dynamic investigations. Tribol. Int. doi: https://doi.org/10.1016/j.triboint.2020.106434.

[62] H. Heshmat, J.A. Walowit, O. Pinkus (1983) Analysis of gas lubricated compliant thrust bearings, Journal of Lubrication Technology 105: 638–646.

[63] H. Heshmat, J.A. Walowit, O. Pinkus (1983) Analysis of gas-lubricated foil journal bearings, Journal of Lubrication Technology 10: 647–655.

[64] B.J. Hamrock (1994) Fundamentals of Fluid Film Lubrication, McGraw-Hill Series in Mechanical Engineering, McGraw-Hill Inc., NewYork.

[65] Bhore S.P., Darpe A.K. (2013) Nonlinear dynamics of flexible rotor supported on the gas foil journal bearings. J. of Sound and Vib. 332:5135-5150.

[66] Larsen J.S., Santos I.F. (2015) On the nonlinear steady-state response of rigid rotors supported by air foil bearings-Theory and experiments. J. of Sound and Vib. 346:284-297.

[67] Mark W. Reichelt and Lawrence F. Shampine, 8-30-94 Copyright 1984-2014 The MathWorks, Inc.

This page has been intentionally left blank

6 LIST OF TABLES

This page has been intentionally left blank

7 LIST OF FIGURES

This page has been intentionally left blank

--- End of Master Thesis ---